Machine-Learning-Based Surrogate Modeling for Multi-Scale Simulations of Polymer Melts

Souta Miyamoto

2024

Contents

List of Figures

List of Tables

List of Abbreviations

a-Lasso	adaptive Least absolute shrinkage and selection operator
CG	Coarse Graining / Coarse Grained
CLF	Contour Length Fluctuations
CR	Constraint Release
DMD	Dynamic mode Decomposition
DPD	Dissipative Particle Dynamics
DT	Doi-Takimoto
E-Net	Elastic-Net
FENE	Finite Extensible Nonlinear Elastic
FENE-P	Finite Extensible Nonlinear Elastic Peterlin
GENERIC	General Equation for Non-Equilibrium Reversible-Irreversible Coupling
GP	Gaussian Process
GPR	Gaussian Process Regression
Lasso	Least absolute shrinkage and selection operator
LHS	Left Hand Side
MD	Molecular Dynamics
mDPD	many-body Dissipative Particle Dynamics
ML	Machine-Learning / Machine-Learned
MLMSS	Machine-Learning based Multi-Scale Simulations
MSS	Multi-Scale Simulation
NN	Neural Network
PCN	Primitive Chain Network
PINN	Physics Informed Neural Network
RhINN	Rheology Informed Neural Network
RHS	Right Hand Side
RNN	Recurrent Neural Network
RUDE	Rheological Universal Differential Equation
SINDy	Sparse Identification Nonlinear Dynamics
SORF	Stretch and Orientation induced Reduction of Friction
SPH	Smoothed Particle Hydrodynamics
STLSQ	Sequentially Thresholded Least SQuare algorithm

STRidge	Sequentially Thresholded Ridge regression
TEVP	Thixotropic-Elasto-ViscoPlastic
UCM	Upper Convected Maxwell
WCSPH	Weakly Compressible Smoothed Particle Hydrodynamics

Chapter 1

General Introduction

1.1 Introductory Remarks

1.1.1 Overview of Data-Driven Rheology on Multi-Scale Simulations

Soft Matter and Complex Fluid in Chemical Engineering

Soft matter refers to a category of substances that possess structures capable of deformations near room temperature [1, 2]. Their ease of shaping and cost-effectiveness help industrial products. These outstanding features originated from their dynamic structures in response to external stimuli. In particular, when characteristic temporal and spatial scales of their dynamics are close to those of deformations externally applied, their appearances at a macroscopic scale show complexity, so-called *complex fluid* [3]. In the field of chemical engineering, an exploration of soft matter and complex fluids is significant for obtaining desirable materials with designated properties and for understanding the relations between their properties and structures. The National Academy of Engineering's report "New Directions for Chemical Engineering" lists these "complex fluids and soft matter" alongside polymer, biological, and electronic materials.

Complex fluids present challenges in flow prediction methods, and rheology and transport phenomena help us address these challenges. Their constitutive relations (stress-strain relation) are non-linear, namely non-Newtonian fluids. The flows of Newtonian fluids with trivial (linear) constitutive relations are investigated in transport phenomena (fluid mechanics also). On the other hand, a general form of constitutive relations has not been fully established, their classification and description remain one of the main interests in rheology.

Rheology provides knowledge for mechanical responses of a deforming material, studying constitutive relations that usually depend on a substance structure. An exposure of non-Newtonian fluids with nontrivial constitutive relations to various strain fields causes industrial problems in the transport phenomenon. Therefore, as described in Bird's "Transport Phenomena" picking polymer fluids as a typical example of complex fluids [4], understanding these phenomena requires the rheological fundamentals of non-Newtonian fluids.

Polymer Fluids and Rheology

Polymer fluids represent complex fluids because of their hierarchical internal degrees of freedom. According to Rubinstein and Colby, the 20th century can be considered as the *Polymer Age* [5], and the chemical engineering field has contributed to the progress of their industry. In polymer processing, the polymer fluids exhibit complex flow behaviors, especially higher molecular weight polymers exceeding

5000 Da [4]. Even relatively slower flow deformations can elicit a nonlinear response of the fluids, especially in the systems composed of longer polymer chains with more than an order of 10^5 Da because of the topological interactions, i.e., entanglements [6].

Classical constitutive models of polymer fluids are not derived from the physical insights of the microscopic structure (e.g., Boltzmann's superposition principle), regardless of the correlations between structures and properties. Beyond the phenomenological modeling, for equilibrium systems, the universal relations between characteristic structures and material constants have been discussed through scaling theories [7]. Furthermore, responses to weak external fields that do not significantly alter the internal structure can be described by transport coefficients derived from the linear response theory of statistical mechanics. Recent progress in rheology relies upon molecular viewpoints with a methodology directly addressing the nonlinear responses for arbitrary external fields.

Data-Driven Methods for Multi-Scale Simulations

Capturing the complexity of microscopic structures depends on molecular dynamics simulations, facilitated by the advancements in computational environments. The simulations with the supercomputer systems can handle numbers of elements even more than a billion. However, remembering the Avogadro constant, we consider it significantly impractical to simulate fluid behaviors at a molecular resolution to predict complex responses under deformations. Thus, there is interest in multi-scale simulation (MSS) methods that effectively combine descriptions at different scales, such as coarse-grained (CG) molecular dynamics simulations and fluid solvers [8].

In the typical MSS approaches, the fluid system is represented by numerous molecular simulators embedded into each fluid element. Essentially, each allocated simulator receives strain rates determined by the velocity field at the macroscopic scale, and the stress is evaluated from the microscopic state of internal molecules. Microscopic simulators work as state machines with inputs and outputs (i.e., strain rate and stress). Such rheology systems can be identified by solving the inverse problem from the input-output data with experiments and/or simulations. This idea of surrogate modeling is one of the data-driven methods that have been permeating multiple fields in recent years, also in the field of rheology [9–11].

1.1.2 Purpose of Thesis

Figure 1.1 illustrates the previous and proposed approach to analyze the complex fluid flows of polymers. Predicting the complex fluid flows with numerous internal degrees of freedom of microscopic systems can be enhanced by data-driven approaches, which paves the way for new avenues toward general solutions [12]. This perspective initializes this doctoral thesis on the discussion of technological developments.

In the following sections of this chapter, Sections 1.2 and 1.3 review the technical elements of MSS and the recent progress relying on the data-driven approaches, respectively. Building upon the overview provided in the previous section, research considering molecular rheology for polymer fluids is discussed. The evolution of prediction methods for polymer fluid flow, centered on the molecular rheology-based fluid prediction, namely the multiscale simulation approach, is described. Subsequently, recent examples of data-driven methods analysis for rheology and transport phenomena are introduced. Then, Section 1.4 guides the practice in this thesis and the roles of the main chapters.

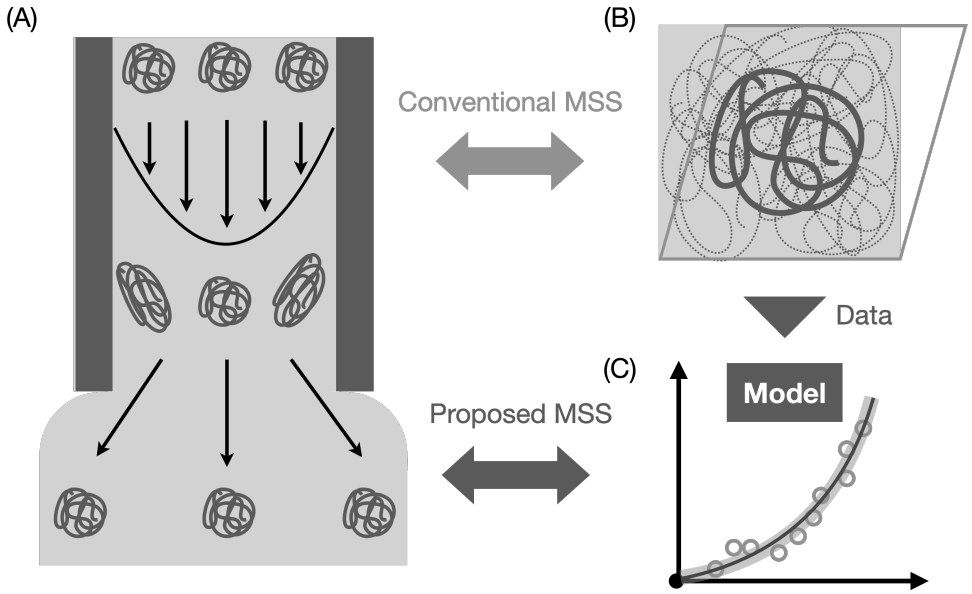

Fig. 1.1 Schematic illustration of the conventional and proposed methods for analyzing complex fluid flows, such as polymer melts. (A) An example of macroscopic polymer flow with the molecular states. The polymer chains in fluid elements are orientated by the flow deformations and the orientations can relax under a freed environment. (B) A microscopic polymer system under a deformation (e.g., simple shears). (C) A data-driven model of constitutive relations is built to minimize the error in the predictions of the rheological data taken from the microscopic simulations under a deformation. In previous, the (direct) MSS means the handling (A) and (B). In this thesis, we investigate the protocol of (A) and (C) (from the data given by (B)).

Exclusions

For simplicity, we focus on isothermal systems without energy transports and heterogeneities, such as concentrations. Instead, the thesis focuses on the analytical techniques for polymer fluid bulks.

1.2 Basics of Multi-Scale Simulations for Polymer Fluid Flows

1.2.1 Microscopic Polymer Systems

This subsection reviews molecular modelings of polymer melt systems describing rheological properties as one of the technical elements of conventional MSS approaches. Polymer melts are handled in polymer processing when forming a shape of products. The rheology of polymer melts is critical not only for industrial demands but also for academic interests. They are typical examples of complex fluids with internal degrees of freedom, potentially insightful to the universalities of such fluid dynamics.

Microscopic descriptions have significantly contributed to sciences as computational methods in addition to experiments and theory. Computational systems can represent the molecules and reproduce the macroscopic properties on the statistical mechanics, including the rheological properties. Full atomistic simulations often face difficulties in computational resources, particularly for soft matters involving mesoscopic structures and their interactions. Thus, CG descriptions (e.g., replacing CH_2 with one bead)

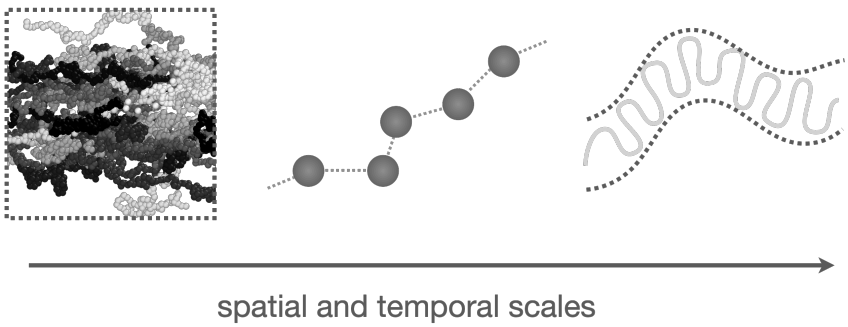

Fig. 1.2 Representative models of polymer chains in melts. (left) A snapshot of beads-spring chains with Kremer-Grest model [13] considering the inter-chain interaction. (center) A bead-spring chain of Rouse model [14]. (right) A tube model[6].

are essential to explain the statistical behavior of the microscopic systems. While these simplifications overlook the detailed information in each CG component, the dynamics of the most significant structure are related to the macroscopic scale, not the minimum components like hydrogens in hydrocarbon frameworks.

Figure 1.2 shows the three types of the CG models of polymer chains. The illustration of aggregated chains is a snapshot of the Kremer-Grest chains [13], which are composed of beads (following Langevin dynamics equations) and springs with inter-chain interactions. The spatial correlations on the inter-chain interactions enable us to describe the dynamics of the polymer chains in detail. We note that the microscopic simulations with the interactions should avoid the deformation collapse of the cell with periodic boundary conditions in the technical commissions developed for specific types of deformations [15–18]. The fundamental rheological properties of polymer melts can be discussed with the simplified model, the Rouse model [14] composed of (Brownian) beads without inter-chain interactions. The Kremer-Grest and the Rouse models are utilized for shorter chain systems since we have limited computational resources. For longer chains in an entangled region with high molecular weights, the tube model [6] represents the topological confinements of chains illustrated on the right-hand side of Fig. 1.2. In a system composed of longer polymer chains, stress shows slow relaxations because of the larger spatial and temporal scales, and rheological dynamics often appear in macroscopic fluid flows, which do not belong to the dynamics of a Newtonian fluid.

Essentially, in the CG systems, the stresses are evaluated by the potential forces dominated by those from the bonds. The momenta are usually damped at their CG time scales, and they act as almost constants in the stresses. Thus, the statistically evaluated stress represents the averaged orientation of the bonding structure of a polymer system.

The characteristic relaxation time of the stress of an entangled polymer system is around that of macroscopic flows. The deformations, with the magnitude of the inverse of the relaxation time, change the structure from that in equilibrium, whose examples are the orientation and stretches of the polymer chains. When the structures are significantly deformed, the nonlinear stress responses depending on the characteristic structures are observed in the flows, e.g., the Weissenberg effect, shear-thinning, shear-thickening, strain-softening, strain-hardening, and so on, appearing in polymer processing. To comprehensively predict and control these phenomena, we should use a well-established dynamical equation

of stress based on the microscopic descriptions.

The dynamical equations of statistical stress can be derived in some simple cases; for example, when the Brownian beads are linearly bonded (no brunches) by harmonic springs, we can obtain the closed formula of the dynamics, i.e., Maxwell model. However, in most practical applications, one cannot derive the constitutive equation without the nontrivial approximation (e.g., FENE-P model). Nevertheless, the simplicity and transparency of the analytical solutions are essential to our understanding.

For adopting the complexity of the applications, the numerical simulations of the CG models play significant roles in evaluating the stress dynamics while considering the history of deformation gradients in the complex flows. The primal research of MSS [19] employs the simplest polymer model, the dumbbell model with two beads connected by a linear or nonlinear spring. With the computational advancements, recent MSS studies rely on the sliplink models [20–26], which, extended from the tube model, can precisely describe the rheological behavior on the parameters bridged to molecular weights and chemical species.

1.2.2 Macroscopic Fluid Solver

This section shows the governing equations of complex fluid flows at a macroscopic scale independent of the constitutive relations. In contrast to the purely viscous fluids governed by the Navie-Stokes equation, the viscoelastic fluids follow the following mass and momentum conservation equations within an isothermal domain:

$$\frac{\partial \rho}{\partial t} + \boldsymbol{\nabla} \cdot (\rho \boldsymbol{v}) = 0, \tag{1.1}$$

$$\frac{\mathrm{D}\boldsymbol{v}}{\mathrm{D}t} = \frac{1}{\rho}\boldsymbol{\nabla} \cdot (\boldsymbol{\sigma} - P\boldsymbol{I}) + \boldsymbol{F}_{\mathrm{ex}}, \tag{1.2}$$

where ρ the mass density, $\boldsymbol{v}$ the fluid velocity, $\mathrm{D}/\mathrm{D}t$ the advective derivative, $\boldsymbol{\sigma}$ the stress, P the pressure, $\boldsymbol{I}$ the unit tensor, $\boldsymbol{F}_{\mathrm{ex}}$ the external force. Additionally, the constitutive equations, the closed form of the equation between the strain rate $\boldsymbol{D}$ and the stress $\boldsymbol{\sigma}$, are used to predict complex fluid flows [3]. Typical equations are of Newtonian fluids and Maxwellian fluids, which have the linear constitutive relations of Newton and Maxwell as

$$\boldsymbol{\sigma} = \eta \boldsymbol{D}, \tag{1.3}$$

$$\left(1 + \tau \frac{\delta}{\delta t}\right)\boldsymbol{\sigma} = \eta \boldsymbol{D}, \tag{1.4}$$

where η the viscosity, $\boldsymbol{D}$ the strain rate, τ the relaxation time, $\delta/\delta t$ the material derivative satisfying the objectivity principle. When the constitutive relation follows the Newton's Eq. (1.3), the Cauthy's Eq. (1.2) becomes the Navie-Stokes equation. Examples of the empirical viscoelastic constitutive relations with an extended form on Eq. (1.4) are the Oldroyd models[27], the White-Metzner model[28], the Giesekus model [29], the Phan-Thien-Tanner model[30], etc. For general complex fluids, the appropriate nonlinear terms in the equations are not known and are dependent on the types of fluids.

Lagrangian Fluid Solvers

The simulations often employ particle-based solvers, while the standard choice with these empirical constitutive equations relies on the mesh-based ones, e.g., the finite element method. The Lagrangian solvers can simplify the advection of the microscopic simulators with the numerous state variables. One of the methods is the smoothed particle hydrodynamics (SPH) [31], which discretizes the fluid domain into

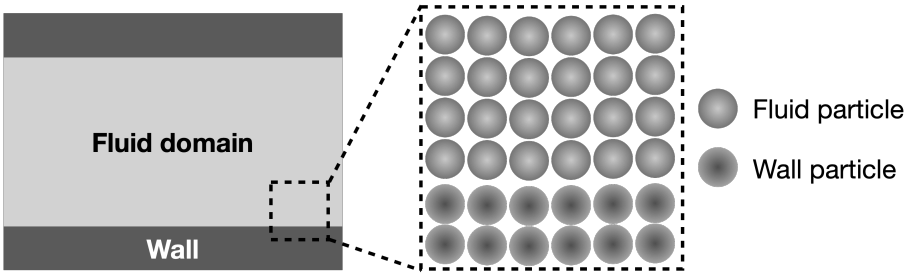

Fig. 1.3 Schematic illustration of the macroscopic fluid solver based on Lagrangian specification.

the smoothed particles. Figure 1.3 demonstrates discretizing the fluid domain into the particle elements. The physical quantities at a point are defined as the summations over the surrounding smoothed particles convoluted with the distances.

1.2.3 Applications of Multi-Scale Simulations

Constitutive equations can reasonably address the linear relation described in Eqs.(1.4), but the nonlinear properties substantially dependent on the microscopic structures are not unified in the existing equation-based models. To overcome this problem, the MSS method has been proposed to analyze the complex fluid flows while considering their microscopic and time-dependent structures. The MSS methods employ two models at different scales which are the macroscopic governing equations and the microscopic (CG) molecular-based model. The two models are connected by velocity gradient and stress, where the velocity gradients at points of a macroscopic domain work as the (affine) deformation rates, which are sent to the corresponding microscopic simulators. A microscopic simulator holds a state under their deformation histories along the streamlines of the fluid flows, which provides the stress dynamics instead of constitutive equations.

This MSS framework has evolved over the past 30 years, starting with the work of Laso and Öttinger [19]. In their original method, the microscopic system comprises the non-interactive chain models, and the macroscopic fluid domain is finitely discretized to be assumed as laminar flows between parallel plates with only a single deformation mode (shears).

MSS applications are classified into two types based on whether they use non- or interactive polymer chains in the employed microscopic systems. The differences between these MSS types are not only the physical viewpoints at the microscopic scale but also the ease of technical handling of the deforming simulation cell boxes; the latter limits the MSS to the (quasi) one-dimensional flows with a deformation type. When we employ the microscopic polymer model with a non- or pseudo-interactive polymer chain model, arbitrary deformations can be applied to the microscopic systems. With this simplified microscopic model, MSS can analyze any fluid flows where their fluid elements experience time-dependent deformation modes. Ideally, simulating the macroscopic flows based on any microscopic model is a goal of MSS technique.

Some of the previous MSS studies [32–38] rely on the non- or pseudo-interactive chains model (e.g., the dumbbell models or the sliplink models) to accurately describe the entangled polymer melt rheology. A SPH [32] or smoothed dissipative particle dynamics (SDPD) [39] method can handle the general fluid flows because of the simplicity of advection of the microscopic simulators. This type of MSS approach enables us to analyze arbitrary flows based on a type of microscopic descriptions and has been applied

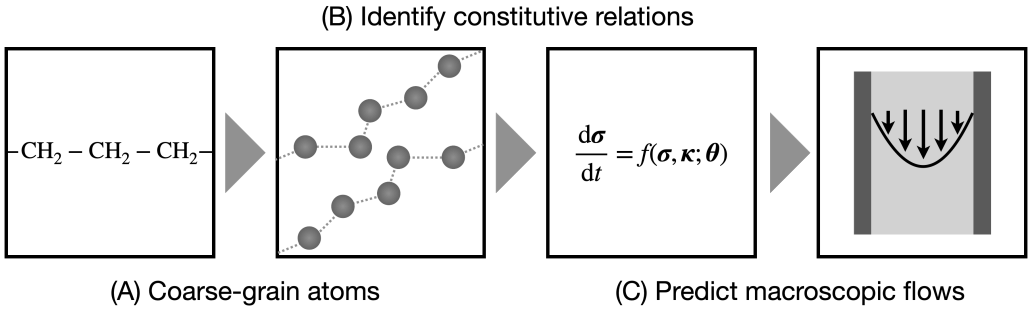

Fig. 1.4 The classification upon the spatial and temporal scales for the rheological applications of data-driven methodologies about fluid flow predictions. The icons in the first and second boxes mean the atomistic/CG descriptions at the micro and mesoscopic scales. Those in the third and fourth boxes are the constitutive relation and the fluid flows as the macroscopic local and global descriptions, respectively. (A) coarse-graining atomistic description, (B) identifying the CG systems, and (C) predicting the macroscopic flows are the typical three types of ML applications.

to some analysis of the polymer processing flows.

We can apply the MSS approach to more detailed microscopic models with interchain interactions when idealizing the macroscopic flows to ones with single-mode deformation mode, shears [19, 40] and uniaxial elongations [35, 41, 42]. To avoid the collapse of simulation cells under deformation, the techniques of recoverable cells for specific types and single mode of deformations [15–18].

1.3 Review on Data-Driven Rheology

In recent years, successful cases of MSS for shear [40] and elongation [42] have been demonstrated with recoverable periodic boundary conditions. However, we currently cannot handle general time-dependent deformations. The use of machine learning constitutive relationships can avoid technical issues regarding periodic boundary conditions and significantly reduce computation time. Data-driven approaches are increasingly being integrated into computational methods in material science, playing a role in predicting as well as discovering experimental results based on physical insights [43]. Machine learning models (e.g., neural networks; NNs) can be tailored to the specific properties of each material. In the field of rheology, complex fluids such as polymer fluids, which exhibit complex behaviors dependent on internal degrees of freedom, are of interest. To advance the practical application of complex fluids and to deepen our understanding of their rheological properties, the use of machine-learned models that combine physical and data-driven approaches is required [10, 11].

Figure 1.4 illustrates the three types of data-driven methods for rheology where the classification is based on the bridges of the four systems: full-atomistic, microscopic, macroscopic but local, and macroscopic ones. First, from full-atomistic to microscopic scales, coarse-graining is a significant example of dimensionality reduction that preserves the macroscopic properties and the structure of its rheology. Coarse-graining enables us to investigate the rheological properties for the (longest) relaxation time of the system for the sake of ignoring the bottleneck of the atomistic system. Second, taking the rheological data from the CG systems, we can identify the dynamics of stress with the minimum number of dimensions based on regression models. The rheology data of the complex and viscoelastic system should cover the time-dependent results under deformations. Finally, the identified constitutive relations can be utilized

for the macroscopic flows where the fluid dynamics solvers are enhanced by data-driven approaches, such as physics-informed neural networks (PINNs) [44]. The three applications of data-driven methods for rheology are described in the following subsections.

1.3.1 Coarse-Graining a Microscopic Description

For machine learning-based MSS, there are two important aspects to consider in determining the constitutive relation: the reliability of the data source (descriptors of micro models) and the validity of the assumed machine learning model itself. As discussed in the previous section, using machine learning methods to learn from the responses of microsystems exposed to steady-state or time-dependent external fields dramatically improves the computational efficiency of MSS. However, the reliability of flow predictions derived using these applications is always constrained by the quality of microscale systems. Deriving polymer dynamics using a full atomic model is prohibitively expensive. Therefore, CG descriptions, commonly adopted (i.e., bead-spring model, sliplink model), are actively researched and enable efficient prediction of dynamics. Special treatment is required for dimension reduction in constructing CG elements and their motion to maintain rheological reliability [45].

Several technical reviews have been published explaining how to derive CG interaction potentials appropriately [46, 47]. Ravikumar et al. [48] proposed conducting many-body dissipative particle dynamics (mDPD) simulations of polymer solutions and suggested using CG potentials that preserve Schmidt numbers of full atomic descriptions, i.e., the ratio of dynamic viscosity to diffusion coefficient. Mukkamala et al. [49] reduce the bottlebrushes using a proper orthogonal decomposition for their DPD simulation. Normal CG potentials are state-dependent, making it difficult to create independent CG potentials for each state across a wide parameter range. To overcome this, Shireen et al. [50] constructed temperature-transferable CG models by obtaining temperature-dependent parameters with DeepNN and successfully predicted their mechanical and thermal properties. During their training process, both binding and non-binding potentials were adjusted to match molecular structure and density. Additionally, we note the use of MD-based generative adversarial networks (MDGAN) [51, 52] to provide a set of latent variables encoding molecular configurations and dynamics. These efforts are crucial for identifying features and parameterizing appropriate models, aiding in accurately describing macroscopic flow of complex fluids.

When deriving constitutive relationships from a CG model, adopting the structure of machine learning is effective in capturing stress behavior. Machine learning models are trained against CG models, and their stress represents atomic and meso structures. However, stress alone is insufficient to describe rheological properties for any microsystem, especially when higher-order relaxation modes occur. Therefore, identifying additional descriptors is necessary to accurately describe stress behavior. For example, methods like singular value decomposition or autoencoders reduce system states, and dynamic mode decomposition (DMD) [53] can track their time evolution.

When representing the dynamics of descriptors using machine learning models, we face two main difficulties. Firstly, the accuracy and stability of model predictions heavily depend on the quantity and quality of training data. Secondly, it becomes challenging to interpret the model, especially when using black-box structures of fundamental neural networks or Gaussian Process Regression (GPR), where Gaussian Process (GP) is the stochastic process, such as following a multivariate normal distribution. If interpretability is the primary objective, alternative methods like symbolic regression are considered. One example is the sparse identification of nonlinear dynamics (SINDy) [43], which uses sparse regression to identify the most plausible terms from a dictionary of possible candidates for the right-hand side of a

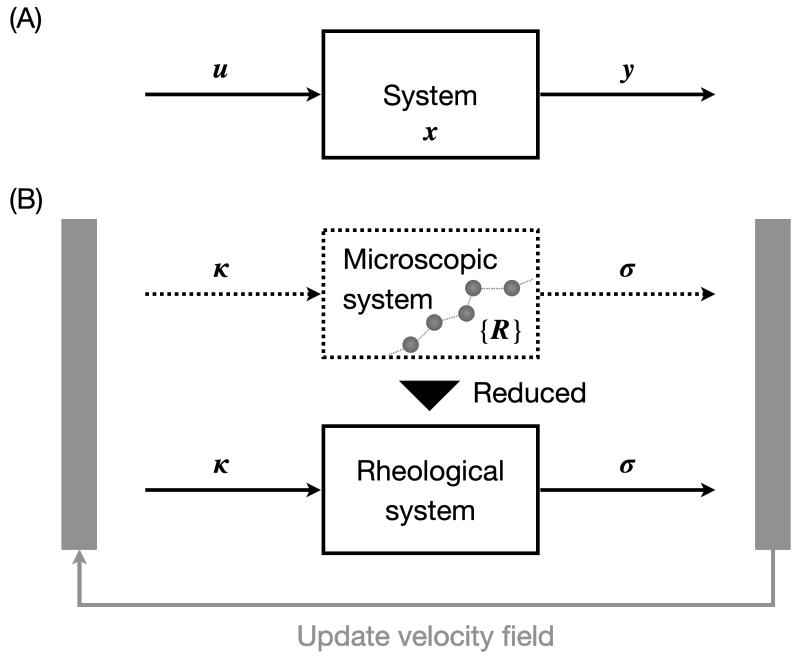

Fig. 1.5 Schematic illustration of the rheological identification problem. (A) Input-output system. The input $\boldsymbol{u}$ changes the state $\boldsymbol{x}$ of the system, and the output y is evaluated from the state $\boldsymbol{x}$ and the input $\boldsymbol{u}$. (B) The rheological systems used in the rheological or fluid simulations where the velocity gradient $\boldsymbol{\kappa}$ from the macroscopic velocity field is the input and the stress evaluated by the system state (e.g., the molecular conformation $\{\boldsymbol{R}\}$ for the system with microscopic configurations, or the stress itself $\boldsymbol{\sigma}$). The stress field updates the velocity field at the macroscopic scale. Except for the multi-scale approaches, the utilized rheological system with numerous degrees of freedom is reduced by phenomenological insights or data-driven techniques.

dynamical system.

In conclusion, viscoelastic stress responses can be approximated using dimension reduction models (e.g., DMD or SINDy), and attempts to learn a complete description using machine learning models can be made at the cost of interpretability. While these methods have shown success for simple systems, considering physical constraints (e.g., rotational symmetry of objective stress rates) becomes crucial for efficiently predicting rheological properties of complex fluids. Developing better data generation protocols (e.g., active learning) to improve robustness and reduce training time is necessary. Resolving these issues will dramatically enhance the ability to predict fluid flow in complex systems based on material properties.

1.3.2 Data-Driven Constitutive Relation and its Application

Figure 1.5 shows the rheological identification problem. The input-output system as Fig. 1.5(A) is the general system targeted in the system engineering field, the input $\boldsymbol{u}$ change the state $\boldsymbol{x}$ and the output $\boldsymbol{y}$ depends on the input and state. In Fig. 1.5(B), the rheological instance of the system is described where the input is the velocity gradient $\boldsymbol{\kappa}$ and the output is the stress $\boldsymbol{\sigma}$, and the state is the degrees of freedom as the molecular conformation $\{\boldsymbol{R}\}$. Data-driven techniques schematically reduce the dimension of a state. In the simplest case, the state is just a (total) stress $\boldsymbol{\sigma}$, the output itself as the phenomenological

constitutive equations.

For complex fluids, machine learning surrogate models of constitutive relationships have been developed [54–59]. Using trained machine learning models, micro-model simulators and surrogate constitutive relationships are replaced to reduce computational costs and statistical errors [54–56, 60–63]. Such machine learning constitutive relationships can reasonably address both linear and nonlinear rheological properties. In the pioneering work by Zhao et al. [54, 56], they inferred the constitutive relationships of generalized Newtonian fluids based on steady shear viscosity using Bayesian methods, precisely GPR [54]. Additionally, they utilized the FENE-P model with relaxation time dependent on shear strain rate [56]. Assuming the form of constitutive relationships, i.e., generalized Newtonian fluids and the FENE-P model, they accurately predicted rheological properties based on microstructures from simple shear simulations. Notably, their active-learning framework automatically generates new training data points and updates the machine learning model, thereby avoiding inference in regions with significant uncertainties if needed during prediction.

Chang et al. [62] expanded this framework to colloidal dispersion systems. Here, in simple continuum flow simulations, contributions to particle viscosity and normal stress were active-learned as functions of volume fraction and shear strain rate from corresponding bulk system shear simulations.

For time-dependent viscoelastic materials such as polymer melts, Seryo et al. [55] proposed an extension of GPR-based learning methods. In this approach, the training data includes time-series data of stress under time-dependent shear flow. This data learns the time derivative of stress as a function of stress and shear strain rate. During the learning process, the dynamics of the microscale system are represented by the stress tensor $\boldsymbol{\sigma}$, controlled by the external strain rate tensor $\dot{\boldsymbol{\gamma}}$. The time evolution of $\boldsymbol{\sigma}$ is generally described by the following equation:

$$\frac{\mathrm{d}\boldsymbol{\sigma}}{\mathrm{d}t} = \boldsymbol{f}(\boldsymbol{\sigma}, \dot{\boldsymbol{\gamma}}), \tag{1.5}$$

Here, $\boldsymbol{f}$ is an arbitrary function learned from the data. Therefore, GPR [55, 61, 63] and recurrent neural networks (RNNs) [59] have been employed. The former method has been validated for both linear [55] and nonlinear [61, 63] stress responses under shear or elongational flows. The latter RNNs have been used to mimic nonlinear constitutive equations under shear flow [59].

This approach cannot be simply applied to active learning methods because controlling the target input states (i.e., generating polymer configurations in response to stress) is difficult, as used for predicting steady-state conditions [54, 56, 62]. The current simulation predictions are limited to regions where the stress response is weaker than unity in terms of Weissenberg number and elasticity number. Here, the Weissenberg number is the product of the shear rate and relaxation time, while the elasticity number is the ratio of the Weissenberg number to the Reynolds number. Nevertheless, these methods efficiently emulate microsystems with material functions, accurately describe rheological properties, and reduce computational costs and statistical errors.

When utilizing standard machine learning architectures to monitor the dynamics of a system, as indicated by the stress tensor, it cannot be assumed that the physical constraints will inherently be met. Specifically, constitutive equations must exhibit rotational symmetry of the objective stress rate, as mandated by the principle of material objectivity.

One approach to achieve this requirement involves employing specially designed neural networks (NN), such as the rheological universal differential equation (RUDE) model proposed by Lennon et al. [58]. RUDE incorporates additional nonlinear terms in the Maxwell constitutive equation. Furthermore, ensuring thermodynamic consistency within a multiscale framework necessitates adopting the general

equation for non-equilibrium reversible-irreversible coupling (GENERIC) formalism.

Examples of such machine learning models include GENERIC formalism informed NNs (GFINNs) introduced by Zhang et al. [64], as well as Hamiltonian and Lagrangian NNs for classical mechanics presented by Greydanus et al. [65] and Cranmer et al. [66], respectively. These physics-informed NNs are capable of inferring and predicting the deterministic and stochastic irreversible dynamics of complex systems.

Another notable example of an ML model constructed to adhere to the principle of objectivity (rotational symmetry of constitutive relation) is the DeepN^2 framework proposed by Fang et al. [60]. This framework describes the dynamics of Brownian beads connected by nonlinear bonds. It employs an encoder network to map the high-dimensional microscopic structure into a low-dimensional macroscopic feature space. Additional networks are then utilized to learn the mapping between the feature space and stress, as well as the time evolution within the feature space.

1.3.3 Forward and Inverse Problems at a Macroscopic Scale

In this section, we introduce machine learning applications for solving forward and inverse problems in rheology research, where the forward problems are to predict the flows based on a constitutive relation, and the inverse problems are to infer the constitutive relation from the flows.

When the form of constitutive equations is known, predicting fluid flow involves solving forward problems using machine learning-based methods. PINNs give mesh-independent solvers on a fluid domain [44]. For non-Newtonian fluids, an example of this is non-Newtonian PINNs (nn-PINNs) [67], which solve the conservation equations for mass and momentum and the specific type of constitutive equations (e.g., [67] employed thixotropic-elasto-viscoplastic model; TEVP model). However, PINNs solutions only minimize the physical loss terms in the loss function and do not strictly satisfy the governing equations. Ideally, solvers that precisely satisfy the physical properties of non-Newtonian fluids are sought. For instance, for Newtonian fluids, the physical properties of Stokesian fluids embedded in GP could potentially be achieved [68, 69].

When constitutive equations or the values of their parameters are not directly known, one faces the inverse problem of estimating material functions. With minimal rheological insights, machine learning methods can estimate transplantable and interpretable material functions. For example, Jamali et al. predicted material functions using Rheology-informed NNs (RhINNs), a type of PINNs combined with neural networks and known constitutive equations [57, 70]. Farrington et al. reported important additional descriptors for predicting blood flow using machine learning models [71]. Models like RUDE [58] and GPR [55] can be used without prior knowledge, but these models do not directly extract physically meaningful parameters. To provide physically meaningful interpretations from large-scale machine learning models, additional reductionist procedures are necessary, such as model selection for existing models or symbolic regression methods for discovering function forms.

Machine learning methods can enhance computational rheology and its data generation. Efforts continue to create extended datasets linking macroscopic properties with molecular structures for polymers [72]. While simulations for long polymers incur significant computational costs, these may be addressed using CG potentials extracted by machine learning models [46, 47]. Similar applications for colloidal dispersions include corrections for short-range fluid interactions based on GPR force fields [73].

Machine learning methods are innovatively advancing the resolution of forward and inverse rheology problems, which is expected to become widespread in the future. While large-scale machine learning

models are currently being attempted to directly link flow predictions to industrial issues, lightweight models are needed for physical understanding and model development.

1.4 Structure of the Thesis

In the previous sections, we reviewed and summarized the related studies on the basics of MSS and the data-driven approaches for rheology. Technological development of MSS has been progressing in order to consistently handle flow prediction of complex fluids based on microscopic viewpoints, but the industrial flow analysis is significantly impossible due to the considerable computational costs. In this thesis, we investigate the possibility of a more efficient approach to employing the machine learning regression model to surrogate the microscopic simulators as the bottleneck part of MSS, named *MLMSS*. To develop the MLMSS method, this thesis is structured as follows.

In Chapter 2, we first give a simple example of the MLMSS. The MLMSS protocol is developed based on the analysis of a quasi-one-dimensional laminar flow (composed of simple shear deformations only) driven by a pressure gap between parallel plates. Assuming a polystyrene melt system in an entangled state, we organize the technical elements of a microscopic polymer model, a regression model, and a macroscopic fluid solver.One scheme comprises the procedures for generating the training dataset from the microscopic polymer system, learning the constitutive relation from the data, and applying the learned relation to the macroscopic flow analysis.

In Chapter 3, we extend the MLMSS method developed in Chapter 2 for the general two-dimensional flows composed of time-dependent deformation modes. For the efficient use of a regression model, we consider the rotational symmetry of the stress rate required by the objectivity principle. We assess the extended regression model by using pressure-gap driven flows in a contraction expansion channel employed in the typical benchmark problem of viscoelastic fluid flows

In Chapter 4, the regression models with numerous parameters sometimes demand significant computational resources. Symbolic regression methods help us to use a transparent model and additionally provide an economical model with sparsity-promoted techniques. We confirm the ability to (re-)identify the constitutive relations of the phenomenological and microscopic models whose constitutive equations are known or unknown.

In Chapter 5, we extend a correction model based on mono-dispersed molecular weight systems for bi-dispersed and improve rheological predictions of microscopic models used in a future MLMSS. It has already been investigated that the sliplink model, also used in Chapters 2 and 3, provides excellent predictions of rheological properties for entangled polymer melts under shear deformation and uniaxial extensional deformation. On the other hand, recent experimental studies have revealed that under extremely high strain rate flow, strain softening occurs contrary to model predictions, and this is considered because of friction reduction by significant stretches and orientation of the polymer chains.

Finally, in Chapter 6, we summarize the results of Chapters 2–5 and discuss the remaining issues and the future direction of developing the MLMSS method.

Chapter 2

Protocol of Machine-Learning-Based Multi-Scale Simulations (MLMSS)

2.1 Introduction

In this chapter, the author gives a simple example of the MLMSS. The MLMSS protocol is developed based on the analysis of a quasi-one-dimensional laminar flow (composed of simple shear deformations only) driven by a pressure gap between parallel plates. Assuming a polystyrene melt system in an entangled state, we organize the technical elements of a microscopic polymer model, a regression model, and a macroscopic fluid solver.One scheme comprises the procedures for generating the training dataset from the microscopic polymer system, learning the constitutive relation from the data, and applying the learned relation to the macroscopic flow analysis.

When numerically predicting the flow of a polymeric system, knowledge of the stress response, as a function of the experienced strain history, is required. However, the accurate prediction of the stress of a polymeric system is highly non-trivial, because it is a reflection of the state of the constituent polymer chains in the system [3]. Currently, there are three typical approaches for obtaining this stress response to an applied strain rate history:

(i) Constitutive equations
(ii) (Coarse-grained) molecular-based models
(iii) Machine-Learned(ML) constitutive relations.

The first approach relies on the use of (i) a constitutive equation, which specifies the time-dependent response of a polymeric system to an arbitrary strain rate[74]. This is the conventional and practical approach, widely used to model the complex flows encountered in industry thanks to its relative simplicity and low computational cost. However, one is always faced with the problem of choosing the appropriate empirical equation to describe the rheology of the target fluid. There are dozens of candidate models, each with its own set of coefficients, which must be specified as material functions, usually by fitting against available experimental data[75]. In addition, because such equations cannot always be derived from molecular-based polymer models, the physical interpretation of their parameters is not always clear.

To resolve the issues of adopting an otherwise ad-hoc constitutive equation, (ii) a (coarse-grained) molecular-based simulation method to directly evaluate the stress response was developed[19]. This approach has the merit of providing an explicit link between the microscopic and macroscopic degrees of freedom. This type of Multi-Scale Simulation (MSS) was pioneered by Laso and Öttinger, who were the

first to combine continuum and molecular-based models for simulating polymer flows[19]. Recent work has shown how to develop such multi-scale descriptions in a thermodynamically consistent manner, within the GENERIC formalism [76]. Several research groups have used this MSS framework to investigate the coupled hierarchical dynamics of polymer fluids[32, 34, 38, 77, 78]. Ellero and coworkers employed a particle-based solver within a Lagrangian description, in order to account for the advection of microscopic systems[32]. Murashima and Taniguchi have analyzed the history-dependent flow of entangled polymer melts[33, 79–81]. Sato and coworkers have reported applications of entangled polymer melts for polymer processing[35, 36, 41, 82], a review of which is given in Ref.[8]. However, even for MSS using a mean-field and/or coarse-grained treatment of the polymer chains, such an approach requires an almost prohibitive computational cost. Thus, the price that is paid for maintaining molecular-based information means that MSS have been restricted to relatively simple and small-scale flows, far removed from industrially relevant polymer processing flows. At present, even with access to the most advanced parallel computation resources and techniques, it is only possible to simulate systems with $\mathcal{O}(10^8)$ total polymer chains, for simple 2D flow geometries[38].

In addition to these two established approaches, (iii) Machine Learning (ML) methods have recently been investigated. Zhao and coworkers have simulated polymer melt flows with a machine-learned constitutive relation[54], under the assumption that the target fluid is a generalized Newtonian fluid, described only by a strain rate-dependent viscosity. Following this work by Zhao et al., Seryo and coworkers [55] proposed a more general method, also based on a Gaussian Process (GP) regression scheme, to handle viscoelasticity, under the assumption that the constitutive equation could be written in differential form, as

$$\dot{\boldsymbol{\sigma}} = \dot{\boldsymbol{\sigma}}(\boldsymbol{\sigma}, \boldsymbol{\kappa}) \tag{2.1}$$

where $\boldsymbol{\sigma}$ is the stress tensor, $\dot{\boldsymbol{\sigma}}$ its time derivative, and $\boldsymbol{\kappa}$ the velocity gradient. Within this approach, the constitutive equation for $\dot{\boldsymbol{\sigma}}$ is defined in terms of a GP prior, which is then conditioned on the available training data (obtained by measuring the stress response of the target system under fundamental deformations), in order to predict the test response under arbitrary deformations. With this GP regression, they succeeded in extracting the constitutive relation for a system of non-interacting Hookean dumbbells, using $\mathcal{O}(10^3)$ training points. This learned constitutive equation was then used to perform simple flow simulations at a significantly reduced computational cost, with no appreciable loss of accuracy. Thus, we consider that this type of ML approach provides an attractive alternative for MSS of polymer melts, in particular, and complex fluids in general.

We note that Zhao and coworkers have also considered elastic effects in a subsequent paper, by adopting a specific constitutive equation[56]. Fang et al. have shown how to learn the constitutive relation for unentangled polymer melts within the bead-spring model, using a neural-network scheme called DeepN^2, and applied it to a system of linear- and star-shape chains[60]. S. Jamali et al. have used physics-informed neural networks (PINNs) for rheological research on an empirical constitutive equation, the Thixotropic Elasto-Visco-Plastic (TEVP) fluid model, by directly solving the equation and then inversely determining/recovering the model parameters[67, 83, 84]. These approaches have succeeded to produce sophisticated models for polymer melts, based on prior knowledge of the bead-spring models or phenomenological equations. Furthermore, from a theoretical point of view, Generic Formalism Informed Neural Networks (GFINNs) have been proposed in order to incorporate the Generic formalism within the PINN framework[64]. We propose an alternative, model-free approach, based on Eq. (2.1).

Until now, the verification of the general ML approach using Eq. (2.1) has only been performed for

a linear constitutive relation, for one-dimensional uni-deformation mode shear flows[55]. In particular, the simulation scheme was applied to a mono-disperse system of non-interacting Hookean dumbbells, which possess a linear constitutive relation, i.e., the system exhibits a linear response regardless of the magnitude of the deformation.

This previous assessment has not established whether or not such an ML-based framework can be applied to a fluid exhibiting non-linear stress responses. This is crucial, as general complex fluids possess a hierarchical structure, with a corresponding non-linear constitutive relation. This non-linear constitutive relation is fundamental to explain the variety of flow phenomena characteristic of such fluids, e.g., shear-thinning, shear thickening, strain softening, and strain hardening, among others. Despite its simplicity, we expect that Eq. (2.1) can be applied to such complex fluids, including polymeric liquids, micellar solutions, and colloidal dispersion, at least in the macroscopic flow regime, provided that the stress can be well represented by the internal structure of the fluid, with a velocity gradient history dependence. However, the non-linearity could affect the accuracy of the simulations and/or increase the computational cost, thus reducing the effectiveness of this ML approach.

To answer such questions, this chapter reports on extensions of the ML framework based on Eq. (2.1), and evaluates its accuracy and efficiency when simulating entangled polymer flows. For this, we perform polymer flow predictions using both MSS and ML constitutive relations, for a coarse-grained molecular-based model with a non-linear constitutive relation. For simplicity, we will only consider pressure-driven flow between two flat parallel plates in 2D.

This chapter is structured as follows. In Section 2.2 we explain the MSS framework using the ML constitutive relation. In Section 2.3 we present the simulation results obtained using this learned relation, and its applications. Finally, Section 2.4 discusses and summarizes our work.

2.2 Method

At the macroscopic scale, the flow of a complex fluid is governed by the Cauchy equation

$$\frac{\mathcal{D}\boldsymbol{p}}{\mathcal{D}t} = \boldsymbol{\nabla}\cdot\boldsymbol{\sigma} - \boldsymbol{\nabla}P \tag{2.2}$$

where $\boldsymbol{p}$ is the fluid momentum density, $\boldsymbol{\sigma}$ the fluid stress, P the pressure. The stress tensor, appearing in the first term on the right-hand side of Eq. (2.2), is determined by the internal degrees of freedom in the constituent fluid. As we will consider incompressible fluids, the second term on the right hand side $\boldsymbol{\nabla}P$ is determined so as to satisfy this incompressibility. In the conventional MSS approach, the stress $\boldsymbol{\sigma}$ is obtained from a statistical average of the microscopic polymer systems embedded in the fluid. As the confirmation of the polymer chains is updated according to the applied velocity gradient, the derived stress will necessarily reflect the history of these velocity gradients.

Within our ML approach, the stress $\boldsymbol{\sigma}$ is evaluated under the assumption that Eq. (2.1) is valid. Thus, in principle, the constitutive relation can be learned in advance from a suitable set of training data generated from the microscopic model under consideration. In particular, the relation between $\dot{\boldsymbol{\sigma}}$ and $\boldsymbol{\sigma}$ is learned from the response of the microscopic polymer system to fundamental deformations, specified by a velocity gradient history $\boldsymbol{\kappa}(t)$. In this study, we consider the special case where $\boldsymbol{\kappa}$ is limited to laminar shear-flows, i.e., only the xy-component (κ_{xy}) is used. This results in a constitutive relation of the form of Eq. (2.1), which can be used within macroscopic flow simulations to infer/predict the stress at the next simulation time step, given the current stress and velocity gradient. A schematic overview of this simulation framework is presented in Fig. 2.1, and can be summarized in the following three steps:

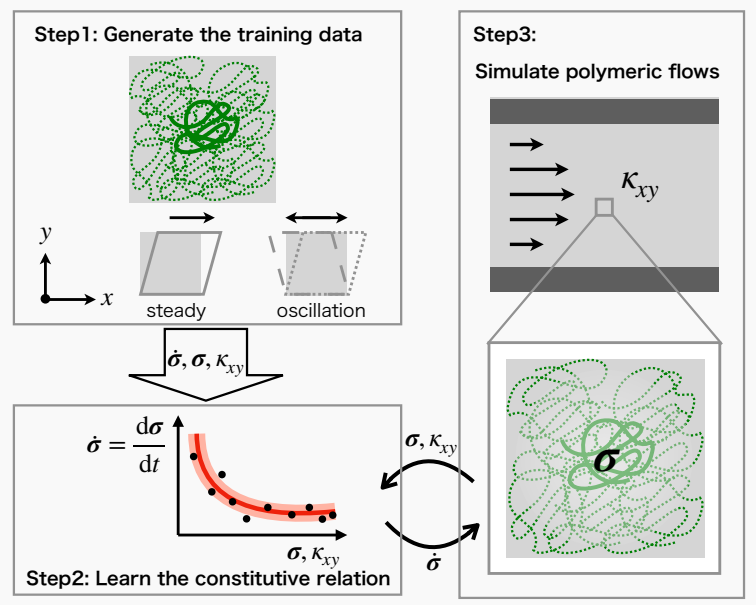

Fig. 2.1 Schematic illustration of the proposed simulation framework for a polymeric fluid with a machine-learned constitutive relation. The application of deformations, here startup steady/oscillatory shears specified by the velocity gradient κ_{xy}, to the targeted microscopic polymer system provides the training data, in the form of the time varying stress $\boldsymbol{\sigma}$ and its time derivative $\dot{\boldsymbol{\sigma}}$, for learning the constitutive relation. The illustration in the bottom left (Step 2), represents the learned relation between $\dot{\boldsymbol{\sigma}}$ and $(\boldsymbol{\sigma}, \kappa_{xy})$, i.e., the constitutive relation. This learned constitutive relation can then be used within a macroscopic flow simulation.

Step 1: Generate the training data
Step 2: Learn the constitutive relation
Step 3: Simulate the macroscopic polymeric flow

The first step, that of generating the training data from the deformations of the polymer system, is described in Section 2.2.1. The second step, for learning of the constitutive relation from the training data, is detailed in Section 2.2.2. Finally, Section 2.2.3 explains how to use the learned constitutive relation to simulate the macroscopic polymeric flows. The flow conditions, geometry, and simulation parameters are detailed in Section 2.2.4. In addition, the implementation details for the microscopic polymer model and the macroscopic fluid solver are given in Appendices 2.B and 2.C, respectively.

2.2.1 Generating the Training Data

The training data is generated from a coarse-grained polymer model (see Appendix 2.B). In particular, we use the sliplink model as a test system to describe microscopic polymer chain dynamics, as it has been extensively studied and confirmed to reproduce the non-linear rheological response of entangled linear polymers[23, 85, 86]. Within this sliplink model, polymer melt systems are characterised by two parameters, the number of entanglements at equilibrium Z_{eq} and the maximum stretch ratio λ_{max} of a chain. The former (Z_{eq}) is proportional to the molecular weight of a constituent polymer chain, the latter (λ_{max}) depends on the rigidity and flexibility of the chain. For simplicity, the molecular weight

distribution of the system is considered to be monodisperse, and we assume the typical values of $Z_{\rm eq} = 10$ and $\lambda_{\rm max} = 4.4$, which correspond to a linear polymer (e.g., polystyrene) of about 100kDa. These values have been taken from one of our previous studies[87].

To prepare the initial state of the polymer chains, we equilibrate the system over several times the longest relaxation time, as evaluated by the linear viscoelastic data, i.e., the storage G' and loss G'' moduli. Then, we subject the system to a deformation with a given velocity gradient. The training data set is generated by considering the response of the system to fundamental shear deformations. The shear deformations (in the $x-y$ plane), with shear rate $\dot{\gamma}(t)$, are expressed as $\kappa_{\alpha\beta}(t) = \dot{\gamma}(t)\delta_{\alpha x}\delta_{\beta y}$. When applying these deformations, it is important to choose "appropriate" strain rates. For determining the magnitudes, we use as reference the longest relaxation time $\tau_{\rm d}$ of the coarse-grained model, as strain rates with this (inverse) magnitude ($\sim 1/\tau_{\rm d}$) will probe the elastic response of viscoelastic fluids.

During training simulations (under the fundamental deformations), we evaluate the stress $\boldsymbol{\sigma}$ as an ensemble average over the conformation of the polymer chains. Let $\boldsymbol{R}^k (k = 1, \ldots, Z)$ denote the positions of the sliplinks on the primitive path of the (linear) polymer chain, with Z the number of entanglement points. The displacement vectors between two adjacent sliplinks along the chain are given by $\boldsymbol{r}^k = \boldsymbol{R}^{k+1} - \boldsymbol{R}^k$ $(k = 1, \ldots, Z-1)$. The stress for an ensemble of such polymer chains can be evaluated in terms of the $\{\boldsymbol{r}\}$ vectors as

$$\boldsymbol{\sigma} = \sigma_{\rm e} \left\langle f \frac{\boldsymbol{r}\boldsymbol{r}}{a|\boldsymbol{r}|} \right\rangle, \tag{2.3}$$

where $\sigma_{\rm e}$ is the unit of stress and f is the FENE parameter. Given that this stress $\boldsymbol{\sigma}$ is defined in terms of the (coarse-grained) molecular conformations, it will naturally express the history dependence on the velocity gradient tensor $\boldsymbol{\kappa}(t)$. The rheological properties of this target system are described in Appendix 2.B (see Figure 2.5).

The training data is generated by considering $N_{\rm gen}$ distinct velocity gradient histories $\{\boldsymbol{\kappa}^1(t), \ldots, \boldsymbol{\kappa}^{N_{\rm gen}}(t)\}$, which are applied to the polymer system, in turn resulting in an equal number of stress trajectories $\{\boldsymbol{\sigma}^1(t), \ldots, \boldsymbol{\sigma}^{N_{\rm gen}}(t)\}$. The time derivative of the stress is then computed by a simple forward difference scheme, such that $\dot{\boldsymbol{\sigma}}(t) \simeq (\boldsymbol{\sigma}(t+h_t) - \boldsymbol{\sigma}(t))/h_t$, where h_t is a suitably small time interval. Finally, the training dataset used to learn the constitutive relations is constructed from the $N_{\rm gen}$ trajectories for the time-derivatives of the stress (training output), together with the corresponding velocity gradient and stress data (training input), i.e., $\{\boldsymbol{\kappa}(t), \boldsymbol{\sigma}(t), \dot{\boldsymbol{\sigma}}(t)\}$. We note that the $N_{\rm gen}$ trajectories, each corresponding to a different velocity gradient history $\boldsymbol{\kappa}(t)$, were initialized with different random initial states, and equilibrated over times t longer than the longest relaxation time $\tau_{\rm d}$ $(t > 10\,\tau_{\rm d})$.

2.2.2 Learning the Constitutive Relation

To learn the constitutive relation, we rely on Gaussian Processes, which provide a probability distribution over functions, and can be used as universal function approximators[88]. For the current case, the time derivative of stress is assumed to be a function of the stress and velocity-gradient, as given by the following GP prior:

$$\dot{\boldsymbol{\sigma}} = \dot{\boldsymbol{\sigma}}(\boldsymbol{\sigma}, \boldsymbol{\kappa}) \sim \mathcal{N}(\boldsymbol{\mu}, \boldsymbol{K}), \tag{2.4}$$

where $\mathcal{N}(\cdot, \cdot)$ denotes a multi-variate normal distribution, with mean $\boldsymbol{\mu}$ and covariance $\boldsymbol{K}$. Under the assumption of Eq. (2.4), a GP regression provides a Bayesian framework capable of inferring the time derivative of the stress when the stress and velocity gradient are given. For the GP regression, we randomly select $N_{\rm train}$ input points from the $N_{\rm gen}$ molecular-based trajectories, where each point consists

of a set of values $(\boldsymbol{\kappa}, \boldsymbol{\sigma}, \dot{\boldsymbol{\sigma}})$. The N_{train} training input points $\boldsymbol{x} \equiv [\boldsymbol{\sigma}, \boldsymbol{\kappa}]$ are collected into a so-called design matrix $\boldsymbol{X}(= [\boldsymbol{x}_1, \ldots, \boldsymbol{x}_{N_{\text{train}}}])$. Then, let $\boldsymbol{X}^*$ be the test input points, for which we want to predict the constitutive relation, i.e., the corresponding $\dot{\boldsymbol{\sigma}}^*$, the joint GP for $(\dot{\boldsymbol{\sigma}}, \dot{\boldsymbol{\sigma}}^*)$ is given as

$$\begin{bmatrix} \dot{\boldsymbol{\sigma}} \\ \dot{\boldsymbol{\sigma}}^* \end{bmatrix} \sim \mathcal{N}\left(\begin{bmatrix} \boldsymbol{\mu}(\boldsymbol{X}) \\ \boldsymbol{\mu}(\boldsymbol{X}^*) \end{bmatrix}, \begin{bmatrix} \boldsymbol{K}(\boldsymbol{X}, \boldsymbol{X}), & \boldsymbol{K}(\boldsymbol{X}, \boldsymbol{X}^*) \\ \boldsymbol{K}(\boldsymbol{X}^*, \boldsymbol{X}), & \boldsymbol{K}(\boldsymbol{X}^*, \boldsymbol{X}^*) \end{bmatrix} \right), \tag{2.5}$$

where the p-th component of the mean is $(\boldsymbol{\mu}(\boldsymbol{X}))_p = \mu(\boldsymbol{x}_p)$ and the (p, q)-th component of the covariance matrix is $(\boldsymbol{K}(\boldsymbol{X}, \boldsymbol{X}))_{pq} = k(\boldsymbol{x}_p, \boldsymbol{x}_q; \boldsymbol{\Theta})$ ($\boldsymbol{\Theta}$ the kernel hyper-parameters), for mean function $\mu(\cdot)$ and kernel function $k(\cdot, \cdot)$. The (output) prediction for these test points $\boldsymbol{X}^*$, conditioned on the known training data $(\boldsymbol{X}, \dot{\boldsymbol{\sigma}})$, is given by the posterior probability distribution for $\dot{\boldsymbol{\sigma}}^*$, which is yet another GP[88]

$$\dot{\boldsymbol{\sigma}}^* | \dot{\boldsymbol{\sigma}} \sim \mathcal{N}(\boldsymbol{\nu}, \boldsymbol{\Sigma}), \tag{2.6}$$

$$\boldsymbol{\nu} = \boldsymbol{\mu}^* + \boldsymbol{K}^* \cdot \boldsymbol{K}^{-1} \cdot (\dot{\boldsymbol{\sigma}} - \boldsymbol{\mu}), \tag{2.7}$$

$$\boldsymbol{\Sigma} = \boldsymbol{K}^{**} - \boldsymbol{K}^* \cdot \boldsymbol{K}^{-1} \cdot {}^t\boldsymbol{K}^*, \tag{2.8}$$

where we use the shorthand notation $\boldsymbol{\mu} = \boldsymbol{\mu}(\boldsymbol{X})$, $\boldsymbol{\mu}^* = \boldsymbol{\mu}(\boldsymbol{X}^*)$, $\boldsymbol{K} = \boldsymbol{K}(\boldsymbol{X}, \boldsymbol{X})$, $\boldsymbol{K}^* = \boldsymbol{K}(\boldsymbol{X}^*, \boldsymbol{X})$, and $\boldsymbol{K}^{**} = \boldsymbol{K}(\boldsymbol{X}^*, \boldsymbol{X}^*)$. Without loss of generality $\mu(\cdot)$ can be set to zero, and the kernel function $k(\cdot, \cdot; \cdot)$ can be constructed from a list of known candidate functions.

Eqs.(2.6-2.8) provide the "best" estimate for the test prediction $\dot{\boldsymbol{\sigma}}^*$ (given by $\boldsymbol{\nu}$), conditioned on the training data set, as well as an estimate for its uncertainty (given by $\boldsymbol{\Sigma}$). These predictions depend on the full set of training data, as well as on the unspecified kernel hyper-parameters $\boldsymbol{\Theta}$. Thus, the first step in the GP regression consists of learning the "optimal" hyper-parameters $\boldsymbol{\Theta}_{\text{opt}}$ from the training data $(\boldsymbol{X}, \dot{\boldsymbol{\sigma}})$ (this is akin to optimizing for the weights and biases of a neural-network). Specifically, we seek to maximize the (log) posterior probability for the hyper-parameters, given the training data, i.e., $\text{Prob}(\boldsymbol{\Theta} | \boldsymbol{X}, \dot{\boldsymbol{\sigma}})$. From Bayes' theorem we have $\text{Prob}(\boldsymbol{\Theta} | \boldsymbol{X}, \dot{\boldsymbol{\sigma}}) \propto \text{Prob}(\dot{\boldsymbol{\sigma}} | \boldsymbol{X}, \boldsymbol{\Theta}) \text{Prob}(\boldsymbol{\Theta})$, where the likelihood $\text{Prob}(\dot{\boldsymbol{\sigma}} | \boldsymbol{X}, \boldsymbol{\Theta})$ is given by the GP of Eq. (2.6), and the prior is assumed constant, $\text{Prob}(\boldsymbol{\Theta}) = \text{const}$, such that

$$\boldsymbol{\Theta}_{\text{opt}} = \text{argmax}_\theta \left[\log \text{Prob}(\dot{\boldsymbol{\sigma}} | \boldsymbol{X}, \boldsymbol{\Theta}) \right]. \tag{2.9}$$

2.2.3 Predicting the Polymeric Flow

We now describe the MSS framework we have utilized to predict the macroscopic flow of an incompressible polymeric fluid. The momentum transport, Eq. (2.2), can be rewritten as

$$\frac{\mathcal{D}\boldsymbol{v}}{\mathcal{D}t} = \frac{1}{\rho} \boldsymbol{\nabla} \cdot (\boldsymbol{\sigma}_{\text{t}} - P\boldsymbol{I}) + \frac{\boldsymbol{F}}{\rho}, \tag{2.10}$$

$$\boldsymbol{\sigma}_{\text{t}} = \boldsymbol{\sigma} + \boldsymbol{\sigma}_{\text{d}}, \tag{2.11}$$

$$\boldsymbol{\sigma}_{\text{d}} = \eta_{\text{d}} (\boldsymbol{\kappa} + {}^t\boldsymbol{\kappa}), \tag{2.12}$$

where $\boldsymbol{v}$ is the fluid velocity, ρ the constant fluid density, $\boldsymbol{\sigma}_{\text{t}}$ the total stress, including the polymer $\boldsymbol{\sigma}$ and the additional dissipative $\boldsymbol{\sigma}_{\text{d}}$ contributions, η_{d} is the viscosity due to thermal dissipation at scales below that of the sliplink dynamics, i.e., occurring at spatial scales smaller than the entanglement distance, $\boldsymbol{\kappa} = {}^t(\nabla \boldsymbol{v})$ is the velocity gradient tensor, i.e., $\kappa_{\alpha\beta} = \nabla_\beta v_\alpha (\alpha, \beta \in \{x, y\})$, P is the pressure, and $\boldsymbol{F}$ the

external force driving the flow. These equations are solved within a Lagrangian framework, using the smoothed particle hydrodynamics method (see Appendix 2.C).

Traditionally, when simulating the momentum transport of such complex fluids, the stress tensor would be evaluated either by (i) a constitutive equation or (ii) a molecular-based model. The standard MSS approach is to directly embed a (ii) molecular-based simulator inside each of the Lagrangian fluid particles, and evaluate the stress as an ensemble average over the conformation of the polymer chains in each simulator (i.e., fluid particle). Instead, our proposed ML scheme removes the microscopic simulators, and instead directly introduces the stress field $\boldsymbol{\sigma}(t)$, together with (iii) a machine-learned constitutive relation for $\dot{\boldsymbol{\sigma}}(\boldsymbol{\sigma}, \boldsymbol{\kappa})$ (which provides the necessary information to update the stress field). The stress $\boldsymbol{\sigma}(t)$ at time t, for each Lagrangian particle, is simply integrated in time following

$$\boldsymbol{\sigma}(t + \Delta t) = \boldsymbol{\sigma}(t) + \dot{\boldsymbol{\sigma}}(\boldsymbol{\sigma}(t), \boldsymbol{\kappa}(t))\Delta t, \tag{2.13}$$

where Δt is the macroscopic time-step. The local velocity gradient at the particle position, evaluated by solving for the macroscopic flow, will deform the embedded microscopic polymer system, in such a way that the polymer confirmation will depend on the history of the flow. Concurrently, the momentum field at the macroscopic scale is updated by taking into account the polymer contributions to the stresses over the entire system. To summarize, the velocity gradient and stress couple the dynamics of the system at two scales, corresponding to the (macroscopic) fluid flow and the (microscopic) polymer chain dynamics.

The Macroscopic and the microscopic time, stress, and length scales have characteristic units of $t^{(\mathrm{M})}, \sigma^{(\mathrm{M})}, \ell^{(\mathrm{M})}$, and $t^{(\mathrm{m})}, \sigma^{(\mathrm{m})}$, and $\ell^{(\mathrm{m})}$, respectively. The superscripts "M" and "m" refer to the macroscopic and the microscopic scale, respectively. The microscopic units are defined by the relaxation time τ_{e} of a strand (the segment between two connected entanglement points), the stress associated to the plateau modulus σ_{e}, and the thermal equilibrium length a of a strand. The macroscopic units of length $\ell^{(\mathrm{M})}$ are the diameter of the Lagrangian particle b, while the time $t^{(\mathrm{M})}$ and stress $\sigma^{(\mathrm{M})}$ units will be determined from the fluid parameters and the corresponding microscopic units, τ_{e} and σ_{e}.

2.2.4 ML-Based MSS Parameters for Well-Entangled Polymer Melt Flows

In a previous study [55], our proposed method has been verified for the case of a linear constitutive relation applied to a uni-deformation mode flow, i.e., a shear flow. Here, we extend the method to consider a microscopic model with a realistic non-linear constitutive relation, and use this Machine-Learned (non-linear) constitutive relation to simulate flows with a single (shear) deformation mode. As utilized in the previous work, we will consider as test flow that of a pressure driven flow between two parallel plates. In the laminar (low Reynolds number) regime, pressure gap driven flows in 2D (xy-plane) only show shear deformations, with $\kappa_{\alpha\beta}(t) = \dot{\gamma}(t)\delta_{\alpha x}\delta_{\beta y}$. Thus, it is enough to only consider such shear deformations in the xy-plane when generating the training data. The learned relations are the time derivatives $\dot{\sigma}_{xx}(t)$, $\dot{\sigma}_{xy}(t)$, and $\dot{\sigma}_{yy}(t)$ for the stress, as a function of the stress and the shear strain $\{\sigma_{xx}, \sigma_{xy}, \sigma_{yy}, \dot{\gamma}\}$, i.e., the three GPs to be learned are $\dot{\sigma}_{xx}(\boldsymbol{\sigma}, \dot{\gamma}), \dot{\sigma}_{xy}(\boldsymbol{\sigma}, \dot{\gamma})$, and $\dot{\sigma}_{yy}(\boldsymbol{\sigma}, \dot{\gamma})$. In this case, Eq. (2.13) can be simplified as follows,

$$\boldsymbol{\sigma}(t + \Delta t) = \boldsymbol{\sigma}(t) + \dot{\boldsymbol{\sigma}}(\boldsymbol{\sigma}(t), \dot{\gamma}(t))\Delta t. \tag{2.14}$$

Table 2.1 shows the simulation parameters for the pressure gap driven flow between two parallel plates. The macroscopic geometry is expressed by the periodic length L_x and the distance between the two plates

Table 2.1 Simulation parameters for planar Poiseuille flow.

Parameter	Description	Value
Δt	time-step	$0.001t^{(\mathrm{M})}$
(L_x, L_y)	system size	$(20\ell^{(\mathrm{M})},40\ell^{(\mathrm{M})})$
$\hat{F}_x$	external force	0.02
τ_d	relaxation time	$40\ t^{(\mathrm{M})}$
η_t	total viscosity	$40\ \sigma^{(\mathrm{M})}t^{(\mathrm{M})}$
β	viscosity ratio	0.1

L_y. The system is initially at rest at time $t = 0$, with the microscopic systems thermally equilibrated. Then, for $t > 0$, the non-dimensionalized external force $\hat{F}_x$, mimicking the pressure gradient, drives the fluid between the plates. The equations of motion are integrated forward in time, with a time-step Δt. At the macroscopic scale, the viscoelasticity of the fluid is characterized by the longest relaxation time τ_d, the total viscosity $\eta_\mathrm{t}(= \eta_\mathrm{p} + \eta_\mathrm{d})$, and the viscosity ratio $\beta(= \eta_\mathrm{d}/\eta_\mathrm{t})$, where η_p and η_d are the polymer and dissipative viscosity, respectively. Here, $\tau_\mathrm{d}/t^{(\mathrm{m})}$ and $\eta_\mathrm{p}/(\sigma^{(\mathrm{m})}t^{(\mathrm{m})})$ are determined by the linear rheology of the microscopic system (see Appendix 2.B), with the corresponding parameters at the macroscopic scale given as $\tau_\mathrm{d}/t^{(\mathrm{M})}$ and $\eta_\mathrm{p}/(\sigma^{(\mathrm{M})}t^{(\mathrm{M})})$.

We have chosen parameter values for a typically viscoelastic condition. The relevant non-dimensional numbers are the apparent Reynolds number $\mathrm{Re}^{(\mathrm{a})}$ and the Weissenberg number $\mathrm{Wi}^{(\mathrm{a})}$, defined as

$$\mathrm{Re}^{(\mathrm{a})} = \frac{\rho_0 L_y U_\mathrm{max}}{\eta_\mathrm{t}}, \tag{2.15}$$

$$\mathrm{Wi}^{(\mathrm{a})} = \frac{U_\mathrm{max}\tau_\mathrm{d}}{L_y}. \tag{2.16}$$

Using $\mathrm{Re}^{(\mathrm{a})}$ and $\mathrm{Wi}^{(\mathrm{a})}$, we define the elasticity number as

$$\mathrm{El} = \frac{\mathrm{Wi}^{(\mathrm{a})}}{\mathrm{Re}^{(\mathrm{a})}} = \frac{\tau_\mathrm{d}\eta_\mathrm{t}}{\rho_0 L_y^2}, \tag{2.17}$$

where $U_\mathrm{max}(= \max(v_x))$ is the maximum velocity in the flow direction at steady state, as evaluated from the simulations. As an example, consider a Hookean dumbbell model in the infinite dumbbell limit, with a single relaxation mode (τ_d, η_p), such that the constitutive relation follows the upper convected Maxwell model

$$\left(1 + \tau_\mathrm{d}\frac{\delta}{\delta t}\right)\boldsymbol{\sigma} = \eta_\mathrm{p}(\boldsymbol{\kappa} + {}^t\boldsymbol{\kappa}), \tag{2.18}$$

with $\delta/\delta t$ is the upper convected derivative. In this case, the parameters of Table 2.1 would be given as $U_\mathrm{max} = 0.1$, $\mathrm{Re}^{(\mathrm{a})} = 0.1$ and $\mathrm{Wi}^{(\mathrm{a})} = 0.1$ ($\mathrm{El} = 1$). We have used this typical viscoelastic problem to validate the macroscopic fluid solver (see Fig. 2.6 of Appendix 2.C for the results).

The Lagrangian particles are initially arranged on a regular grid, with a spacing equal to the particle diameter b. Thus, the total number of fluid particles is $800(= L_x L_y/b^2)$, using the values described in Table 2.1. The simulations are performed using a parallelized solver, allowing us to perform the calculations for both macroscopic and microscopic scales simultaneously. For the current flow problem, a single 40-core CPU is assigned to handle both macroscopic and microscopic parts simultaneously. We note that the computational load of the macroscopic SPH fluid solver is significantly less than that of the (ML) constitutive relation predictions, which are themselves overshadowed by the cost of including the

explicit microscopic degrees of freedom within the conventional MSS. In other words, the computational bottleneck for the ML and MSS calculations is the same, i.e., the stress calculation.

2.3 Results and Discussion

This section describes the simulation results for the pressure gap driven flows between two parallel plates. We test the applicability of our proposed ML approach to simulate a realistic polymer model, one with a non-linear constitutive relation, under uni-deformation shear mode flows. The performance, as measured by the accuracy and computational cost compared to the conventional MSS method, is analyzed for the typical viscoelastic flow problem characterized by the parameters shown in Table 2.1.

2.3.1 Learning the Constitutive Relation under Shear Flow

For generating the training data, we applied a time-dependent (shear) velocity gradient to a microscopic polymer system, composed of $N_{\rm p} = 10^4$ polymer chains. We consider two types of flow profiles, (1) constant start-up and (2) oscillatory shear flows, with shear rates $\dot{\gamma}(t) = \dot{\gamma}_0 H(t)$ and $\dot{\gamma}(t) = \gamma_{\rm max}\omega\cos(\omega t)$, respectively, where $H(t)$ is the Heaviside step function, $\dot{\gamma}_0$ the constant shear rate, $\gamma_{\rm max}$ the maximum strain, and ω the angular frequency. We consider $N_{\dot{\gamma}} = 12$ different shear strain (rate) magnitudes $\dot{\gamma}_0^1, \ldots, \dot{\gamma}_0^{N_{\dot{\gamma}}}$ and $\gamma_{\rm max}^1, \ldots, \gamma_{\rm max}^{N_{\dot{\gamma}}}$, evenly spaced on a logarithmic scale within the range $\dot{\gamma}_0, \gamma_{\rm max}\omega \in [10^{-1}/\tau_{\rm d}, 10^1/\tau_{\rm d}]$. For the oscillatory flow, we used a fixed angular frequency $\omega = 1/\tau_{\rm d}$ for all shear strains. In total, we used $N_{\rm gen} = 4N_{\dot{\gamma}}$ time series, for the positive/negative $N_{\dot{\gamma}}$ shear rates, for both the startup and oscillatory flows, each generated by a different velocity gradient history. The simulations were performed up to $t = 10\tau_{\rm d}$, starting from an equilibrated state at $t = 0$, with a time-step $h_t = t^{(\rm m)}$. The resulting trajectory data $\{\dot{\sigma}_{xx}(t), \dot{\sigma}_{xy}(t), \dot{\sigma}_{yy}(t), \sigma_{xx}(t), \sigma_{xy}(t), \sigma_{yy}, \dot{\gamma}(t)\}$ are smoothed by a simple moving average

$$\tilde{t} = \frac{1}{N_{\rm sm}} \sum_{j=1}^{N_{\rm sm}} (t + (j-1)h_t), \tag{2.19}$$

$$\tilde{X} = \frac{1}{N_{\rm sm}} \sum_{j=1}^{N_{\rm sm}} X(t + (j-1)h_t), \tag{2.20}$$

where $X(t)$ is the time series data, $\tilde{X}$ ($\tilde{t}$) the smoothed dynamical variable (time), and $N_{\rm sm}$ the averaging window size. From this smoothed $\tilde{X}(\tilde{t})$, with $N_{\rm sm} = 5$, we randomly choose $N_{\rm train} \sim 3 \times 10^3$ data points to serve as the training data. For the current flow problem, this number is large enough to generate an adequate sampling of the constitutive equation space, in order to learn the functions, while limiting the calculation time of the GP prediction. While simply increasing $N_{\rm train}$ can improve the accuracy, it is also important to consider the training protocol used to generate the training data.

For learning the constitutive relation, we use a GP regression to "learn" the functions $\dot{\sigma}_{xx}$, $\dot{\sigma}_{xy}$, and $\dot{\sigma}_{yy}$, from the input $\boldsymbol{x} = [\kappa_{xy}, \sigma_{xx}, \sigma_{xy}, \sigma_{yy}]$. Each $\dot{\sigma}_{\alpha\beta}$ is specified as a separate GP, with covariance matrix $K_{\alpha\beta}(\boldsymbol{X}, \boldsymbol{X})$, whose entries are given by $K_{\alpha\beta}(\boldsymbol{X}, \boldsymbol{X})_{ij} = k(\boldsymbol{X}_i, \boldsymbol{X}_j) + \epsilon^2\delta_{ij}$, assuming a constant (but unknown) measurement error ϵ. For the kernel function $k(\boldsymbol{x}, \boldsymbol{x}')$ we adopt the following ansatz

$$\begin{aligned} k(\boldsymbol{x}, \boldsymbol{x}') =& \Theta_\eta k_{\rm M}(\kappa_{xy}, \kappa'_{xy}; \Theta_{\kappa_{xy}}) \times \\ & k_{\rm M}([\sigma_{xx}, \sigma_{yy}, \sigma_{xy}], [\sigma'_{xx}, \sigma'_{yy}, \sigma'_{xy}]; \boldsymbol{\Theta}_{\boldsymbol{\sigma}}), \end{aligned} \tag{2.21}$$

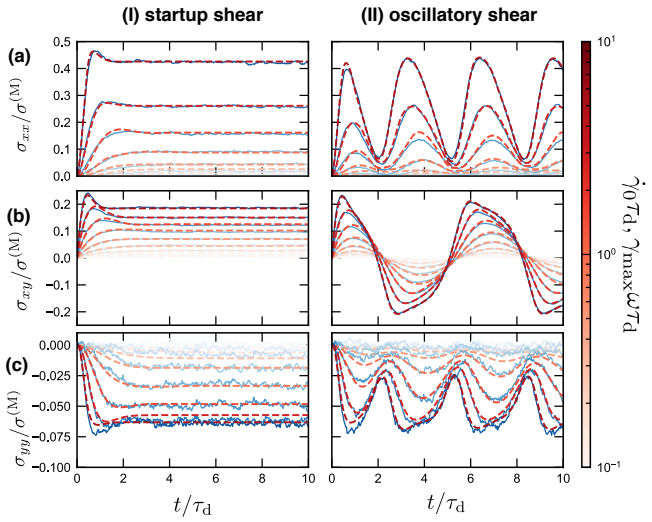

Fig. 2.2 The predictions for the stress responses, (a) $\sigma_{xx}(t)$, (b) $\sigma_{xy}(t)$, and (c) $\sigma_{yy}(t)$, under (I) the startup shear flows and (II) the oscillatory flows for ten different shear rates, evenly spaced on a logarithmic axis, such that $\dot{\gamma}_0, \gamma_{\max}\omega \in [10^{-1}/\tau_{\rm d}, 1\cdot 10^{1}/\tau_{\rm d}]$. The solid blue lines are the time series of the stress with the microscopic polymer system thermally equilibrated at $t=0$ (10^4 polymer chains) and the dashed red lines are those obtained from the machine-learned constitutive relations for $\dot{\sigma}_{xx}$, $\dot{\sigma}_{xy}$, and $\dot{\sigma}_{yy}$. Lighter (darker) colors are used to represent lower (higher) values of the applied shear-rates, $\dot{\gamma}_0, \gamma_{\max}\omega$. Note that the higher absolute magnitudes of the stresses (σ_{xx},σ_{xy},σ_{yy}) correspond to the higher shear rates.

where Θ_η is the amplitude hyper-parameter, and $\Theta_{\kappa_{xy}}$ and $\boldsymbol{\Theta}_{\boldsymbol{\sigma}} = (\Theta_{\sigma_{xx}}, \Theta_{\sigma_{yy}}, \Theta_{\sigma_{xy}})$ are the length-scale hyper-parameters. Since our training data contains the sharp stress response of the startup shear, we use the (twice-differentiable) Matern5/2 kernel,

$$k_{\rm M}(\boldsymbol{x}, \boldsymbol{x}'; \boldsymbol{\Theta}_\ell) = \left(1 + \sqrt{5}d + \frac{5}{3}d^2\right)\exp\left(-\sqrt{5}d\right), \tag{2.22}$$

$$\text{where } d = {}^t(\boldsymbol{x} - \boldsymbol{x}')\mathrm{diag}(\boldsymbol{\Theta}_\ell)^{-2}(\boldsymbol{x} - \boldsymbol{x}'), \tag{2.23}$$

with $\mathrm{diag}(\boldsymbol{\Theta}_\ell)$ the diagonal matrix constructed from the vector of hyper-parameters $\boldsymbol{\Theta}_\ell$. The three GPs for $\dot{\sigma}_{xx}$, $\dot{\sigma}_{xy}$, and $\dot{\sigma}_{yy}$ are independently trained, each with a different set of hyper-parameters. For this, we use the standard ADAM optimizer to tune the hyper-parameters $\boldsymbol{\Theta}= (\epsilon, \Theta_\eta, \Theta_{\kappa_{xy}}, \boldsymbol{\Theta}_{\boldsymbol{\sigma}})$, based on Eq. (2.9), as implemented within the GPyTorch package[89] (itself based on the PyTorch framework [90]).

To verify the applicability of the learned constitutive relations, we confirm that they are able to accurately describe the flow under (I) start-up shear flows ($\dot{\gamma}(t) = \dot{\gamma}_0 H(t)$) and (II) oscillatory shear flows ($\dot{\gamma}(t) = \gamma_{\max}\omega\cos(\omega t)$) for $\dot{\gamma}$ values not included in the training data. As shown in Fig. 2.2, we successfully reproduced the stress responses (a) $\sigma_{xx}(t)$, (b) $\sigma_{xy}(t)$, and (c) $\sigma_{yy}(t)$, for ten different shear rates, evenly spaced on a logarithmic axis, such that $\dot{\gamma}_0, \gamma_{\max}\omega \in [10^{-1}/\tau_{\rm d}, 10^{1}/\tau_{\rm d}]$. The solid blue lines show the time series for the stress obtained from the microscopic simulations of the sliplink systems with 10^4 polymer chains, while the dashed red lines show the results obtained using the machine-learned constitutive relations for $\dot{\sigma}_{xx}$, $\dot{\sigma}_{xy}$, and $\dot{\sigma}_{yy}$. The higher absolute magnitudes of (σ_{xx},σ_{xy},σ_{yy}) are from the higher shear rates with $\dot{\gamma}_0, \gamma_{\max}\omega$.

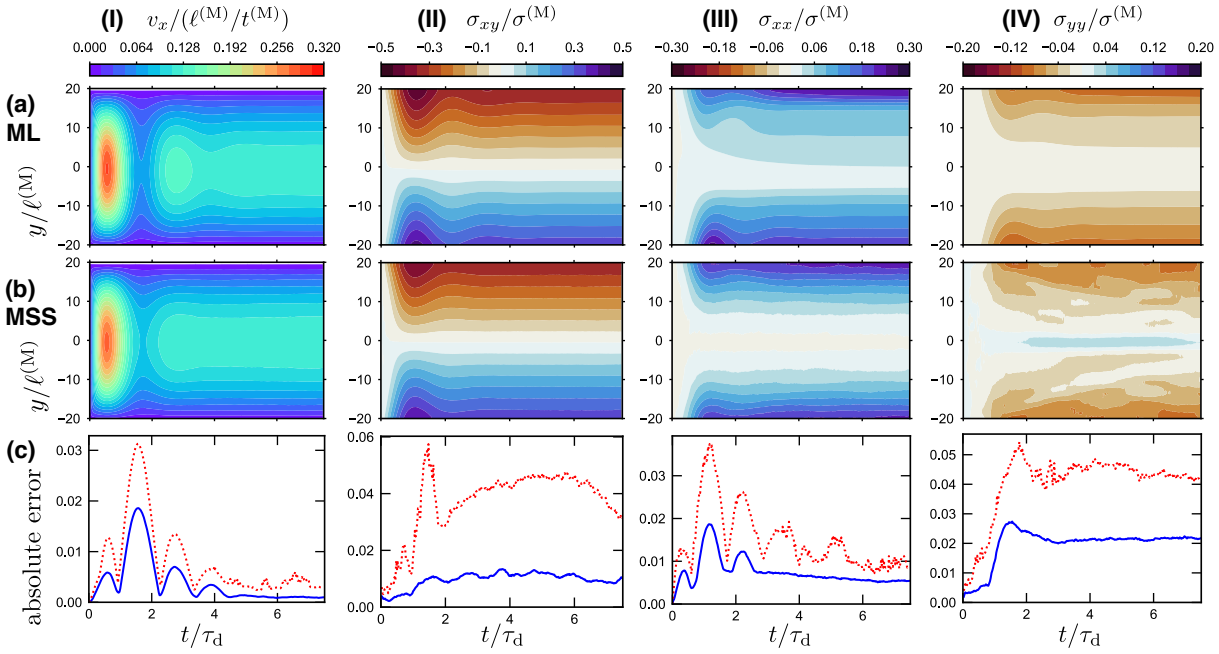

Fig. 2.3 Predictions for the pressure gap driven flow were obtained using (a) the machine-learned constitutive relation, trained on microscopic systems under steady/oscillatory shear flows, and (b) the full MSS, using embedded microscopic simulators (10^4 polymer chains per Lagrangian particle), together with (c) The absolute error between the two simulation results. In the bottom panels (c), the dotted red lines show the maximum absolute error, the solid blue lines the average error values. From left to right, the columns correspond to (I) the velocity along the flow direction v_x, and (II) the σ_{xy}, (III) σ_{xx}, and (IV) σ_{yy} components of the stress.

The learned constitutive relation, given by the three GPs, accurately reproduces the non-linear behaviors of the shear stress, i.e., the overshoots at the early time and the shear thinning at the steady state (see Fig. 2.2). Thus, it is expected to reproduce the flow response for typical shear flows over a wide range of deformation rates, around the inverse of the characteristic relaxation time $[10^{-1}/\tau_{\mathrm{d}}, 10^{1}/\tau_{\mathrm{d}}]$. Note that when considering the dumbbell model[55], which has a linear constitutive relation, the stress responses all exhibit the same shape, regardless of the magnitude of the shear rate $\dot{\gamma}(t)$, in contrast to the results obtained here. This makes it more challenging to learn the constitutive relations. While we obtain very good overall agreement, some of the stress responses show small deviations from the reference (MSS) trajectories. This is due to the random/sparse sampling of the training data, which makes sampling around the first overshoot/undershoot, where these deviations are most noticeable, more difficult (compared to sampling of the steady-state response). If required, one could protect against this type of error by employing a more robust active-learning / data-driven approach, in which training points are selectively added in order to reduce the prediction uncertainty of the GP[54].

2.3.2 Application to Pressure Gap Driven Flows

The pressure gap driven flow has been simulated using the ML constitutive relation with the parameters given in Table 2.1. As a reference, we also conducted full MSS simulations, with $N_{\mathrm{p}} = 10^4$ polymer chains per Lagrangian particle, in order to ensure high numerical accuracy. Our results are summarized in Fig.

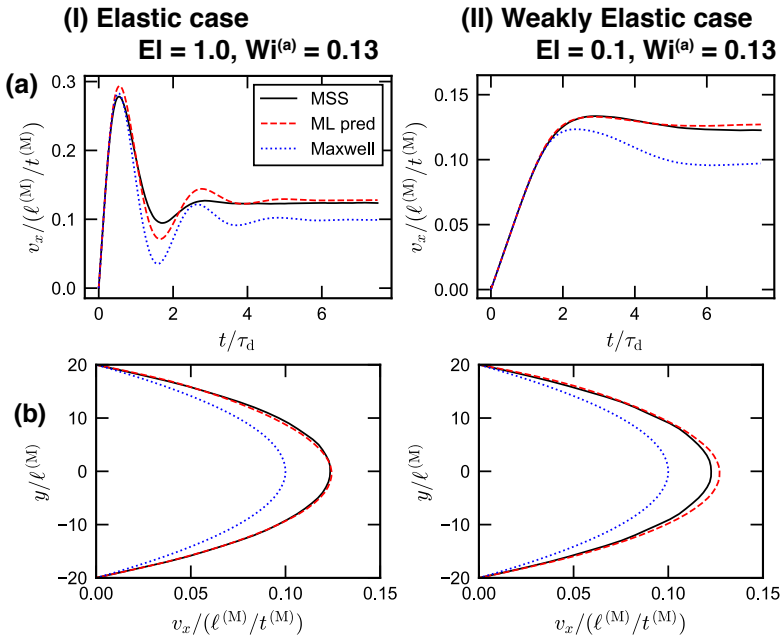

Fig. 2.4 (a) The time series of the velocity v_x along the center line $y = 0$. (b) The steady state velocity v_x as a function of height. (I) The graphs on the left show the elastic case with $\mathrm{El} = 1.0, \mathrm{Wi}^{(\mathrm{a})} = 0.13$ using the parameters shown in Table 2.1, whereas those on (II) the right show a weakly elastic case, with $\mathrm{El} = 0.1$ and $\mathrm{Wi}^{(\mathrm{a})} = 0.13$. The parameters for case (II) are the same as those of (I), expect for a change in the total viscosity $\eta_\mathrm{t} = 4.0$ and the external force $\hat{F}_x = 0.002$. Solid black lines and dashed red lines are the simulation results using the microscopic simulators of the sliplink model and the machine-learned constitutive relation, respectively. Blue dotted lines are the results of the upper convected Maxwell model having the same value of the zero shear viscosity and the longest relaxation time of the sliplink system.

2.3, which shows the flow and stress predictions obtained using (a) the learned constitutive relation and (b) the full MSS, as well as (c) the absolute error between the two. In particular, we show (I) the velocity along the channel direction v_x and (II) the σ_{xy}, (III) σ_{xx}, and (IV) σ_{yy} components of the stress. In the bottom panels (c), the dotted red lines give the time series for the maximum absolute error, as a function of the height y, the solid blue lines give the corresponding averaged absolute errors.

Our predictions using the learned constitutive relation are in very good agreement with the reference MSS values, i.e., we can reproduce the early-time $t/\tau_\mathrm{d} < 6$ oscillations in the velocity v_x, and the σ_{xy} and σ_{xx} components of the stress, as well as their steady state values (see Fig. 2.3). The maximum (instantaneous) relative errors for σ_{xy}, and σ_{xx} are at most $\sim 10\%$, with the absolute error an order of magnitude smaller than the average value of the quantity under consideration. While the absolute error for the σ_{yy} predictions is of the same order as those of σ_{xy} and σ_{xx}, the relative error is considerably higher. However, this is not an issue, as the σ_{yy} component plays no role in the shear flows used for the training or test cases. Thus, we conclude that the learned constitutive relation properly tracks the relevant variables for the typical viscoelastic flow problem we have studied. Furthermore, this indicates that the proposed ML scheme is accurate enough to provide quantitative predictions for entangled polymer melt flows.

For a more detailed comparison, Fig. 2.4 shows (a) the time evolution of the velocity v_x along the

center line $y = 0$, and (b) the steady-state velocity profile v_x as a function of height along the channel. We show results for (I) the moderately elastic case, with $\mathrm{El} = 1.0$ and $\mathrm{Wi}^{(\mathrm{a})} = 0.13$, and (II) the weakly elastic case, with $\mathrm{El} = 0.1$ and $\mathrm{Wi}^{(\mathrm{a})} = 0.13$. The former corresponds to the default parameters shown in Table 2.1, while the latter updates the values of the total viscosity $\eta_{\mathrm{t}} = 4.0$ and the external force $\hat{F}_x = 0.002$ (all other parameters being equal). The solid black lines and dashed red lines show the simulation results using the full MSS (microscopic sliplink model) and the machine-learned constitutive relation, respectively. In addition, we have also plotted the results for the upper convected Maxwell model having the same values for the zero-shear viscosity and the relaxation time scale (equal to that longest relaxation time of the sliplink model).

In the transient regime, as shown in Fig. 2.4 (a-I), the time evolution of the velocity v_x exhibits clear oscillations. The first undershoot is predicted to occur at the same time $t/\tau_{\mathrm{d}} \simeq 1.8$ by both the ML and MSS approaches, however, the amplitude of this undershoot is larger in the ML results, and approaches that of the Maxwell model. This is due to the presence of higher order modes of relaxation in the microscopic sliplink model, compared to the longest relaxation mode of the upper convected Maxwell model, originating in the constraint release mechanism. The learning of $\dot{\boldsymbol{\sigma}}(\boldsymbol{\sigma}, \boldsymbol{\kappa})$ can safely overlook responses with high relaxation modes, since these are only observed under large deformation rate startup shears, and would be more expensive to properly sample. For weakly elastic conditions, the stress responses (a-II) have a reduced oscillation amplitude, compared to that of the elastic case, and the ML predictions show a higher degree of accuracy.

In the steady state, as shown in Figs. 2.4 (b-I) and (b-II), the maximum velocity $\max(v_x)$ is $U_{\max} = 0.13$, at $y = 0$. This value is considerably larger than that of the linear viscoelastic fluid ($U_{\max} = 0.1$), as given by the Maxwell constitutive relation (Eq. (2.18)). This enhanced velocity is due to the non-linear phenomenon of shear thinning. Using the value of $U_{\max}$, the non-dimensional parameters are $\mathrm{Re}^{(\mathrm{a})} = \mathrm{Wi}^{(\mathrm{a})} = 0.13$. Here, we have investigated a typical viscoelastic case with $\mathrm{El} = 1$, for more viscous systems, with smaller elastic numbers $\mathrm{El} < 1$, we expected the learned constitutive relations to provide accurate descriptions, as they cover the linear regime by construction.

We now discuss the computational efficiency of the ML approach. With regards to the flow simulations, the full MSS, using the embedded microscopic simulators, requires a considerably large computation cost. For the results presented here, this amounted to $\simeq 21$ hours, using a single 40-core CPU and 12 GB size of memory, with the microscopic simulators accounting for $\sim 99\%$ of all the computation time. In contrast, the ML-based simulation can run on the same CPU with 2 GB memory size, and takes only $\simeq 2$ hours, i.e., it is roughly an order of magnitude faster with 1/6 times memory consumption. In fact, we can also ignore the (one-time) cost of training/learning the constitutive relation, as it requires negligible resources (for $N_{\mathrm{train}} \sim 10^3$). Furthermore, if/when larger datasets are required (e.g., 3D systems and/or complex flows), the learning can be significantly accelerated by using GPUs.

2.3.3 Limitation

While our results clearly show the promise of accelerating the state-of-the-art MSS for complex flows using ML, the proposed method has some potential limitations that should be addressed in future work. First, we need to design custom time-dependent velocity gradient profiles in order to generate a curated training dataset that adequately explores the constitutive relation space (for the target flow problem). Second, we have neglected higher-order time derivatives of the stress in the assumed form of the constitutive equation. Additionally, it is not clear whether or not the stress is enough to completely

track the conformation of the coarse-grained molecules (i.e., additional descriptors might be required). Furthermore, when learning the multi-mode relaxation for higher Rouse modes or polydisperse polymer systems, when the system has well-separated relaxation times, the values of the strain rates should be carefully chosen, so as to grasp both the slow and fast relaxation modes. Finally, for more complex 2D/3D flows, the frame invariance of the stress should be incorporated into the GP regression model. These issues will be addressed in future work.

2.4 Conclusion

In the present study, we have successfully applied a simulation scheme [55] using a machine learned constitutive relation to well-entangled polymer systems. As a typical example of a complex fluid with a non-linear constitutive relation, we have used the dual sliplink model [23] to account for the linear and non-linear rheological behavior of a well-entangled polymer system. The proposed ML method has been tested on a pressure gap driven flow, for a typical viscoelastic condition, and is shown to reproduce the flow properties with reasonable accuracy (i.e., $\lesssim 10\%$ relative error for the shear stress). This accuracy can be improved upon by using a more robust/sophisticated training protocol, e.g., by increasing the number of polymer chains in the microscopic simulator (decreasing the noise due to thermal fluctuations, increasing the training points, and/or actively sampling the constitutive equation space.

In particular, we developed a ML method to learn the non-linear rheological response of the sliplink model under startup and oscillatory shear flows. The learned constitutive relation has well reproduced the rheological responses for deformation rates over two orders of magnitude around the inverse of the longest relaxation time. The learned relation can accurately reproduce the responses for the weakly elastic flows, with $\mathrm{Wi} < 1$ and $\mathrm{El} < 1$, i.e., the linear rheological responses. The simulation results also provide accurate predictions for the rheological response corresponding to the longest relaxation mode, under the transient state, as well as the non-linear behaviour at steady state. The computational cost is significantly reduced, compared to directly using the microscopic simulators, and the ML model also has the benefit of being easy to parallelize, allowing us to leverage the power of modern GPUs.

This study also provides us with a road map for the future development of the proposed simulation scheme. To increase the accuracy of the flow predictions, in particular for the transient regime, the rheological responses of the higher-order modes of relaxation should be reflected in the training data. Furthermore, to protect against inaccurate predictions, we can employ a data-driven approach to generate a suitable trajectory in constitutive equation space (i.e., using a velocity gradient profile customized to the specific flow problem we wish to study). In particular, we could use some known constitutive relation to help identify difficult to learn rheological responses. In any case, the equation-free learning proposed here is enough for predicting the fundamental responses for deformation rates around the inverse of the longest relaxation time.

The use of ML constitutive relations will help us to predict the rheological behavior of any complex fluid, given only knowledge of the molecular-based model. The method allows us to maintain the connection between the microscopic molecular structure and the macroscopic flow properties, at little to no computational costs compared to the conventional MSS approach. The acceleration provided by learning the relation between these two scales will not only help us to refine manufacturing processes, but it will also promote the understanding of the rheological properties of complex fluids.

2.A Implimentation of Simulation

The smoothed particle hydrodynamics simulations for the macroscopic flows are parallelized using the "Framework for Developing Particle Simulators" (FDPS)[91], as used in previous MSS studies by Murashima [92]. The GP regression is performed using the GPyTorch library[89], based on the PyTorch framework[90]. The trained ML model is called within the MSS code by interfacing the C++ code with the PyTorch library (using TorchScript).

2.B Microscopic Polymer System: Dual Sliplink Model

The sliplink model proposed by Doi and Takimoto[23] expresses the relaxation mechanisms of entangled polymer chains. A polymer chain in this model is represented as a set of primitive paths, sliplinks, and two tail segments. The sliplinks, occurring in pairs on different chains, are continuously being created and released. This model has been shown to quantitatively reproduce the rheological properties of entangled polymers[23, 85, 86].

A model chain has two parameters, the number of entanglements at equilibrium $Z_{\rm eq}$ and the maximum stretch ratio $\lambda_{\rm max}$. The units of time $\tau_{\rm e}$ and length a are the Rouse relaxation time and the equilibrium length of a strand, i.e., the bond between two paired/connected sliplinks. This model has three relaxation mechanisms:

- Reptation
- Contour Length Fluctuations (CLF)
- Constraint Release (CR)

The stress $\boldsymbol{\sigma}$ is evaluated as an ensemble average over the bond vectors $\boldsymbol{r}$, with unit stress $\sigma_{\rm e}$, and FENE parameter f, as given in Eq. (2.3).

Next, we consider the linear rheology for a monodisperse system under this model. The linear complex modulii $G'(\omega) \propto \omega^2$ and $G''(\omega) \propto \omega$, obtained from the linear relaxation modulus $G(t)$, give the relaxation time $\tau_{\rm d}$. This is evaluated by fitting the small ω behaviour of $G'(\omega)$ and $G''(\omega)$ to be proportional to ω^2 and ω, respectively, and determining the point of intersection, which is defined to be $\omega^*\tau_{\rm e} = \tau_{\rm e}/\tau_{\rm d}$. The linear viscoelasticity $G(t)$ is computed using the Green-Kubo formula, from the auto-correlations of the stress $\sigma_{\alpha\beta}$

$$\begin{aligned} G(t) =& \frac{V}{5k_{\rm B}T}(\langle\sigma_{xy}(0)\sigma_{xy}(t)\rangle + \langle\sigma_{yz}(0)\sigma_{yz}(t)\rangle + \\ & \langle\sigma_{zx}(0)\sigma_{zx}(t)\rangle) + \frac{V}{30k_{\rm B}T}\Big(\langle N_{xy}(0)N_{xy}(t)\rangle + \\ & \langle N_{yz}(0)N_{yz}(t)\rangle + \langle N_{zx}(0)N_{zx}(t)\rangle\Big), \end{aligned} \tag{2.24}$$

where V is the volume, $k_{\rm B}$ the Boltzmann constant, T the temperature, and $N_{\alpha\beta} = \sigma_{\alpha\alpha} - \sigma_{\beta\beta}$ the normal stress difference. Finally, the relation between the longest relaxation time $\tau_{\rm d}$ and $Z_{\rm eq}$ is obtained from a fit to the linear viscoelasticity as

$$\tau_{\rm d}/\tau_{\rm e} = C_{\tau_{\rm d}} Z_{\rm eq}^{3.45}. \tag{2.25}$$

We obtain $C_{\tau_{\rm d}} = \exp(-2.01 \pm 0.01)$ using a least-squares method.

Table 2.2 Cross model fitting parameters for the number of entanglements $Z_{\rm eq}$.

$Z_{\rm eq}$	$\eta_0^{\rm (C)}/\sigma_{\rm e}\tau_{\rm e}$	$\eta_\infty^{\rm (C)}/\sigma_{\rm e}\tau_{\rm e}$	$\tau^{\rm (C)}/\tau_{\rm e}$	n
5	6.98×10^{0}	2.78×10^{0}	3.61×10^{1}	1.85
10	7.28×10^{1}	8.25×10^{0}	3.99×10^{2}	1.37
20	8.74×10^{2}	2.20×10^{1}	5.11×10^{3}	1.20
40	9.28×10^{3}	5.46×10^{1}	5.48×10^{4}	1.17
80	9.85×10^{4}	1.36×10^{2}	6.10×10^{5}	1.15

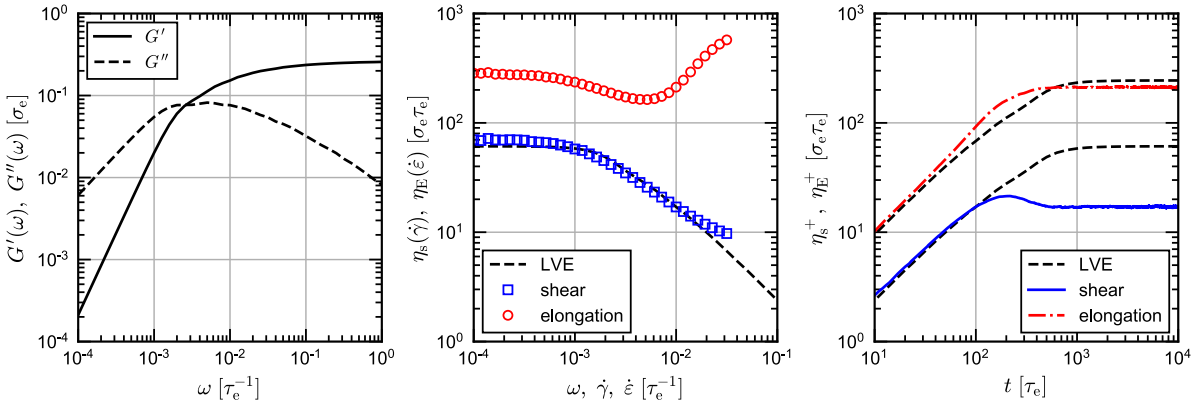

Fig. 2.5 Rheological properties for a mono-disperse system with $Z_{\rm eq}=10$. (left) Linear viscoelasticity, where the solid line is the storage modulus $G'(\omega)$ and the dashed line is the loss modulus $G''(\omega)$. (center) Steady viscosities under shears and planar elongations. Squares and circles show the mean values of the steady shear viscosity $\eta_{\rm s}(\dot\gamma)$ and the planar elongational viscosity $\eta_{\rm E}(\dot\varepsilon)$, respectively. The dashed line indicates the linear viscoelasticity (LVE) results, corresponding to the absolute value of the linear complex viscosity $|\eta^*(\omega)|$. (right) Transient viscosities under steady shear, with $\dot\gamma=1/\tau_{\rm R}$ (solid line), and planar elongation, with $\dot\varepsilon=1/\tau_{\rm R}$ (dotted dashed line) where $\tau_{\rm R}$ is the Rouse relaxation time. The dashed lines are the LVE results ($|\eta^*(\omega)|$ and $4|\eta^*(\omega)|$) using the Trouton rule.

The shear viscosities $\eta_{\rm p}(\dot\gamma)$ for the steady shear flows, with shear rates $\dot\gamma$, are fitted to the Cross model as

$$\eta_{\rm p}(\dot\gamma)=\eta_\infty^{\rm (C)}+\frac{\eta_0^{\rm (C)}-\eta_\infty^{\rm (C)}}{1+(\tau^{\rm (C)}\dot\gamma)^n}. \tag{2.26}$$

The model parameters $(\eta_0^{\rm (C)},\eta_\infty^{\rm (C)},\tau^{\rm (C)},n)$ are shown in Table 2.2, and were obtained from simulations under steady shear for each $Z_{\rm eq}$. Using the zero shear viscosity $\eta_{\rm p}$ given by the Cross model $\eta_0^{\rm (C)}$, the exponential relation of the entanglements is written as

$$\eta_{\rm p}/(\sigma_{\rm e}\tau_{\rm e})=C_{\eta_{\rm p}}Z_{\rm eq}^{3.45}, \tag{2.27}$$

where $C_{\eta_{\rm p}}=\exp(-3.61\pm0.02)$.

We now discuss the rheology of the mono-disperse system with $Z_{\rm eq}=10$ employed in this study. The longest relaxation time $\tau_{\rm d}$ and the zero shear viscosity $\eta_{\rm p}$ are obtained as $\tau_{\rm d}=3.8\times10^{2}\tau_{\rm e}$ and $\eta_{\rm p}=7.6\times10^{1}\sigma_{\rm e}\tau_{\rm e}$, respectively. Figure 2.5 contains the key rheological properties. We show the linear storage and loss moduli, $G'(\omega)$ and $G''(\omega)$ (left panel), as evaluated by Eq. (2.24). As seen from the

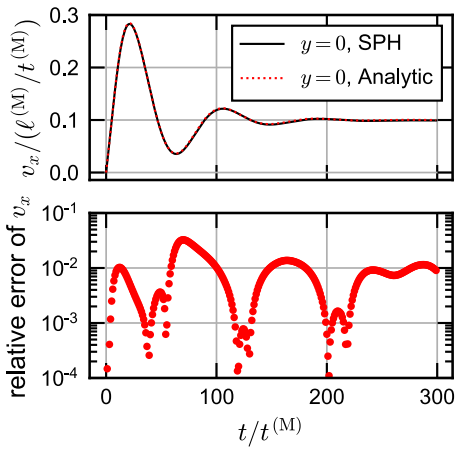

Fig. 2.6 (top) Velocity v_x at the center line ($y = 0$) for the Oldroyd-B fluid flow between two parallel plates. the black line is the results of SPH simulation and the red line shows the analytical solution. (bottom) The red symbols are the absolute relative errors of v_x at $y = 0$ with time.

data, the model contains the slow modes of the entangled polymer chain, from the terminal regime to the plateau regime. The system's non-linear behavior at higher strain rates is evidenced by the shear thinning and the thickening under planar elongations (center panel). Finally, transient viscosities show the strain softening under steady shear, and the strain hardening under steady planar elongation. Thus, the model is clearly capable of replicating the non-linear rheological behavior observed in experimentals, which distinguishes it from the simple dumbbell model used previously to test the ML simulation framework. At the same time, however, these complex non-linear properties pose a challenge when attempting to learn its constitutive relation.

2.C Macroscopic Fluid Solver: WCSPH

We employ a fluid solver within the Lagrangian picture, in order to easily handle the advection of the polymeric systems. For this, we use the smoothed particle hydrodynamics (SPH) method, which discretises the fluid into smoothed particles [31], and in particular, its weakly compressible SPH (WCSPH) variant[93]. The governing equations of i-th particle are written as

$$\frac{\mathrm{d}\boldsymbol{x}^{(i)}}{\mathrm{d}t} = \boldsymbol{v}^{(i)}, \tag{2.28}$$

$$\frac{\mathrm{d}\boldsymbol{v}^{(i)}}{\mathrm{d}t} = \frac{1}{\rho^{(i)}}\boldsymbol{\nabla}\cdot(\boldsymbol{\sigma}_{\mathrm{t}}^{(i)} - P^{(i)}\boldsymbol{I}) + \frac{\boldsymbol{F}}{\rho^{(i)}}, \tag{2.29}$$

$$P^{(i)} = \frac{C_{\mathrm{s}}^2\rho_0}{\gamma}\left[\left(\frac{\rho^{(i)}}{\rho_0}\right)^{\gamma} - 1\right], \tag{2.30}$$

where $\boldsymbol{x}^{(i)}$ is the position of the particle, $\boldsymbol{v}^{(i)}$ the velocity, $\rho^{(i)}$ the density, $\boldsymbol{\sigma}_{\mathrm{t}}$ the total stress (polymer and additional thermal dissipation contributions), $P^{(i)}$ the pressure, and $\boldsymbol{F}$ the external force. In Eq. (2.30), C_{s} is the sound speed, γ a constant that is set to 1, as is appropriate for viscoelastic flows[94], and ρ_0 the reference density.

The macroscopic units of this WCSPH simulation are the particle radius $b(=\ell^{(\mathrm{M})})$, the time $t^{(\mathrm{M})}$, and the stress $\sigma^{(\mathrm{M})}$. We solve these equations in non-dimensionalised form, having as main parameters to characterize the momentum transport the external force $\hat{\boldsymbol{F}}$, and the momentum diffusion constant $\hat{D}$ (fixed to 1), defined as

$$\hat{\boldsymbol{F}} = \frac{\boldsymbol{F}(t^{(\mathrm{M})})^2}{\rho_0 b}, \tag{2.31}$$

$$\hat{D} = \frac{\sigma^{(\mathrm{M})} b^2}{\rho_0 (t^{(\mathrm{M})})^2}. \tag{2.32}$$

as well as the artificial sound speed $\hat{C}_{\mathrm{s}}(= C_{\mathrm{s}}(t^{(\mathrm{M})})^2/b^2)$. We use $\hat{C}_{\mathrm{s}} = 20$ to ensure the density fluctuations are under 1%, and the incompressibility condition is approximately satisfied. The fluid has a constitutive relation determined by the microscopic polymer system, with longest relaxation time $\tau_{\mathrm{d}}/t^{(\mathrm{M})}$, and zero shear viscosity $\eta_{\mathrm{p}}/(\sigma^{(\mathrm{M})} t^{(\mathrm{M})})$. The ratio of the viscosity η_{d} to the total viscosity β is defined as

$$\beta = \frac{\eta_{\mathrm{d}}}{\eta_{\mathrm{p}} + \eta_{\mathrm{d}}}. \tag{2.33}$$

The thickness of the wall is $L_{\mathrm{w}} = 4b$. A no-slip boundary condition is set between the fluid and walls, such that the velocity of the fluid at the surface satisfies the Dirichlet boundary condition, $\boldsymbol{v} = \boldsymbol{0}$, and the stress tensor follows the Neumann boundary condition, i.e., the gradient normal to the surface is zero.

The density ρ at position $\boldsymbol{x}$ is computed as a weighted average, over the neighboring particles located at $\boldsymbol{x}'$, as

$$\rho(\boldsymbol{x}) = \int \mathrm{d}\boldsymbol{x}' m W(|\boldsymbol{x}' - \boldsymbol{x}|, h), \tag{2.34}$$

where $m(=\rho_0/b^3)$ is the mass of a particle and h is the smoothing length. The value of this smoothing length is fixed to twice the diameter of the SPH particle ($h = 2b$). The revised Gaussian kernel [95] is utilized as the SPH kernel W, with cutoff radius $2h$.

$$W(r, h) = \frac{A_2}{(h\sqrt{\pi})^2}\left[e^{-r^2/h^2} - e^{-4}\right], (0 \le r \le 2h). \tag{2.35}$$

The pre-factor $A_2 = 1.10081$ is the normalizing constant for a 2d system. When smoothing a field variable, we adopt the Kernel Gradient Free (KGF) method [96], which satisfies the second-order compatibility of the Taylor series expansion. For the time-integration of the SPH particles, the velocity-Verlet scheme is used. To improve the numerical stability, a particle rearrangement scheme is implemented to shift the particle positions, as detailed in a report by Murashima [94]. The shift vector $\Delta\boldsymbol{x}^{(i)}$ for the i-th particle is defined as

$$\Delta\boldsymbol{x}^{(i)} = \epsilon\delta_0 \int \mathrm{d}\boldsymbol{x}' \frac{\boldsymbol{x}' - \boldsymbol{x}^{(i)}}{|\boldsymbol{x}' - \boldsymbol{x}^{(i)}|} W(|\boldsymbol{x}' - \boldsymbol{x}^{(i)}|, h), \tag{2.36}$$

where ϵ is a constant and $\delta_0(= b)$ is the initial distance between particles at the start of the simulation. To avoid the tensile instability, Ref.[94] recommends a value of ϵ between 0.001 and 0.1, we set $\epsilon = 0.005$. Thus, the (shifted) positions $\boldsymbol{x}^{(i)}$ and velocities $\boldsymbol{v}^{(i)}$ are defined as

$$\boldsymbol{x}^{(i)} = \boldsymbol{x}^{(i)}_{\mathrm{old}} + \Delta\boldsymbol{x}^{(i)}, \tag{2.37}$$

$$\boldsymbol{v}^{(i)} = \boldsymbol{v}^{(i)}_{\mathrm{old}} + \Delta\boldsymbol{x}^{(i)} \cdot \nabla\boldsymbol{v}^{(i)}_{\mathrm{old}}, \tag{2.38}$$

where $\boldsymbol{x}_{\rm old}^{(i)}$ and $\boldsymbol{v}_{\rm old}^{(i)}$ are the corresponding variables before shifting.

To test our numerical scheme we consider a pressure gap driven flow between parallel plates for an Oldroyd-B model fluid. Figure 2.6 shows the velocity along the center line, using the same parameters as in Table 2.1. The predicted SPH velocity is in excellent agreement with the analytical solution. For this typical viscoelastic problem, the relative errors are under 3%. For the types of flows, and analysis, considered in this work, this error is small enough that it can be ignored.

2.D Analytical Solution of the Case of an Oldtoyd-B Fluid

In the $x-y$ plane, two parallel plates face the y direction at $x=0$ and $x=L$, where L is the distance of the plates. Between the plates, an Oldroyd-B fluid flows in the x direction. We assume the laminar flows, the fluid velocity v is a function of time t and position y. An Oldroyd-B fluid has the parameters: the kinetic viscosity ν, the relaxation time of stress λ_1, and the retardation time of solute λ_2. The momentum equation is simplified as

$$\left(1+\lambda_1\frac{\partial}{\partial t}\right)\frac{\partial v}{\partial t}=\nu\left(1+\lambda_2\frac{\partial}{\partial t}\right)\frac{\partial^2 v}{\partial y^2}+F. \tag{2.39}$$

This equation follows the boundary and initial conditions:

$$v(0,y)=0,\ \left.\frac{\partial v(t,y)}{\partial t}\right|_{t=0}=F,\ v(t,0)=0,\ v(t,L)=0. \tag{2.40}$$

Let us solve the equation as follows. First, the solution of steady state $v^{(\rm s)}$ is to be obtained as

$$v^{(\rm s)}=\frac{FL^2}{2\nu}\left\{-\left(\frac{y}{L}\right)^2+\frac{y}{L}\right\}, \tag{2.41}$$

The variable $V=v-v^{(\rm s)}$ follows the equation and the conditions

$$\left(1+\lambda_1\frac{\partial}{\partial t}\right)\frac{\partial V}{\partial t}=\left(1+\lambda_2\frac{\partial}{\partial t}\right)\nu\frac{\partial^2 V}{\partial y^2} \tag{2.42}$$

$$V(0,y)=-v^{(\rm s)},\ \left.\frac{\partial V(t,y)}{\partial t}\right|_{t=0}=F,\ V(t,0)=0,\ V(t,L)=0. \tag{2.43}$$

We expand V on the sine basis as

$$V(t,y)=\sum_{n=1}^{\infty}A_n(t)\sin\left(n\pi\frac{y}{L}\right), \tag{2.44}$$

where $A_n(t)$ is the Fourier coefficient. From Eqs. (2.42) and (2.44), we obtained the ordinal differential equation of $A_n(t)$:

$$\left(1+\lambda_1\frac{\mathrm{d}}{\mathrm{d}t}\right)\frac{\mathrm{d}A_n}{\mathrm{d}t}=-\nu\left(\frac{n\pi}{L}\right)^2\left(1+\lambda_2\frac{\mathrm{d}}{\mathrm{d}t}\right)A_n \tag{2.45}$$

We substitute $A_n(t)=e^{\alpha t}$,

$$\lambda_1\alpha^2+\left\{1+\lambda_2\nu\left(\frac{n\pi}{L}\right)^2\right\}\alpha+\nu\left(\frac{n\pi}{L}\right)^2=0, \tag{2.46}$$

$$\alpha=\frac{-(1+\lambda_2\nu k_n^2)}{2\lambda_1}\pm\frac{1}{2\lambda_1}\sqrt{(1+\lambda_2\nu k_n^2)^2-4\lambda_1\nu k_n^2} \tag{2.47}$$

where $k_n = n\pi/L$.

For the case of $(1+\lambda_2\nu k_n^2)^2 < 4\lambda_1\nu k_n^2$, the solution is written as

$$V(t,y) = \sum_{n=1}^{\infty} \exp\left(-\frac{1+\lambda_2\nu k_n^2}{2\lambda_1}t\right)[C_n\cos(\omega_n t) + S_n\sin(\omega_n t)]\sin\left(n\pi\frac{y}{L}\right), \tag{2.48}$$

where C_n and S_n are the constants, and $\omega_n = 1/(2\lambda_1)\sqrt{4\lambda_1\nu k_n^2 - (1+\lambda_2\nu k_n^2)^2}$. We evaluate C_n and S_n with the initial conditions of Eq. (2.43), the results are obtained as

$$C_n = -\frac{FL^2}{\nu}\frac{2(1-(-1)^n)}{(n\pi)^3} \tag{2.49}$$

$$S_n = \frac{1}{\omega_n}\left(2F\frac{1-(-1)^n}{n\pi} + \frac{1+\lambda_2\nu k_n^2}{2\lambda_1}C_n\right) \tag{2.50}$$

For $(1+\lambda_2\nu k_n^2)^2 > 4\lambda_1\nu k_n^2$, we can derive the same formula of coefficients C_n and S_n corresponding $\cos \to \cosh$ and $\sin \to \sinh$, respectively. Also for $(1+\lambda_2\nu k_n^2)^2 = 4\lambda_1\nu k_n^2$, C_n is the same to $\cos \to 1$, but S_n for $\sin \to t$ get the multiplied form of Eq. (2.50) and ω_n.

Summarizing the results, using the re-defined ω_n as

$$\omega_n = \frac{1+\lambda_2\nu k_n^2}{2\lambda_1}\sqrt{\left|(1+\lambda_2\nu k_n^2)^2 - 4\nu\lambda_1 k_n^2\right|}; \quad k_n = (n\pi/L)^2, \tag{2.51}$$

the solution is written as

$$\begin{aligned} v(t,y) =& \frac{FL^2}{2\nu}\left\{-\left(\frac{y}{L}\right)^2 + \left(\frac{y}{L}\right)\right\} \\ &+ \sum_{n=1}^{\infty}\sin\left(n\pi\frac{y}{L}\right)\exp\left(-\frac{1+\lambda_2\nu k_n^2}{2\lambda_1}t\right) \\ &\times \begin{cases} C_n\cosh(\omega_n t) + S_n\sinh(\omega_n t) & \text{for } (1+\lambda_2\nu k_n^2)^2 > 4\lambda_1\nu k_n^2 \\ C_n + S_n\omega_n t & \text{for } (1+\lambda_2\nu k_n^2)^2 = 4\lambda_1\nu k_n^2 \\ C_n\cos(\omega_n t) + S_n\sin(\omega_n t) & \text{for } (1+\lambda_2\nu k_n^2)^2 < 4\lambda_1\nu k_n^2 \end{cases}, \end{aligned} \tag{2.52}$$

where C_n and S_n are defined as Eqs. (2.49) and (2.50), respectively.

Chapter 3

MLMSS for Multi-Mode-Deformation Flows in 2D Geometry

3.1 Introduction

Following the previous Chapter, in this Chapter 3, we extend the MLMSS method developed for the general two-dimensional flows composed of time-dependent deformation modes. For the efficient use of a regression model, we consider the rotational symmetry of the stress rate required by the objectivity principle. We assess the extended regression model by using pressure-gap driven flows in a contraction expansion channel employed in the typical benchmark problem of viscoelastic fluid flows

We take the considerable computational cost for MSS, even using the corpse-grained, in return for understanding of the flow based on the molecular rheology. The recent development of computational environment and technics, particularly the machine-learning (ML) based method, have played on the acceleration of MSS. We proposed the one for the general viscoelastic fluids, the use of the function form of the constitutive relation: $\dot{\boldsymbol{\sigma}} = \dot{\boldsymbol{\sigma}}(\boldsymbol{\sigma}, \boldsymbol{\kappa})$ where $\dot{\boldsymbol{\sigma}}$ the time derivative of the stress, $\boldsymbol{\sigma}$ the stress, $\boldsymbol{\kappa}$ the velocity gradient.

The previous studies on the ML-based MSS method have reported the efficiency of the computation maintaining the accuracy for the linear[55] and nonlinear[61] for the specific cases, single mode of deformation exists in the flows, as shears or elongations. The flows in industrial processing have each mode and the multi modes of deformation, and the fundamental research has challenged the history-dependent flows. The complex fluid experience shear and elongation deformations in these geometries even at a steady state. Our proposed ML scheme has not illustrated the assessments for the multi-deformation mode flows.

The contraction and/or expansion channel is the benchmarking problem for the mix of shear and elongation deformation modes. For predicting the general two-dimensional flows, we should provide the training data from the deformation histories with the multi-deformation modes; shear, elongation, and combinations of the two modes. The amount of training data used in learning the constitutive relations is expected to be larger than the order of $\mathcal{O}(10^3)$ when predicting the one deformation mode flows, e.g., pressure-gap driven flow between two parallel plates. The increased data and the high dimensionality in the learning can prevent the efficiency of the computational costs.

To answer the efficiency concern for the ML-based simulation scheme, we assess the application to the contraction-expansion channel with the well-entangled polymer model. Apparent deformation histories in a fluid element passing the contract slit strictly test the predictions of the ML constitutive relations

under shear and planar elongations. This chapter is organized as follows. In Section 3.2, we present the MSS framework using the machine-learned constitutive relation. In Section 3.3, we describe the ML simulation results compared to the full MSS. Finally, Section 3.4 summarizes this chapter.

3.2 Method

We extend the proposed ML-based simulation approach to handle the 2D flow simulation. The 2D flow simulations are implemented by the Lagrangian fluid solver, which handles the mass and momentum transports on the incompressible fluid. For solving the momentum transports, the stress field σ contributed by the constituent polymers is needed and is determined or time-developed by the strain field. The relation between stress and strain cannot be explicitly given for complex fluids, but it can be learned by the machine-learning technique.

The constitutive relations to be learned should follow the physical principle of material objectivity. The principle imposes the convection and the rotational invariants to the constitutive relations, which are satisfied in the conventional equations by the material derivatives of stress. We give the way that the ML constitutive relations do not break the symmetry for the rotation of stress rate.

Within the fluid solver on the Lagrangian specification, the migrations of fluid elements handle convection, and the angle changes of the material frames for each element consider rotation, independent of the constitutive relation. On a material frame, the formula of constitutive relation by using the (total) polymer stress $\boldsymbol{\sigma}$ is assumed to be

$$\dot{\boldsymbol{\sigma}} = \dot{\boldsymbol{\sigma}}(\boldsymbol{\sigma}, \boldsymbol{D}), \tag{3.1}$$

where $\boldsymbol{D}(\equiv (\boldsymbol{\kappa} + {}^t\boldsymbol{\kappa})/2)$ is the strain rate tensor. In contrast to Eq.(2.1) used in the previous chapter, the external field is $\boldsymbol{D}$, not $\boldsymbol{\kappa}$. The spin tensor $\boldsymbol{W}(\equiv (\boldsymbol{\kappa} - {}^t\boldsymbol{\kappa})/2)$ does not contribute to the stress, and is used for the rotation of the angle of the fluid element. In the fluid flow simulations, the ML constitutive relation of Eq. (3.1) on the material frame ensures the invariances of the material objectivity.

As summary, the governing equations in xy plane are Eq. (3.1) and the following Eqs. (3.2)–(3.6) as

$$\frac{\mathrm{d}\boldsymbol{r}}{\mathrm{d}t} = \boldsymbol{v}, \tag{3.2}$$

$$\frac{\mathrm{d}\boldsymbol{v}}{\mathrm{d}t} = \frac{1}{\rho}\boldsymbol{\nabla}\cdot(\boldsymbol{\sigma}_\mathrm{t} - P\boldsymbol{I}) + \frac{\boldsymbol{F}}{\rho}, \tag{3.3}$$

$$\frac{\mathrm{d}\theta}{\mathrm{d}t} = \omega, \tag{3.4}$$

$$\boldsymbol{\sigma}_\mathrm{t} = \boldsymbol{\sigma} + \boldsymbol{\sigma}_\mathrm{d}, \tag{3.5}$$

$$\boldsymbol{\sigma}_\mathrm{d} = \eta_\mathrm{d}(\boldsymbol{\kappa} + {}^t\boldsymbol{\kappa}), \tag{3.6}$$

where $\boldsymbol{r}$, $\boldsymbol{v}$, and θ are the position, the velocity, and the rotation angle (about z-axis) of a fluid element. ρ is the constant density, $\boldsymbol{\sigma}_\mathrm{t}$ the total stress, P the pressure, $\boldsymbol{I}$ the unit tensor, $\boldsymbol{F}$ is the external force, $\omega(\equiv -W_{xy} = W_{yx})$ the rotational rate. $\boldsymbol{\sigma}$ is the polymer stress, and $\boldsymbol{\sigma}_\mathrm{d}$ is the additional dissipative contributions; η_d is the viscosity due to the thermal fluctuation at the coarse-grained scale from the polymer model. $\boldsymbol{\kappa}(\equiv \kappa_{\alpha\beta} \equiv \nabla_\beta v_\alpha$ where $\alpha, \beta \in [x, y])$ is the velocity gradient.

Figure 3.1 summarizes the scheme proposed for the two-dimensional flow simulations. We give detailed implementations of the learning and flow simulation parts in the following sections. Section 3.2.1 shows how to learn the constitutive relation of Eq. (3.1) using the multi-deformation mode flows. Section 3.2.2 presents the flow solver and the configuration for assessing this method.

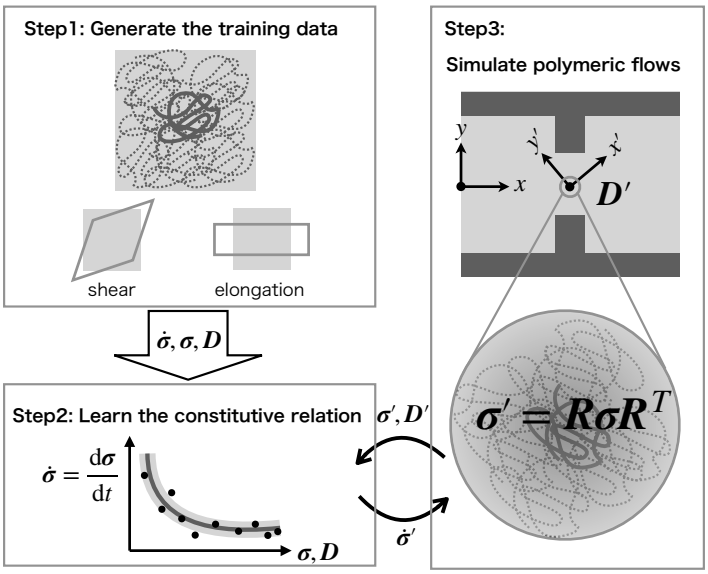

Fig. 3.1 Schematic illustration of the proposed protocol. It summarizes the procedure for simulating a MLMSS of entangled polymer systems in the following three steps: (i) generate the training data from (pure) shears and elongations, (ii) learn the constitutive relation based on the data with the trajectories of the stress $\boldsymbol{\sigma}$ and the strain rate $\boldsymbol{D}$, (iii) simulate the polymeric flows discretized by the Lagrangian elements capable to be rotated, and the rotation matrix $\boldsymbol{R}$ transforms $\boldsymbol{\sigma}$ and $\boldsymbol{D}$ on the $x-y$ coordinate of the system to that of the fluid element ($\boldsymbol{\sigma}'$ and $\boldsymbol{D}'$ on $x'-y'$ plane).

3.2.1 Learning the Cosntitutive Relation

We employ a well-entangled polymer model extended from tube theory, the dual sliplink model[23] by Doi and Takimoto because this model reproduces the experimental results of rheological properties in an entangled state for the linear and nonlinear regions[23, 85, 86]. The target polymer system represents the monodispersed polystyrene of about 100 kDa, where the rheological predictions are reported previously (e.g., Ref. [61]). The polymer configuration parameters, the number of entanglements at equilibrium $Z_{\mathrm{eq}} = 10$ and the maximum stretch ratio $\lambda_{\max} = 4.4$, are dependent on the molecular weight and the polymer rigidity by the chemical species, respectively. τ_{e} and a are the units of time and length characterized by a strand (the segments between connected two sliplinks); the Rouse relaxation time and the equilibrium length. σ_{e} is the unit value of stress connected to the plateau modulus. We redefine the microscopic scale units with the superscript of (m) as $t^{(\mathrm{m})} = \tau_{\mathrm{e}}$, $\ell^{(\mathrm{m})} = a$, and $\sigma^{(\mathrm{m})} = \sigma_{\mathrm{e}}$.

The conformation of sliplinks in the polymer system provides the statistically evaluated stress as follows:

$$\boldsymbol{\sigma} = \sigma_{\mathrm{e}} \Big\langle \frac{\boldsymbol{Q}\boldsymbol{Q}}{a|\boldsymbol{Q}|} \Big\rangle, \tag{3.7}$$

where $\boldsymbol{Q}$ is the displacement vector of the adjacent sliplinks; $\boldsymbol{Q}^i \equiv \boldsymbol{q}^{i+1} - \boldsymbol{q}^i$ $(i = 1, 2, \ldots, Z-1)$ for a linear chain with Z sliplinks at the positions $\boldsymbol{q}^i$ $(i = 1, 2, \ldots, Z)$. We evaluate the linear relaxation modulus $G(t)$ by the auto-correlations of the stress components, the terminal mode of $G(t)$ is characterized by the longest relaxation time and the zero shear viscosity: $(\tau_{\mathrm{d}}, \eta_{\mathrm{p}}) = (3.8 \times 10^2 \tau_{\mathrm{e}}, 7.6 \times 10^1 \sigma_{\mathrm{e}} \tau_{\mathrm{e}})$[61]. Under a deformation, the polymer conformation is sequentially contributed by the (local) strain rate $\boldsymbol{D}$ with

time, and the stress with Eq. (3.7) reflects the history $\boldsymbol{D}(t)$. We note that the assumed constitutive relation picks the first-order derivative of total stress $\dot{\boldsymbol{\sigma}}$ as the time-dependent states reduced from the conformation.

For generating the training data, we apply the $N_{\rm g}$ velocity gradient histories, $\boldsymbol{\kappa}^1(t), \boldsymbol{\kappa}^2(t), \ldots, \boldsymbol{\kappa}^{N_{\rm g}}(t)$, to the equilibrated systems, independently prepared for each history with simulating for about twenty times the longest relaxation time $20\tau_{\rm d}$. The velocity gradient is decomposed to the symmetric and anti-symmetric components as $\boldsymbol{\kappa} \equiv \boldsymbol{D} + \boldsymbol{W}$. For learning the constitutive relation of Eq. (3.1) on a material frame, the system tracks the system angle θ by the rotational rate ω as in Eq. (3.4). The record obtained from the simulations is the set of ($\boldsymbol{\sigma}'$ and $\boldsymbol{D}'$), and the primed variables are on the material frame ($x'-y'$); where the coordinate transformation by using the rotation tensor $\boldsymbol{R}(\theta)$ stand, e.g., $\boldsymbol{\sigma}' \equiv \boldsymbol{R}(\theta)\boldsymbol{\sigma}^t\boldsymbol{R}(\theta)$. This study constrains the strain rate as ${\rm Tr}\boldsymbol{D} = {\rm Tr}\boldsymbol{D}' = 0$ so as to be incompressible, thus the two components, $\dot{\gamma}(\equiv D_{xy} = D_{yx})$ and $\dot{\varepsilon}(\equiv D_{xx} = -D_{yy})$ (averaged with the two components of D due to weakly incompressible in this simulation), are collected for the training inputs $(\sigma'_{xx}, \sigma'_{xy}, \sigma'_{yy}, \dot{\gamma}', \dot{\varepsilon}')$.

The learning of Eq. (3.1) is implemented by the GP regression scheme [88]. The time derivative of stress, assumed to be a function of the stress and strain rate, is given by the following GP prior

$$\dot{\boldsymbol{\sigma}} = \dot{\boldsymbol{\sigma}}(\boldsymbol{\sigma}, \boldsymbol{D}) \sim N(\boldsymbol{\mu}, \boldsymbol{K}), \tag{3.8}$$

where $\boldsymbol{\mu}$ and $\boldsymbol{K}$ are the mean and covariance. The input data are correlated within the covariance kernel function $k(\boldsymbol{x}^{\rm a}, \boldsymbol{x}^{\rm b})$.

$$\begin{aligned} k(\boldsymbol{x}^{\rm a}, \boldsymbol{x}^{\rm b}) =& \Theta_\eta k_{\rm M}(\dot{\gamma}^{\rm a}, \dot{\gamma}^{\rm b}; \Theta_{\dot{\gamma}}) \times k_{\rm M}(\dot{\varepsilon}^{\rm a}, \dot{\varepsilon}^{\rm b}; \Theta_{\dot{\varepsilon}}) \\ & \times k_{\rm M}([\sigma^{\rm a}_{xx}, \sigma^{\rm a}_{xy}, \sigma^{\rm a}_{yy}], [\sigma^{\rm b}_{xx}, \sigma^{\rm b}_{xy}, \sigma^{\rm b}_{yy}]; \Theta_{\boldsymbol{\sigma}}), \end{aligned} \tag{3.9}$$

where Θ_η is the covariance scale parameter, $\Theta_{\dot{\gamma}}$. $k_{\rm M}$ is the Matern kernel defined as

$$\begin{aligned} k_{\rm M}(\boldsymbol{x}^{\rm a}, \boldsymbol{x}^{\rm b}; \boldsymbol{\Theta}_\ell) = \left(1 + \sqrt{5}d + \frac{5}{3}d^2\right)\exp\left(-\sqrt{5}d\right), \\ \text{where } d = {}^t(\boldsymbol{x}^{\rm a} - \boldsymbol{x}^{\rm b}){\rm diag}(\boldsymbol{\Theta}_\ell)^{-2}(\boldsymbol{x}^{\rm a} - \boldsymbol{x}^{\rm b}) \end{aligned} \tag{3.10}$$

3.2.2 Predicting the Polymeric Flow

As in the previous MSS studies [33, 61, 79, 85, 87], we employ the Smoothed Particle Hydrodynamics (SPH) for the Lagrangian fluid solver [31, 93]. At $t = 0$, the aligned smoothed particles in a grid with a space equal to the particle diameter b are put on the macroscopic system. The smoothing kernel function $W(r, h)$, where r is the distance and h is the smoothing length, here is the revised Gaussian kernel with $h = 2b$, and the radius for convolution reaches $2h$. The density ρ at the position $\boldsymbol{r}$ is convoluted over the neighbor particles at $\boldsymbol{r}^{\rm n}$ with the kernel function as

$$\rho(\boldsymbol{r}) = \int {\rm d}\boldsymbol{r}^{\rm n} m W(|\boldsymbol{r}^{\rm n} - \boldsymbol{r}|, h), \tag{3.11}$$

where m is the particle mass. For incompressibility, we give the state equation to weakly constrain $\rho(\boldsymbol{r})$ as

$$P = \frac{C_{\rm s}^2\rho_0}{C_\gamma}\left[\left(\frac{\rho}{\rho_0}\right)^{C_\gamma} - 1\right], \tag{3.12}$$

where $C_{\rm s}$ is the sound speed parameter, $\rho_0 (= m/b^3)$ the reference density, C_γ the constant set to 1. For the Taylor series compatibility of time and space, the SPH implementation adopts the velocity Verlet

Parameter	Definition	Value
Z_{eq}	# of entanglements at equi.	10
$\lambda_{\max}$	Maximum stretch ratio	4.4
(L_x, L_y)	System size	$(80b, 56b)$
(w_x, w_y)	Size of contraction part	$(28b, 14b)$
F_x	External force	$0.025\sigma^{(\mathrm{M})}/\ell^{(\mathrm{M})}$
τ_{d}	Relaxation time	$14t^{(\mathrm{M})}$
η_{t}	Total viscosity	$14t^{(\mathrm{M})}\sigma^{(\mathrm{M})}$
β	Viscosity ratio	0.1
Δt	Time step	$0.001t^{(\mathrm{M})}$
C_{s}	Sound speed	$20\ell^{(\mathrm{M})}/t^{(\mathrm{M})}$

Table 3.1 Simulation parameters for the microscopic polymer system and the macroscopic fluid flow.

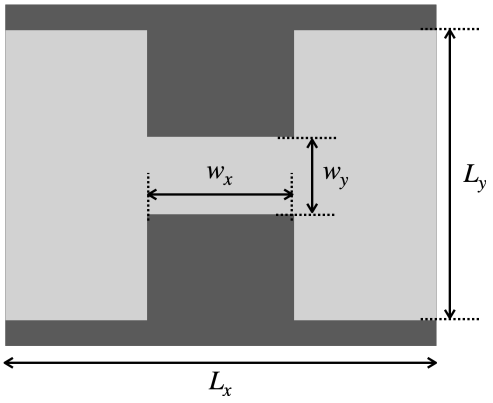

Fig. 3.2 Geometry of the contraction expansion channel.

scheme the kernel gradient free method, and for the numerical stability, the particle shifting method is employed, utilized as in our previous study [61].

Given the velocity gradient $\boldsymbol{\kappa}$ on laboratory frame, the stress tensor $\boldsymbol{\sigma}$ is updated by the learned constitutive relation and the rotation as follows:

$$\boldsymbol{\sigma}'(t+\Delta t) = \boldsymbol{\sigma}'(t) + \dot{\boldsymbol{\sigma}}'(t)(\boldsymbol{\sigma}'(t), \boldsymbol{D}'(t))\Delta t, \tag{3.13}$$

$$\theta(t+\Delta t) = \theta(t) + \omega\Delta t, \tag{3.14}$$

where Δt is the time-step.

The macroscopic units are the variables denoted with (M) as the time $t^{(\mathrm{M})}$, the length $\ell^{(\mathrm{M})}(= b)$, and the stress $\sigma^{(\mathrm{M})}(= \rho_0 b^2/(t^{(\mathrm{M})})^2)$. For bridging the macro- and micro-scales, the velocity gradient $\boldsymbol{\kappa}$ and the stress $\boldsymbol{\sigma}$ are exchanged between the scales, where the time- and stress- ratios of the units, $t^{(\mathrm{M})}/t^{(\mathrm{m})}$ and $\sigma^{(\mathrm{M})}/\sigma^{(\mathrm{m})}$, are used for the conversions. The ratios are determined by the macroscopic parameters of the polymer viscosity and the relaxation time, $\eta_{\mathrm{p}}/t^{(\mathrm{M})}\sigma^{(\mathrm{M})}$ and $\tau_{\mathrm{d}}/t^{(\mathrm{M})}$, and by the microscopic characters, $\eta_{\mathrm{p}}/t^{(\mathrm{m})}\sigma^{(\mathrm{m})}$ and $\tau_{\mathrm{d}}/t^{(\mathrm{m})}$.

Figure 3.2 shows the macroscopic system for assessing the proposed method as the 4:1:4 contraction-expansion channel, where the shears and planar elongations occur. The periodic cell size of x-direction is L_x, the channel height of the expansion part is L_y, and the rectangle size of the contraction part is

(w_x, w_y). At $t = 0$, the initial system is in a quiescent state. The microscopic polymer systems are thermally equilibrated, and then $t > 0$, the fluid in the system is driven by the external body force $\boldsymbol{F} = (F_x, 0)$ mimicking the (static) pressure gap. The viscoelasticity of the fluid is characterized by the total viscosity $\eta_{\rm t} (\equiv \eta_{\rm p} + \eta_{\rm d})$ and the viscosity ratio $\beta \equiv \eta_{\rm d}/\eta_{\rm t}$. To summarize, Table. 3.1 comprises the list of the parameters for the microscopic- and macroscopic- systems.

3.3 Results and Discussion

We give the result of the learning of the constitutive relation and the validation of the flows driven by pressure gap in two geometries: between parallel plates and in a contraction expansion channel.

3.3.1 Learning the Constitutive Relation under Shears and Elongations

We generated the training data by applying the shears and elongations to the microscopic polymer system. We considered the two deformation types of pure shears and elongations with the strain rates $\dot{\gamma}(t)$ and $\dot{\varepsilon}(t)$, here set the two degrees of freedom independently ($\dot{\gamma}(t)$ or $\dot{\varepsilon}(t)$ is zero). The simple and oscillate deformation histories given as $\dot{\gamma}(t) = \dot{\gamma}_0 H(t)$, $\dot{\varepsilon}(t) = \dot{\varepsilon}_0 H(t)$, $\dot{\gamma}(t) = \gamma_{\max}\omega\cos(\omega t)$, and $\dot{\varepsilon}(t) = \varepsilon_{\max}\omega\cos(\omega t)$, respectively. $H(t)$ is the Heaviside step function, $\dot{\gamma}_0$ and $\dot{\varepsilon}_0$ are the constant strain rate, $\gamma_{\max}$ and $\dot{\varepsilon}_0$ are the maximum strains, ω is the angular frequency. The value of ω was fixed at the inverse of the longest relaxation time: $1/\tau_{\rm d}$. We consider $N_{\dot{\gamma}} = 12$ different shear strain (rate) magnitudes $\dot{\gamma}_0^1, \ldots, \dot{\gamma}_0^{N_{\dot{\gamma}}}$ and $\gamma_{\max}^1, \ldots, \gamma_{\max}^{N_{\dot{\gamma}}}$, evenly spaced on a logarithmic scale within the range $\dot{\gamma}_0, \gamma_{\max}\omega \in [10^{-1}/\tau_{\rm d}, 10^{1}/\tau_{\rm d}]$. These numbers for elongation as for $N_{\dot{\varepsilon}} = 12$ is the same in elongational strain (rate) magnitudes $\dot{\varepsilon}_0$ and $\dot{\varepsilon}_0$. For positive/negative strain rates, for both startup and oscillate flows, each were generated by a different velocity gradient history. The microscopic systems in an equilibrated state at $t = 0$ have been simulated up to $t = 10\tau_{\rm d}$. The smoothed procedure was processed as proposed in the previous chapter for each trajectory generated by the shears and elongations. We have randomly chosen $N_{\rm train} \sim 3 \times 10^3$ data points to serve as the training data. The learning cost was almost the same but slightly more than the shear case because of the one additional variable upon the two strain rates for the regression model.

3.3.2 Validation with Laminar Flows between Parallel Plates

We validated the learned regression model with the analysis of the pressure-gap driven flows described in the previous chapter, and the flow condition is in a typical elastic ($\mathsf{El} = 1$) to use the geometric parameters as in Table 2.1.

The reference results are obtained by full MSS simulations whose microscopic simulator is composed of $N_{\rm p} = 10^4$ polymer chains in a fluid element. Our validation results are summarized in Fig. 3.3, which shows the flow and stress predictions obtained using (a) the learned constitutive relation and (b) the full MSS, as well as (c) the absolute error between the two. In particular, we show (I) the velocity along the channel direction v_x and (II) the σ_{xy}, (III) σ_{xx}, and (IV) σ_{yy} components of the stress. In the bottom panels (c), the dotted red lines give the time series for the maximum absolute error, as a function of the height y, the solid blue lines give the corresponding averaged absolute errors. For a more detailed comparison, Fig. 3.4 shows (left) the time evolution of the velocity v_x along the center line $y = 0$, and (right) the steady-state velocity profile v_x as a function of height along the channel.

The results show the agreement of the predictions with the learned constitutive relation to the full MSS

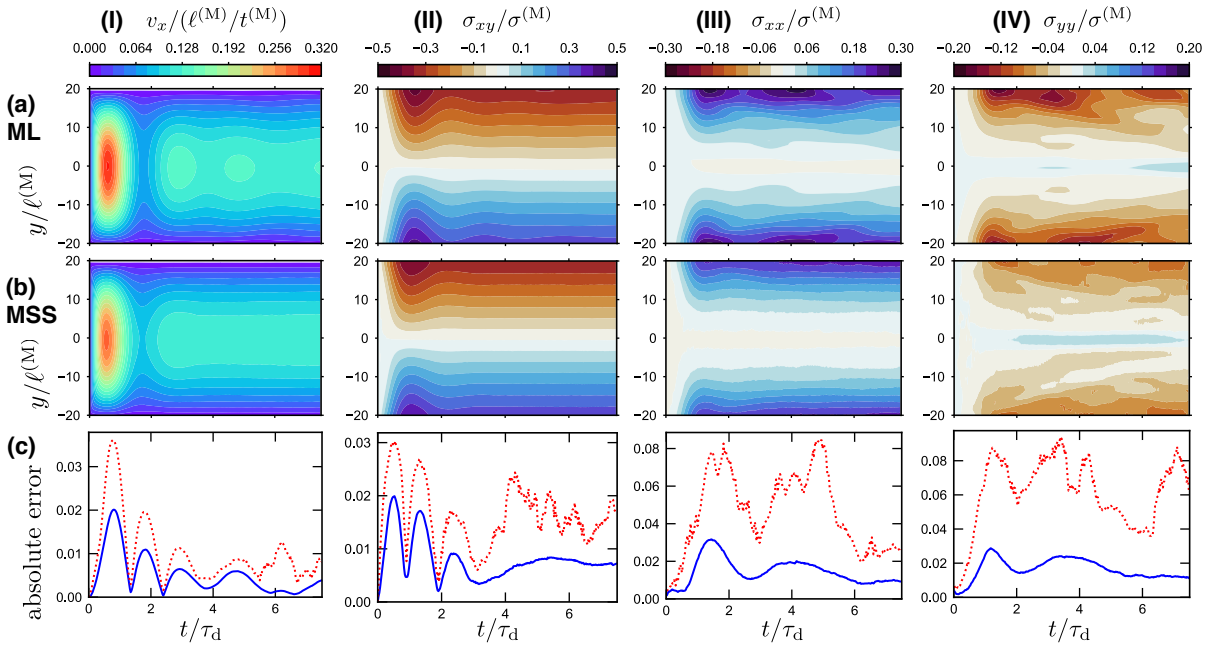

Fig. 3.3 Predictions for the pressure gap driven flow were obtained using (a) the machine-learned constitutive relation, trained on microscopic systems under steady/oscillatory shear flows, and (b) the full MSS, using embedded microscopic simulators (10^4 polymer chains per Lagrangian particle), together with (c) The absolute error between the two simulation results. In the bottom panels (c), the dotted red lines show the maximum absolute error, the solid blue lines the average error values. From left to right, the columns correspond to (I) the velocity along the flow direction v_x, and (II) the σ_{xy}, (III) σ_{xx}, and (IV) σ_{yy} components of the stress.

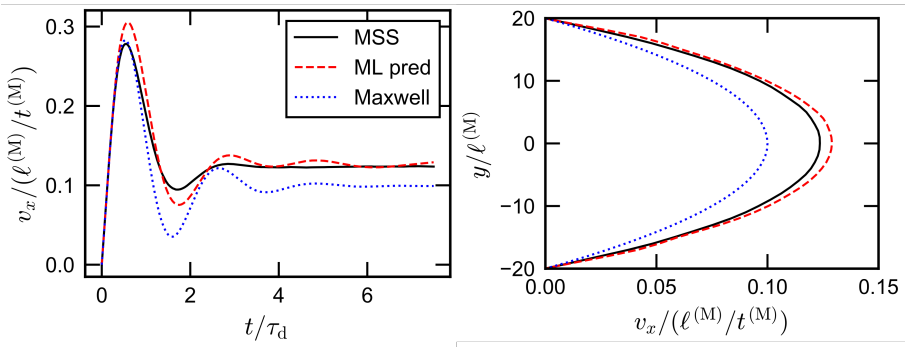

Fig. 3.4 (left) The time series of the velocity v_x along the center line $y = 0$. (right) The steady state velocity v_x as a function of height. The graphs on the left show the elastic case with $\mathrm{El} = 1.0, \mathrm{Wi}^{(\mathrm{a})} = 0.13$ using the parameters shown in Table 2.1. Solid black lines and dashed red lines are the simulation results using the microscopic simulators of the sliplink model and the machine-learned constitutive relation, respectively. Blue dotted lines are the results of the upper convected Maxwell model having the same value of the zero shear viscosity and the longest relaxation time of the sliplink system.

results. Overall, the MLMSS results explain the velocity profiles of the transient and steady states. In particular, the accurate predictions for $\sigma_{\rm yy}$ should be focused against to the results of the previous chapter shown in Fig. 2.3. However, contrary to the reasonable matches in the steady state, the transient velocity shows an accuracy decrease, particularly at the over- and under-shoot behaviors. In this simulation, a fluid element rotates by the rotational rate of deformation, and the mixed modes of shear and elongation, being absent in the training data, can be applied to the microscopic system. One possible reason for decreased accuracy is the inexperienced external fields in training, or simply the increased dimension number of the regression model.

3.3.3 Application to a Contraction Expansion Channel Flow

We applied the learned constitutive relation to the contraction expansion channel where fluid elements experience the time-dependent deformation modes, not as the validation in the previous section.

The reference results of a full MSS calculation were obtained by using the microscopic systems with 10^4 polymer chains. By the full MSS simulation, we calculate the apparent values of the Weissenberg and Reynolds numbers for the flows in the contraction expansion channel defined as

$$\mathsf{Wi}^{(\mathrm{a})} = \frac{\langle v_x \rangle_{\rm c} \tau_{\rm d}}{w_y}, \tag{3.15}$$

$$\mathsf{Re}^{(\mathrm{a})} = \frac{\rho \langle v_x \rangle_{\rm c} w_y}{\eta_{\rm t}}, \tag{3.16}$$

where $\langle v_x \rangle_{\rm c}$ is the average velocity v_x over the narrow slit region, w_y the slit width, ρ the density. The elastic number is defined as

$$\mathsf{El} = \frac{\mathsf{Wi}^{(\mathrm{a})}}{\mathsf{Re}^{(\mathrm{a})}}. \tag{3.17}$$

The values for the parameters given in the simulation results and Table 3.1 are $\mathsf{Wi}^{(\mathrm{a})} \sim 0.1$ and $\mathsf{Re}^{(\mathrm{a})} \sim 0.1$, and $\mathsf{El} = 1$.

Figures 3.5 and 3.6 compare the ML predictions against the full-MSS result using 10^4 chains per fluid particle. In Fig. 3.5, the upper and lower panels show the velocity streamlines and the profiles of principal stress difference (PSD) as PSD $\equiv [4\sigma_{xy}^2 + (\sigma_{xx} - \sigma_{yy})^2]^{1/2}$. The ML- and full-MSS results show qualitative agreement with each other. For further detail, Fig. 3.6 shows the stress profiles along the horizontal center line.

In Fig. 3.6, the profiles of a steady flow are successfully tracked through the startup from the quiescent state using the ML constitutive relation even in the typical elastic conditions. In Fig. 3.6(aII), the streamlines at the corners are fluctuated; this is due to the statistical noise due to the finite size of the system even using 10^4 chains per fluid element. Vortexes should be observed in an accurate simulation with enlarged as an increase of elasticity. We expect that the ML predictions increase in accuracy for smaller $\mathsf{Wi}^{(\mathrm{a})}$ and El than those of the present work, as the non-linear response becomes less important. While the full-MSS results exhibit strong fluctuations due to thermal noise, the ML predictions are considerably smoother. Regarding the speedup, the CPU time of the ML prediction is about 6 times smaller than that of full-MSS, with both solvers parallelized on CPUs using MPI.

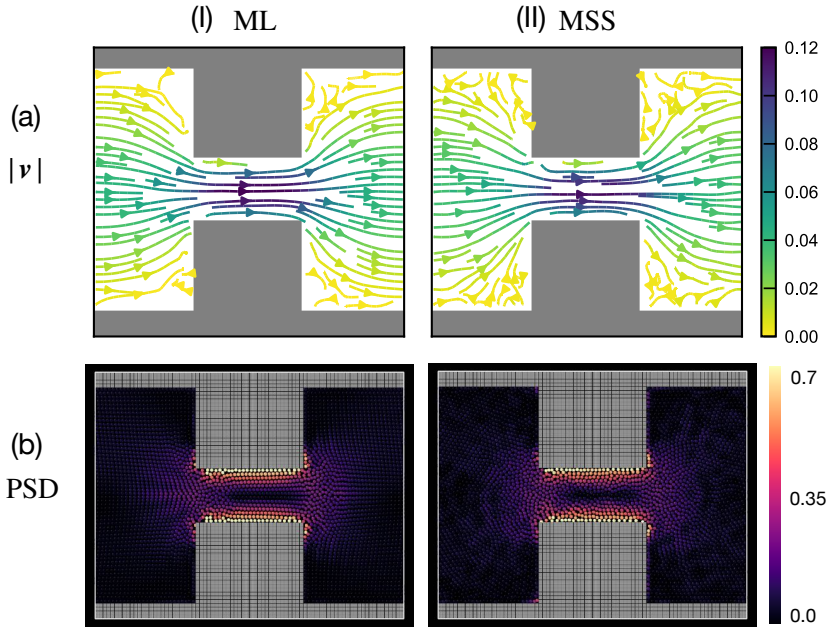

Fig. 3.5 Simulation snapshots of the contraction expansion flow at steady state, for the (left) ML-MSS and (right) full-MSS result. The upper and lower panels show the streamlines and principal stress differences (PSD), color-coded by their respective magnitudes.

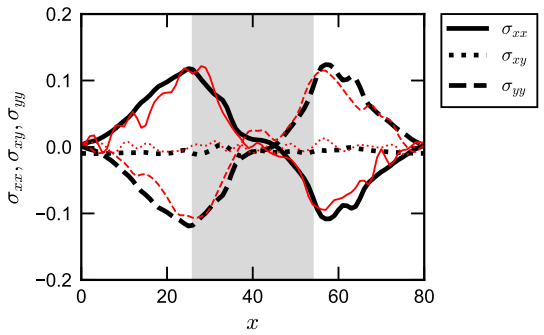

Fig. 3.6 Steady-state stress profiles along horizontal center line. The thick (thin) lines are the ML-MSS (full-MSS) results, where the solid, dotted, and dashed lines correspond to $\sigma_{xx}, \sigma_{xy}, \sigma_{yy}$, respectively. The gray background indicates the narrow slit region.

3.4 Conclusions

In this chapter, we presented the improved approach for ML-based MSS method for the general two-dimensional flows. The proposed approach is assessed by analyzing the two startup flows between the parallel plates and in the construction expansion channel. In typical elastic conditions, the predictions successfully reproduce the direct MSS results for the profiles contributed by the history-dependent fluid elements even under a steady state. The error retains the same order of magnitude before extension, slightly reduced from the previous case in Chapter 2 due to the dimensional increase in the regression

model. Although the present ML-based simulation performed on CPUs is not fully accelerated, the calculation time is accelerated six times. This reasonable and successful example has clearly provided the direction of development of the proposed method. The accuracy is reliably high within a given typical or weaker elastic regime, but we have also observed decreased accuracy at higher strain rates, i.e., for a more significant pressure gap. Thus, a more effective learning protocol should be developed. We can discuss such prospects from the viewpoint of a data-driven approach.

Chapter 4

Symbolic Regression Technique for Discovering Constitutive Relations

4.1 Introduction

In the previous Chapters 2 and 3, we use Gaussian process regressions for identify the constitutive relation of the microscopic model. However, such a ML model needs computational resources to learn and infer the predictions based on the training dataset. In this Chapter 4, we employ a symbolic regression method to help us to use a transparent model and additionally provide an economical model with sparsity-promoted techniques. We confirm the ability to (re-)identify the constitutive relations of the phenomenological and microscopic models whose constitutive equations are known or unknown.

Mathematical models grounded in physical laws are indispensable across science and engineering, offering profound insights into complex system behaviors. These models elucidate the underlying mechanisms governing system dynamics and empower predictions and innovations in technology and natural science. Traditionally, model derivation has leaned heavily on theoretical and empirical knowledge, often requiring expert knowledge and intuition. On the other hand, data-driven methods have become capable of assisting in developing mathematical models and constructing models that provide advanced predictions [9]. These data-driven methods involve the sparse identification methods [43, 97–99], symbolic regression methods [100–103], and physics-informed machine learning methods [44, 104–106]. These methods have emerged as powerful tools for deriving governing equations directly from data, overcoming the limitations of conventional expert-dependent approaches.

Rheology is one of the scientific fields that address flows of any materials, which plays a crucial role in many industries, such as designs of chemical processes, by providing insights into flow behaviors of complex fluids. One of the roles of rheology is to discover or derive governing equations that relate deformation and stress, referred to as *constitutive equations*. From an engineering perspective, accurate constitutive equations are necessary to predict the flow of complex fluids under complex boundary conditions. Nevertheless, it is generally difficult to theoretically obtain constitutive equations for complex fluids. Instead, mesoscopic coarse-grained models, which are based on molecular theories, have been explored in the field of rheology. For example, for polymeric liquids, standard molecular theories have been proposed [6, 14], on which refined mesoscopic models have been constructed [22, 23, 107]. In these models, the motion of individual (coarse-grained) molecules is numerically tracked. Although these models require significantly more computational time compared to constitutive equations, they can reproduce (nearly) accurate rheological *data*. Despite these advancements, a clear methodology for

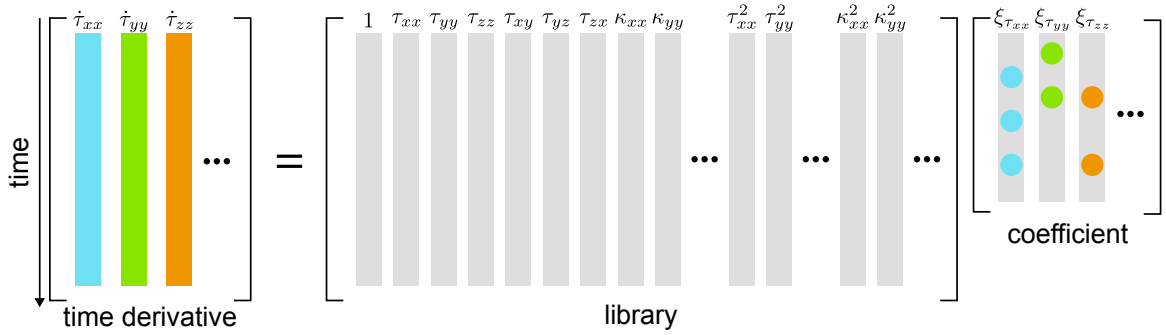

Fig. 4.1 Schematic illustration of *Rheo*-SINDy.

obtaining constitutive equations from available data remains elusive.

Data-driven methods are powerful approaches for addressing the aforementioned challenges in rheology. Indeed, such methods have enhanced rheological studies such as constitutive modeling, flow predictions of complex fluid flows, and model selections [10, 12]. Some applications have successfully identified constitutive relations of complex fluids or governing equations to predict the dynamics of fluids with knowledge of rheology. These studies have employed neural networks (NN), including deep NN [60], graph NN [108], recurrent NN [59], physics-informed NN [67, 83, 84], multi-fidelity NN [109], and tensor basis NN [58]. Gaussian processes (GP) have also been employed, for example, for strain-rate dependent viscosity [54] or for viscoelastic properties [55, 56, 61, 68].

Despite the success of NNs and GPs, their black-box nature often obscures the underlying physics, making symbolic regression techniques more appealing for transparency and interoperability. These methods, such as the sparse identification of nonlinear dynamics (SINDy) [43], have been frequently utilized to track (reduced order) dynamics in the field of fluid dynamics [110]. Inspired by these successes, symbolic regression methods have recently started to be used in the field of rheology as well. For example, Mohammadamin and coworkers [111] relied on the SINDy for flexibly identifying the constitutive equations of an elasto-visco-plastic fluid. Although there are several attempts along this line, a comprehensive study to test the SINDy for rheological data has not yet been conducted.

In this study, we employ the SINDy to find constitutive models from rheological data, which we call as *Rheo*-SINDy. After verifying the performance of *Rheo*-SINDy when the constitutive equations are known, we apply *Rheo*-SINDy to problems where the constitutive equations are unknown. The details are shown below.

4.2 Methods

4.2.1 *Rheo*-SINDy

We use a data-driven method known as a sparse identification of nonlinear dynamics (SINDy), which was originally developed by Brunton and coworkers [43]. In this study, we attempt to obtain constitutive equations of complex fluids using the SINDy. Here, we briefly explain the basic concepts of the SINDy.

We consider dynamical systems generally expressed by the following differential equation:

$$\frac{\mathrm{d}\boldsymbol{x}(t)}{\mathrm{d}t} = \boldsymbol{f}[\boldsymbol{x}(t)], \tag{4.1}$$

where the vector $\boldsymbol{x}(t)$ represents the state of a system at time t and the function $\boldsymbol{f}[\boldsymbol{x}(t)]$ determines the dynamics of the state $\boldsymbol{x}(t)$. In general, while there are many possible candidate terms for $\boldsymbol{f}[\boldsymbol{x}(t)]$, the right-hand side of Eq. (4.1) is assumed to include only a few terms on its appropriate coordinate. The basic idea of the SINDy is to find dominant terms for describing the dynamics out of the numerous options using a sparse identification method. One can determine the (sparse) representation of $\boldsymbol{f}$ by a dataset including a collection of $\boldsymbol{x}(t)$ and $\dot{\boldsymbol{x}}(t)$ (the time derivative of $\boldsymbol{x}(t)$). The regression to points of $\boldsymbol{x}(t)$ and $\dot{\boldsymbol{x}}(t)$ is computed with sparsity-promoting techniques, such as ℓ_1-regularization.

In the rheological community, it is of great importance to determine a relationship between stress and strain rate. This relationship is a so-called constitutive model or constitutive equation. Most constitutive equations are differential equations that depend on the (extra) stress tensor $\boldsymbol{\tau}$ and velocity gradient tensor $\boldsymbol{\kappa}$. In this study, we prefer to use the so-called extra stress tensor $\boldsymbol{\tau}$ as the stress tensor because this stress tensor is $\boldsymbol{\tau} = \boldsymbol{0}$ at equilibrium, which is convenient for the SINDy regression. The total stress tensor $\boldsymbol{\sigma}$ can be obtained by the relation $\boldsymbol{\tau} = \boldsymbol{\sigma} - G\boldsymbol{I}$, where G is the modulus and $\boldsymbol{I}$ is the unit tensor. A general form for constitutive equations can be written as

$$\frac{\mathrm{d}\boldsymbol{\tau}(t)}{\mathrm{d}t} = \dot{\boldsymbol{\tau}}(t) = \boldsymbol{f}[\boldsymbol{\tau}(t), \boldsymbol{\kappa}(t)]. \tag{4.2}$$

Here, $\boldsymbol{\kappa}(t)$ is a control variable during rheological measurements. We use the SINDy algorithm to find constitutive equations for complex fluids, which we call this technique *Rheo*-SINDy.

The training data needed to *Rheo*-SINDy are transient stress data $\boldsymbol{T}$ and those time derivatives $\dot{\boldsymbol{T}}$, which can be summarized as the following two matrices:

$$\boldsymbol{T} = \begin{bmatrix} \boldsymbol{t}_{xx} & \boldsymbol{t}_{yy} & \cdots & \boldsymbol{t}_{zx} \end{bmatrix} = \begin{bmatrix} \tau_{xx}(t_1) & \tau_{yy}(t_1) & \cdots & \tau_{zx}(t_1) \\ \tau_{xx}(t_2) & \tau_{yy}(t_2) & \cdots & \tau_{zx}(t_2) \\ \vdots & \vdots & \ddots & \vdots \\ \tau_{xx}(t_n) & \tau_{yy}(t_n) & \cdots & \tau_{zx}(t_n) \end{bmatrix} \tag{4.3}$$

and

$$\dot{\boldsymbol{T}} = \begin{bmatrix} \dot{\boldsymbol{t}}_{xx} & \dot{\boldsymbol{t}}_{yy} & \cdots & \dot{\boldsymbol{t}}_{zx} \end{bmatrix} = \begin{bmatrix} \dot{\tau}_{xx}(t_1) & \dot{\tau}_{yy}(t_1) & \cdots & \dot{\tau}_{zx}(t_1) \\ \dot{\tau}_{xx}(t_2) & \dot{\tau}_{yy}(t_2) & \cdots & \dot{\tau}_{zx}(t_2) \\ \vdots & \vdots & \ddots & \vdots \\ \dot{\tau}_{xx}(t_n) & \dot{\tau}_{yy}(t_n) & \cdots & \dot{\tau}_{zx}(t_n) \end{bmatrix}, \tag{4.4}$$

where $\boldsymbol{t}_{\mu\nu}$ $(\mu, \nu \in \{x, y, z\})$ is the column of $\boldsymbol{T}$, and we take the stress data for n sequential times. The time derivatives of the stress data $\dot{\boldsymbol{T}}$ are computed by a numerical differentiation method. To take the stress data, we apply the velocity gradient $\boldsymbol{\kappa}$ to the system. The data of the velocity gradient tensor $\boldsymbol{K}$ are summarized as

$$\boldsymbol{K} = \begin{bmatrix} \boldsymbol{k}_{xx} & \boldsymbol{k}_{yy} & \cdots & \boldsymbol{k}_{zx} \end{bmatrix} = \begin{bmatrix} \kappa_{xx}(t_1) & \kappa_{yy}(t_1) & \cdots & \kappa_{zx}(t_1) \\ \kappa_{xx}(t_2) & \kappa_{yy}(t_2) & \cdots & \kappa_{zx}(t_2) \\ \vdots & \vdots & \ddots & \vdots \\ \kappa_{xx}(t_n) & \kappa_{yy}(t_n) & \cdots & \kappa_{zx}(t_n) \end{bmatrix}, \tag{4.5}$$

where $\boldsymbol{k}_{\mu\nu}$ $(\mu, \nu \in \{x, y, z\})$ is the the column of $\boldsymbol{K}$.

In *Rheo*-SINDy, we construct a library matrix of functions, denoted as $\boldsymbol{\Theta}$, which can include various nonlinear functions. $\boldsymbol{\Theta}$ is expressed as

$$\boldsymbol{\Theta} = \begin{bmatrix} \boldsymbol{1} & \boldsymbol{T} & \boldsymbol{K} & (\boldsymbol{T} \otimes \boldsymbol{T}) & (\boldsymbol{T} \otimes \boldsymbol{K}) & (\boldsymbol{K} \otimes \boldsymbol{K}) & \cdots \end{bmatrix}, \tag{4.6}$$

where $\boldsymbol{T} \otimes \boldsymbol{K}$, for example, denotes all possible combinations of the products of the row components in $\boldsymbol{T}$ and $\boldsymbol{K}$ for each time t_i $(1 \leq i \leq n)$. We note that $\boldsymbol{\Theta}$ can incorporate not only polynomials but also other functions, such as sinusoidal functions. Using these expressions, we can substitute Eq. (4.2) as

$$\dot{\boldsymbol{T}} = \boldsymbol{\Theta}\boldsymbol{\Xi}, \tag{4.7}$$

where $\boldsymbol{\Xi}$ is the coefficient matrix. The coefficient matrix can be written as

$$\boldsymbol{\Xi} = \begin{bmatrix} \boldsymbol{\xi}_{xx} & \boldsymbol{\xi}_{yy} & \cdots & \boldsymbol{\xi}_{zx} \end{bmatrix} = \begin{bmatrix} \xi_{xx,1} & \xi_{yy,1} & \cdots & \xi_{zx,1} \\ \xi_{xx,2} & \xi_{yy,2} & \cdots & \xi_{zx,2} \\ \vdots & \vdots & \ddots & \vdots \\ \xi_{xx,N_{\boldsymbol{\Theta}}} & \xi_{yy,N_{\boldsymbol{\Theta}}} & \cdots & \xi_{zx,N_{\boldsymbol{\Theta}}} \end{bmatrix}. \tag{4.8}$$

where $N_{\boldsymbol{\Theta}}$ is the total number of library functions.

To determine the coefficient matrix $\boldsymbol{\Xi}$, we solve the following optimization problem:

$$\hat{\boldsymbol{\xi}}_{\mu\nu} = \underset{\boldsymbol{\xi}_{\mu\nu}}{\operatorname{argmin}} \|\dot{\boldsymbol{t}}_{\mu\nu} - \boldsymbol{\Theta}\boldsymbol{\xi}_{\mu\nu}\|_2^2 + R(\boldsymbol{\xi}_{\mu\nu}), \tag{4.9}$$

where $||\cdots||_2$ is the ℓ_2 norm defined as

$$||\boldsymbol{x}||_2 = \left(\sum_i x_i^2 \right)^{1/2}, \tag{4.10}$$

and $R(\boldsymbol{\xi}_{\mu\nu})$ is the regularization term. To obtain a sparse solution of $\boldsymbol{\Xi}$, we apply the following five methods: (i) the sequentially thresholded least square algorithm (STLSQ), (ii) sequentially thresholded Ridge regression (STRidge), (iii) least absolute shrinkage and selection operator (Lasso), (iv) Elastic-Net (E-Net), and (v) adaptive-Lasso (a-Lasso) (see 4.A for detail). Each method has a hyperparameter α to penalize the solution complexity, which is to be tuned for obtaining well-predictive yet parsimonious representations. For this purpose, we attempt to re-identify known constitutive equations by (i)–(v) with various α values and pick an *appropriate* value of α that gives a small loss value and the (nearly) correct number of terms.

In this study, we limit ourselves to *shear* rheological measurements that give fundamental rheological properties. Under shear flow, among the components $\boldsymbol{\kappa}$, only κ_{xy} has non-zero values. Here, x is the velocity direction, and y is the velocity gradient direction. Since the major stress components are τ_{xx}, τ_{yy}, τ_{zz}, and τ_{xy} under shear flow, we only use these components to conduct *Rheo*-SINDy.

4.3 Case Studies

For case studies of *Rheo*-SINDy, we first test whether *Rheo*-SINDy can find the appropriate constitutive equation from the training data obtained by several phenomenological and molecular-based constitutive equations. Subsequently, we consider *approximate* constitutive models of a mesoscopic model, whose constitutive equation is unknown. This section provides a brief overview of the models considered in this study and the conditions for creating the datasets.

4.3.1 Constitutive Equation Models

Upper Convected Maxwell (UCM) Model

The simplest constitutive equation is the upper convected Maxwell (UCM) model [112] shown as

$$\frac{\mathrm{d}\boldsymbol{\tau}}{\mathrm{d}t} - \boldsymbol{\tau}\cdot{}^{t}\boldsymbol{\kappa} - \boldsymbol{\kappa}\cdot\boldsymbol{\tau} = -\frac{1}{\lambda}\boldsymbol{\tau} + 2G\boldsymbol{D}. \tag{4.11}$$

Here, the left-hand side of Eq. (4.11) is the upper-convected time derivative of $\boldsymbol{\tau}$, λ is the relaxation time, G is the modulus, and $\boldsymbol{D}$ is the deformation rate tensor defined as $\boldsymbol{D} = (\boldsymbol{\kappa} + {}^{t}\boldsymbol{\kappa})/2$. Using λ as the unit time and G as the unit stress (i.e., $\lambda = G = 1$), we can obtain dimensionless expressions for time $\tilde{t} = t/\lambda$, velocity gradient tensor $\tilde{\boldsymbol{\kappa}} = \lambda\boldsymbol{\kappa}$, and stress $\tilde{\boldsymbol{\tau}} = \boldsymbol{\tau}/G$. In what follows, we omit the tilde in dimensionless variables for simplicity. The dimensionless form of the UCM model under shear flow is thus written as

$$\dot{\tau}_{xx} = -\tau_{xx} + 2\tau_{xy}\kappa_{xy}, \tag{4.12}$$

$$\dot{\tau}_{yy/zz} = \tau_{yy/zz} = 0, \tag{4.13}$$

$$\dot{\tau}_{xy} = -\tau_{xy} + \kappa_{xy} + \tau_{yy}\kappa_{xy} = -\tau_{xy} + \kappa_{xy}. \tag{4.14}$$

Here, since the initial conditions for $\boldsymbol{\tau}$ are set to the values of $\boldsymbol{\tau}$ at equilibrium, namely $\boldsymbol{\tau} = \boldsymbol{0}$, $\tau_{yy/zz}$ of the UCM model is zero under shear flow.

For the UCM model, we generate training data by numerically solving Eqs. (4.12)–(4.14) under two shear flow scenarios: simple shear and oscillatory shear tests. For the simple shear test, the shear rate is kept constant ($\kappa_{xy} = \dot{\gamma}$) across various values ($\dot{\gamma} \in \{1, 1.7, 2.8, 4.6, 7.7, 13, 22, 36, 60, 100\}$) with simulations running from $t = 0$ to $t = 10$ using a time step of $\Delta t = 1.0 \times 10^{-4}$. The oscillatory shear test introduces a time-dependent oscillatory shear strain, $\gamma(t) = \gamma_0 \sin(\omega t)$, with $\gamma_0 = 2$ and $\omega = 1$, over a period from $t = 0$ to $t = 100$, employing the same time step. In both tests, data are collected at intervals of $\Delta t_{\mathrm{train}} = 1 \times 10^{-2}$, resulting in a total of 10^4 data points for the training data.

Giesekus Model

The Giesekus model, which is one of the phenomenological constitutive equations [29], shows typical shear rheological properties and is used to fit various complex fluids, including polymer solutions and wormlike micellar solutions. The tensorial form of the Giesekus constitutive equation can be written as

$$\frac{\mathrm{d}\boldsymbol{\tau}}{\mathrm{d}t} - \boldsymbol{\tau}\cdot{}^{t}\boldsymbol{\kappa} - \boldsymbol{\kappa}\cdot\boldsymbol{\tau} = -\frac{1}{\lambda}\boldsymbol{\tau} - \frac{\alpha_{\mathrm{G}}}{G\lambda}\boldsymbol{\tau}\cdot\boldsymbol{\tau} + 2G\boldsymbol{D}, \tag{4.15}$$

where α_{G} is the parameter governing the nonlinear response of the Giesekus model. The Giesekus equation under shear flow is thus given by

$$\dot{\tau}_{xx} = -\tau_{xx} - \alpha_{\mathrm{G}}(\tau_{xx}^2 + \tau_{xy}^2) + 2\tau_{xy}\kappa_{xy}, \tag{4.16}$$

$$\dot{\tau}_{yy} = -\tau_{yy} - \alpha_{\mathrm{G}}(\tau_{yy}^2 + \tau_{xy}^2), \tag{4.17}$$

$$\dot{\tau}_{zz} = 0, \tag{4.18}$$

$$\dot{\tau}_{xy} = -\tau_{xy} - \alpha_{\mathrm{G}}(\tau_{xx} + \tau_{yy})\tau_{xy} + \tau_{yy}\kappa_{xy} + \kappa_{xy}. \tag{4.19}$$

Here, all quantities are non-dimensionalized by using λ as the unit time and G as the unit stress. From Eqs. (4.16)–(4.19), the total number of collect terms in the Giesekus model is 12.

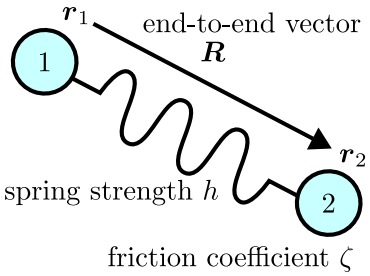

Fig. 4.2 Schematic illustration of the dumbbell model.

We generate the training data by solving Eqs. (4.16)–(4.19) numerically with $\alpha_{\mathrm{G}} = 0.5$ and $\Delta t = 1 \times 10^{-4}$. We note that the Giesekus model with $\alpha_{\mathrm{G}} = 0.5$ gives sufficient nonlinear features under shear flow. We applied the oscillatory shear flow with $\gamma_0 = 2$ and various ω values ($\omega \in \{0.1, 0.2, \ldots, 1\}$) for $0 \leq t \leq 100$. From the computed stress data, we collected data at the interval of $\Delta t_{\mathrm{train}} = 1 \times 10^{-2}$.

4.3.2 Dumbbell Models

The dumbbell-based models have been widely utilized in numerous previous studies for the computation of viscoelastic fluids and are considered a standard mesoscopic model for viscoelastic fluids [74]. As illustrated in Fig. 4.2, a dumbbell consists of two beads (indexed as 1 or 2) and a spring that connects them. The Langevin equations for the positions of the two beads $\boldsymbol{r}_{1/2}(t)$ can be written as

$$\zeta \left[\frac{\mathrm{d}\boldsymbol{r}_i(t)}{\mathrm{d}t} - \boldsymbol{\kappa} \cdot \boldsymbol{r}_i(t) \right] = -h(t) \left\{ \boldsymbol{r}_i(t) - \boldsymbol{r}_j(t) \right\} + \boldsymbol{F}_{\mathrm{B}i}(t), \tag{4.20}$$

with $(i, j) = (1, 2)$ or $(2, 1)$. Here, ζ is the friction coefficient, $h(t)$ is the spring strength, and $\boldsymbol{F}_{\mathrm{B}i}(t)$ is the Brownian force acting on the bead i. The time evolution equation for the end-to-end vector $\boldsymbol{R}$ $(\boldsymbol{r}_2(t) - \boldsymbol{r}_1(t))$ of the beads is thus obtained as

$$\zeta \left[\frac{\mathrm{d}\boldsymbol{R}(t)}{\mathrm{d}t} - \boldsymbol{\kappa} \cdot \boldsymbol{R}(t) \right] = -2h(t)\boldsymbol{R}(t) + \left\{ \boldsymbol{F}_{\mathrm{B}2}(t) - \boldsymbol{F}_{\mathrm{B}1}(t) \right\}. \tag{4.21}$$

The Brownian force is characterized by the first and second-moment averages as

$$\langle \boldsymbol{F}_{\mathrm{B}i}(t) \rangle = \boldsymbol{0}, \tag{4.22}$$

and

$$\langle \boldsymbol{F}_{\mathrm{B}i}(t) \boldsymbol{F}_{\mathrm{B}j}(t') \rangle = 2\zeta k_{\mathrm{B}} T \delta_{ij} \delta(t - t') \boldsymbol{I}, \tag{4.23}$$

where k_{B} is the Boltzmann constant and T is the temperature. The stress tensor is obtained as

$$\boldsymbol{\tau}(t) = \nu \langle h(t) \boldsymbol{R}(t) \boldsymbol{R}(t) \rangle - \rho k_{\mathrm{B}} T \boldsymbol{I}, \tag{4.24}$$

where ρ is the density of dumbbells.

There are several expressions for the spring strength $h(t)$. The most basic one is the Hookean spring, defined as

$$h(t) = h_{\mathrm{eq}} = \frac{3 k_{\mathrm{B}} T}{n_{\mathrm{K}} b_{\mathrm{K}}^2}, \tag{4.25}$$

where n_K is the number of Kuhn segments per spring and b_K is the Kuhn length. To reproduce the properties of polymers, dumbbell models with finite extensible nonlinear elastic (FENE) springs are widely used. The empirical expression of the FENE spring is

$$h(t) = h_\mathrm{eq}\frac{1-\langle R_\mathrm{eq}^2\rangle/R_\mathrm{max}^2}{1-\boldsymbol{R}^2(t)/R_\mathrm{max}^2}, \tag{4.26}$$

where $\langle R_\mathrm{eq}^2\rangle^{1/2} = (n_\mathrm{K})^{1/2}b_\mathrm{K}$ is the equilibrium length of the springs, and $R_\mathrm{max} = n_\mathrm{K}b_\mathrm{K}$ is the maximum length of the springs. As shown later in Sec. 4.3.2, a constitutive equation cannot be analytically obtained for the FENE dumbbell model. To address the FENE spring more analytically, the following approximate expression of the FENE spring has been proposed:

$$h(t) = h_\mathrm{eq}f_\mathrm{FENE}(t),\ \text{where}\ f_\mathrm{FENE}(t) = \frac{1-\langle R_\mathrm{eq}^2\rangle/R_\mathrm{max}^2}{1-\langle\boldsymbol{R}^2(t)\rangle/R_\mathrm{max}^2}. \tag{4.27}$$

This spring is referred to as the FENE-P spring. Here, "P" means Peterlin, who proposed the approximate form of the FENE spring law.

We use $\lambda = \zeta/4h_\mathrm{eq}$ as the unit time and $G = \rho k_\mathrm{B}T$ as the unit stress for the dumbbell models. To simplify the expressions, we omit the tilde representing dimensionless quantities.

Hookean Dumbbell Model

The most basic dumbbell model is the Hookean dumbbell model, where Hookean springs are employed (cf. Eq. (4.25)). Using Eqs. (4.21), (4.24), and (4.25), the Hookean dumbbell model reduces to the constitutive equation of the UCM model (cf. Eq. (4.11)) in the limit of $N_\mathrm{p} \to \infty$ with N_p being the number of dumbbells.

For the Hookean dumbbell model, we generate training data by Brownian dynamics (BD) simulations with the finite numbers of dumbbells ($N_\mathrm{p} \in \{10^3, 10^4, 10^5\}$) under the oscillatory shear flows same as those in the Giesekus model. The simulations are run with $\Delta t = 1\times10^{-3}$ for $0 \le t \le 100$ and data are collected at the interval of $\Delta t_\mathrm{train} = 1\times10^{-2}$. Each simulation is conducted with five different random seeds, and their average data is used for training. Due to the characteristics of the BD simulation, the training data inherently include noise originating from the finite N_p. We here test whether Eqs. (4.12)–(4.14) can be discovered from the noisy data.

FENE-P Dumbbell Model

We next address the so-called FENE-P dumbbell model, where Eq. (4.27) is utilized as the spring strength. As shown below, the FENE-P dumbbell model has an analytical solution and is utilized for various flow problems, such as turbulent flows [113].

Due to the assumption shown in Eq. (4.27), a simple representation of the time evolution for the conformation tensor $\boldsymbol{C} = \langle\boldsymbol{R}(t)\boldsymbol{R}(t)\rangle$ can be obtained as

$$\frac{\mathrm{d}\boldsymbol{C}}{\mathrm{d}t} - \boldsymbol{C}\cdot{}^t\boldsymbol{\kappa} - \boldsymbol{\kappa}\cdot\boldsymbol{C} = -f_\mathrm{FENE}(t)\boldsymbol{C} + \frac{n_\mathrm{K}}{3}\boldsymbol{I}. \tag{4.28}$$

The stress tensor is thus obtained by

$$\boldsymbol{\tau}(t) = \rho k(t)\boldsymbol{C}(t) - \rho k_\mathrm{B}T\boldsymbol{I}. \tag{4.29}$$

Under shear flow, Eq. (4.28) reduces to the following expressions:

$$\dot{C}_{xx} = -f_\mathrm{FENE}C_{xx} + 2C_{xy}\kappa_{xy} + \frac{n_\mathrm{K}}{3}, \tag{4.30}$$

$$\dot{C}_{yy/zz} = -f_{\mathrm{FENE}} C_{yy/zz} + \frac{n_{\mathrm{K}}}{3}, \tag{4.31}$$

$$\dot{C}_{xy} = -f_{\mathrm{FENE}} C_{xy} + C_{yy}\kappa_{xy}. \tag{4.32}$$

Using *Rheo*-SINDy, we test whether or not Eqs. (4.30)–(4.32) can be found from the data.

While it has not been as widely recognized due to its complexity, the FENE-P dumbbell model can also be expressed in the form of the constitutive equation (i.e., the stress expression) [114]. From the textbook of Bird and coworkers [74], the constitutive equation for the FENE-P model is

$$\frac{\mathrm{d}\boldsymbol{\tau}}{\mathrm{d}t} - \boldsymbol{\tau}\cdot{}^{t}\boldsymbol{\kappa} - \boldsymbol{\kappa}\cdot\boldsymbol{\tau} = -f_{\mathrm{FENE}}(t)\boldsymbol{\tau} + 2\boldsymbol{D} + \frac{\mathrm{D}\ln Z}{\mathrm{D}t}(\boldsymbol{\tau} + \boldsymbol{I}), \tag{4.33}$$

where $\mathrm{D}(\cdots)/\mathrm{D}t$ is the substantial derivative and Z is the function expressed as

$$Z = \frac{1}{1 - \langle \boldsymbol{R}^2(t)/R_{\max}^2 \rangle} = 1 + \frac{1}{3n_{\mathrm{K}} Z_{\mathrm{eq}}^{-1}}(\mathrm{tr}\boldsymbol{\tau} + 3). \tag{4.34}$$

Here, Z_{eq} indicates Z at equilibrium. From Eq. (4.34), we can see that $\mathrm{tr}\boldsymbol{\tau}$ is tightly related to the (squared) length of dumbbells. Since we do not address the spatial gradient in rheological calculations, $\mathrm{D}(\cdots)/\mathrm{D}t$ simply reduces to $\mathrm{d}(\cdots)/\mathrm{d}t$. Using Eqs. (4.28), (4.33), and (4.34), the constitutive equations for the FENE-P dumbbell model under shear flow can be expressed as

$$\begin{aligned}
\dot{\tau}_{xx} \quad = &-\left\{1 + \frac{1}{3(n_{\mathrm{K}}-1)}\right\}\tau_{xx} - \frac{1}{3(n_{\mathrm{K}}-1)}(\tau_{yy} + \tau_{zz}) \\
&- \frac{1}{9(n_{\mathrm{K}}-1)}(\mathrm{tr}\,\boldsymbol{\tau})^2 - \frac{1}{3n_{\mathrm{K}}}\left(2 + \frac{1}{n_{\mathrm{K}}-1}\right)\mathrm{tr}\,\boldsymbol{\tau}\tau_{xx} \\
&+ 2\left\{1 + \frac{1}{3(n_{\mathrm{K}}-1)}\right\}\tau_{xy}\kappa_{xy} - \frac{1}{9(n_{\mathrm{K}}-1)}(\mathrm{tr}\,\boldsymbol{\tau})^2\tau_{xx} \\
&+ \frac{2}{3(n_{\mathrm{K}}-1)}\tau_{xx}\tau_{xy}\kappa_{xy},
\end{aligned} \tag{4.35}$$

$$\begin{aligned}
\dot{\tau}_{yy/zz} = &-\left\{1 + \frac{1}{3(n_{\mathrm{K}}-1)}\right\}\tau_{yy/zz} - \frac{1}{3(n_{\mathrm{K}}-1)}(\tau_{xx} + \tau_{zz/yy}) \\
&- \frac{1}{9(n_{\mathrm{K}}-1)}(\mathrm{tr}\,\boldsymbol{\tau})^2 - \frac{1}{3n_{\mathrm{K}}}\left(2 + \frac{1}{n_{\mathrm{K}}-1}\right)\mathrm{tr}\,\boldsymbol{\tau}\tau_{yy/zz} \\
&+ \frac{2}{3(n_{\mathrm{K}}-1)}\tau_{xy}\kappa_{xy} - \frac{1}{9(n_{\mathrm{K}}-1)}(\mathrm{tr}\,\boldsymbol{\tau})^2\tau_{yy/zz} \\
&+ \frac{2}{3(n_{\mathrm{K}}-1)}\tau_{yy/zz}\tau_{xy}\kappa_{xy},
\end{aligned} \tag{4.36}$$

$$\begin{aligned}
\dot{\tau}_{xy} = &-\tau_{xy} + \kappa_{xy} + \tau_{yy}\kappa_{xy} - \frac{1}{3n_{\mathrm{K}}}\left(2 + \frac{1}{n_{\mathrm{K}}-1}\right)\mathrm{tr}\,\boldsymbol{\tau}\tau_{xy} \\
&- \frac{1}{9(n_{\mathrm{K}}-1)}(\mathrm{tr}\,\boldsymbol{\tau})^2\tau_{xy} + \frac{2}{3(n_{\mathrm{K}}-1)}\tau_{xy}^2\kappa_{xy}.
\end{aligned} \tag{4.37}$$

For the derivation, please refer to 4.C. From Eqs. (4.35)–(4.37), we can see that the constitutive equation for the FENE-P model can be expressed by a polynomial of up to third degree in $\boldsymbol{\tau}$ and $\boldsymbol{\kappa}$. Here, we note that Eqs. (4.35)–(4.37) become equivalent to the UCM model shown in Eqs. (4.12)–(4.14) in the limit of $n_{\mathrm{K}} \to \infty$.

To generate noise-free training data, we use Eqs. (4.29)–(4.32) with $n_{\mathrm{K}} = 10$ and $\Delta t = 1 \times 10^{-4}$ for $0 \le t \le 100$. We apply the oscillatory shear flows the same as those in the Giesekus model. From the computed stress data, we collect data at the interval of $\Delta t_{\mathrm{train}} = 1 \times 10^{-2}$.

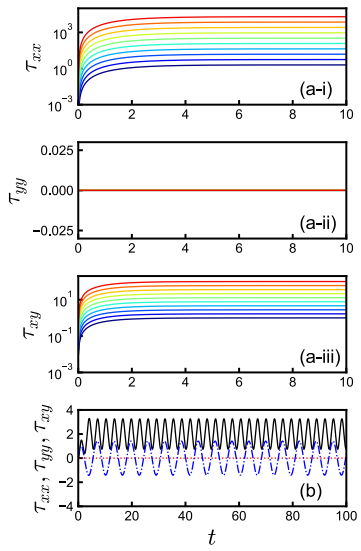

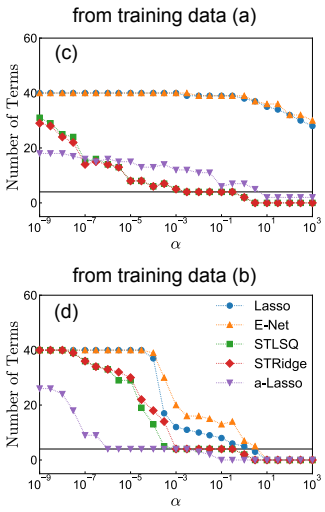

(e) SINDy results

data	method	α	equations
(a)	STRidge	3×10^{-3}	$\dot{\tau}_{xx} = -1.000\tau_{xx} + 2.000\tau_{xy}\kappa_{xy}$ $\dot{\tau}_{yy} = 0.000$ $\dot{\tau}_{xy} = -1.000\tau_{xy} + 1.000\kappa_{xy}$
(a)	a-Lasso	1×10^{-1}	$\dot{\tau}_{xx} = -1.239\tau_{xx} + 0.983\tau_{xy}^2 + 1.385\tau_{xy}\kappa_{xy} + 0.100\kappa_{xy}^2$ $\dot{\tau}_{yy} = 0.000$ $\dot{\tau}_{xy} = -0.997\tau_{xy} + 0.997\kappa_{xy}$
(b)	STRidge	3×10^{-3}	$\dot{\tau}_{xx} = -1.000\tau_{xx} + 2.000\tau_{xy}\kappa_{xy}$ $\dot{\tau}_{yy} = 0.000$ $\dot{\tau}_{xy} = -1.000\tau_{xy} + 1.000\kappa_{xy}$
(b)	a-Lasso	1×10^{-6}	$\dot{\tau}_{xx} = -1.000\tau_{xx} + 2.000\tau_{xy}\kappa_{xy}$ $\dot{\tau}_{yy} = 0.000$ $\dot{\tau}_{xy} = -1.000\tau_{xy} + 1.000\kappa_{xy}$

Fig. 4.3 Training data obtained by the UCM model (a) under simple shear flow ($\kappa_{xy} = \dot{\gamma}$) and (b) under oscillatory shear flow ($\kappa_{xy} = \gamma_0 \omega \cos(\omega t)$). The number of total terms obtained by (c) the training data (a) (i.e., simple shear flow) and (d) the training data (b) (i.e., oscillatory shear flow). (e) The constitutive equations obtained by *Rheo*-SINDy. The parameters for the applied shear flows to obtain the training data are summarized in Sec. 4.3.1. In (b), xx-, yy-, and xy-components of the stress tensor are plotted with the black solid, red dotted, and blue dash-dotted lines, respectively. In (c) and (d), the number of total terms for five different optimization methods is plotted against the hyperparameter α. The black horizontal lines in (c) and (d) indicate the correct number of the terms in the UCM model.

FENE Dumbbell Model

We finally address the FENE dumbbell model, where the spring strength is represented by Eq. (4.26). Since the FENE dumbbell model does not use any simplification for the spring strength (e.g., Peterlin approximation shown in Eq. (4.27)), its analytical constitutive equation has not been obtained. We apply *Rheo*-SINDy to this case to see if an "approximate" constitutive equation can be obtained. The obtained equations are validated by comparing the data obtained by numerically solving them with the data obtained by BD simulations.

The training data are generated by the BD simulations using Eqs. (4.21)–(4.24) and (4.26) with $n_\mathrm{K} = 10$, $N_\mathrm{p} = 10^4$, and $\Delta t = 1 \times 10^{-2}$ for $0 \leq t \leq 100$. We apply the oscillatory shear flows with the same parameters as those in the Giesekus model. Since we do not use any approximation for the spring strength, the values of $h(t)$ differ for each individual dumbbell. The BD simulation results with five different random seeds are averaged for each condition. From the computed stress data, we collected data at the interval of $\Delta t_\mathrm{train} = 1 \times 10^{-2}$.

4.4 Results and Discussions

4.4.1 Re-Identifying Upper Convected Maxwell Model

Through this case study, we first check the appropriate methods to take the shear rheological data for *Rheo*-SINDy. Figure 4.3 shows the training data and results for the UCM model. Figure 4.3(a) and (b) are the stress data under simple shear flows with various shear rates and those under oscillatory shear flows.

We conducted the *Rheo*-SINDy regressions by using the polynomial library that includes up to third order terms of τ_{xx}, τ_{yy}, τ_{xy}, and κ_{xy}. Thus, there were 35 candidate terms for each component of the constitutive equation. The terms related to τ_{zz} were excluded because they do not contribute to the UCM dynamics. The correct number of terms is four, as shown in Eqs. (4.12)–(4.14). Figures 4.3(c) and (d) present the number of total terms varying with the hyperparameter α obtained by *Rheo*-SINDy using the training data (a) and (b), respectively (for the detail of the hyperparameter α, see 4.A). 4.3(c) indicates that the sparse solutions can be obtained by the STLSQ, STRidge, and a-Lasso, but not by the Lasso and E-Net. Moreover, from the perspective of the number of terms, the STLSQ and STRdge exhibit similar behavior. Specifically, we confirm that the correct *number* of terms (cf. Eqs. (4.12)–(4.14)) are obtained by the STLSQ and STRidge with $3 \times 10^{-3} \leq \alpha \leq 3 \times 10^{-1}$. On the other hand, Fig. 4.3(d) indicates that the STLSQ, STRidge, and a-Lasso yielded the correct number of terms, though all four methods gave sparse solutions. In most of the cases where the number of terms obtained was correct, the obtained coefficients were also correct. These results suggest that the oscillatory shear test is more appropriate than the simple shear test to obtain the correct constitutive equations for the UCM model. Figure 4.3(e) lists the constitutive equations obtained by the STRidge and a-Lasso. We can see that the STRidge and a-Lasso can give the collect constitutive equations, except for the a-Lasso in the simple shear test. Furthermore, we confirmed that the correct equations were obtained even for α values not shown in Fig. 4.3(e) in the case of the UCM model. These findings show the basic validity of finding the constitutive equations from the rheological data by *Rheo*-SINDy. Figure 4.3 indicates that the Lasso and E-Net could not identify the correct solution within the considered scope; thus, we exclude these two methods from consideration in the following discussion.

4.4.2 Re-Identifying Giesekus Model

We here explain the results of *Rheo*-SINDy for the Giesekus model. This case used the polynomial library consisting of up to 2nd order terms of τ_{xx}, τ_{yy}, τ_{xy}, and κ_{xy}. Figure 4.4 shows (a) the total number of terms and (b) the error rate obtained by *Rheo*-SINDy for the training data of the Giesekus model. The error rate is defined as the sum of the mean squared errors (MSEs) of $\dot{\boldsymbol{t}}_{\mu\nu} - \boldsymbol{\Theta}\hat{\boldsymbol{\xi}}_{\mu\nu}$. The MSEs were scaled so that the maximum value of each method was 1. We here show results using a single data trajectory with $\omega = 0.1$ and multiple data trajectories with $\omega \in \{0.1, 0.2, \ldots, 1.0\}$ as training data. Figure 4.4(a) indicates that the a-Lasso evidently provides a sparser solution compared to the other two methods. Furthermore, Fig. 4.4(b) demonstrates that the methods using multiple data trajectories derive solutions with smaller errors than those using a single data trajectory. We note that, similar to the number of terms obtained by *Rheo*-SINDy, coefficient values generally depend on α.

Figures 4.5(a) and (b) show the constitutive equations found by *Rheo*-SINDy and the test simulation

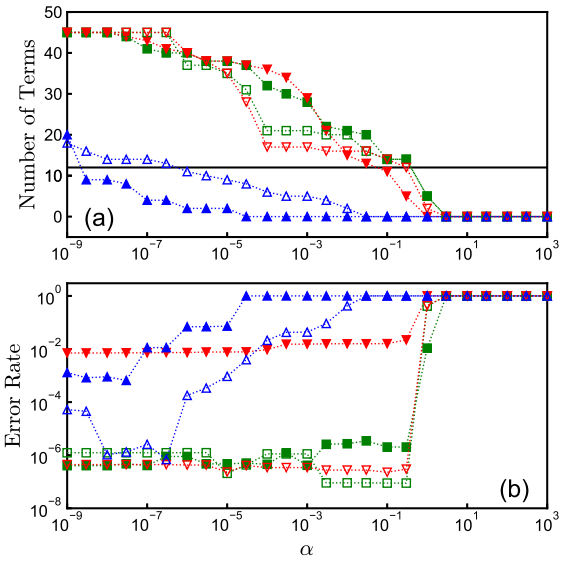

Fig. 4.4 (a) The number of total terms and (b) the error rate obtained for the Giesekus model. The optimization methods include the STLSQ (green squares), STRidge (red reverse triangles), and a-Lasso (blue triangles). The filled and open symbols indicate the results with a single data trajectory of $\kappa_{xy} = \gamma_0 \omega \cos(\omega t)$ with $\gamma_0 = 2$ and $\omega = 0.1$ for $0 \leq t \leq 100$ and those with multiple (10) data trajectories of $\kappa_{xy} = \gamma_0 \omega \cos(\omega t)$ with $\gamma_0 = 2$ and $\omega \in \{0.1, 0.2, \ldots, 1\}$ for $0 \leq t \leq 100$, respectively.

results, respectively. Here, we used the training data of the multiple data trajectories. The α value for each method was chosen considering the sparsity indicated in Fig. 4.4(a) and the small loss indicated in Fig. 4.4(b). For test simulations shown in Fig. 4.5(b), we employed the oscillatory shear flow with $\gamma_0 = 4$ and $\omega = 0.5$, which is the outside of the parameters in the training data described in Sec. 4.3.1. Figure 4.5(a) reveals that the STRidge with $\alpha = 3 \times 10^{-1}$ can give almost exact constitutive equations, including the value of α_{G} (cf. Eqs. (4.16)–(4.19)). As inferred from this, the predictions based on the constitutive equations obtained by the STRidge demonstrate a good agreement with the test data as shown in Fig. 4.5(b-ii). While the success of the STRidge, the STLSQ and a-Lasso failed to identify the correct solution, as indicated in Fig. 4.5(a). The constitutive equation obtained by the STLSQ with $\alpha = 3 \times 10^{-1}$ has a low error rate as shown in Fig. 4.4(b), but its predicted τ_{xx} significantly deviates from the test data as seen in Fig. 4.5(b-i). On the other hand, although the a-Lasso did not provide the correct solution for τ_{xx}, the test simulations with the obtained constitutive equations exhibit a good agreement with the test data. These test simulations demonstrate that the STRidge and a-Lasso are promising approaches for *Rheo*-SINDy.

4.4.3 Re-Identifying the Solution of Hookean Dumbbell Model

We next explain the results for the Hookean dumbbell model. We here used the polynomial library that includes up to 2nd order terms of τ_{xx}, τ_{yy}, τ_{xy}, and κ_{xy}. In what follows, based on the findings in Secs. 4.4.1 and 4.4.2, we consider only the STRidge and a-Lasso as optimization methods.

Figure 4.6 shows the *Rheo*-SINDy results for the Hookean dumbbell model with the different numbers

(a) SINDy results

method	α	equations
STLSQ	3×10^{-1}	$\dot{\tau}_{xx} = +1.404\tau_{xx} + 2.404\tau_{yy} - 0.500\tau_{xx}^2 + 2.405\tau_{xx}\tau_{yy} - 2.904\tau_{xy}^2 + 2.000\tau_{xy}\kappa_{xy}$ $\dot{\tau}_{yy} = -1.000\tau_{yy} - 0.500\tau_{yy}^2 - 0.500\tau_{xy}^2$ $\dot{\tau}_{xy} = -1.000\tau_{xy} + 1.000\kappa_{xy} - 0.500\tau_{xx}\tau_{xy} - 0.499\tau_{yy}\tau_{xy} + 1.000\tau_{yy}\kappa_{xy}$
STRdge	3×10^{-1}	$\dot{\tau}_{xx} = -1.001\tau_{xx} - 0.500\tau_{xx}^2 - 0.499\tau_{xy}^2 + 2.000\tau_{xy}\kappa_{xy}$ $\dot{\tau}_{yy} = -0.999\tau_{yy} - 0.496\tau_{yy}^2 - 0.500\tau_{xy}^2$ $\dot{\tau}_{xy} = -1.000\tau_{xy} + 1.000\kappa_{xy} - 0.500\tau_{xx}\tau_{xy} - 0.497\tau_{yy}\tau_{xy} + 0.998\tau_{yy}\kappa_{xy}$
a-Lasso	3×10^{-7}	$\dot{\tau}_{xx} = -1.498\tau_{xx} - 0.502\tau_{yy} - 0.495\tau_{xx}^2 - 0.475\tau_{xx}\tau_{yy} + 1.998\tau_{xy}\kappa_{xy}$ $\dot{\tau}_{yy} = -0.993\tau_{yy} - 0.472\tau_{yy}^2 - 0.500\tau_{xy}^2$ $\dot{\tau}_{xy} = -0.998\tau_{xy} + 0.999\kappa_{xy} - 0.499\tau_{xx}\tau_{xy} - 0.484\tau_{yy}\tau_{xy} + 0.995\tau_{yy}\kappa_{xy}$

(b) test simulations

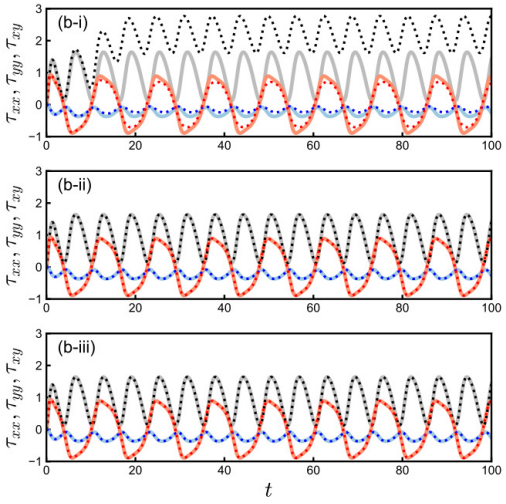

Fig. 4.5 (a) The obtained constitutive equations for three optimization methods and (b) test simulation results under the oscillatory shear flow with $\gamma_0 = 4$ and $\omega = 0.5$ for (i) the STLSQ, (ii) STRidge, (iii) and a-Lasso. The training data are the same as those in Fig. 4.4. In (a), the constitutive equations obtained by the multiple data trajectories are shown. In (b), the xx-, yy-, and xy-components of the stress tensor are shown with black, blue, and red lines, respectively. The dotted and solid lines in (b) denote the predictions by the equations shown in (a) and the test simulation data, respectively.

of dumbbells. We note that the standard deviation of $\boldsymbol{\tau}$ decreases proportionally with $N_\mathrm{p}^{-1/2}$. From Fig. 4.6(a), as the value of N_p increases, sparser solutions are obtained. Unlike the case of the UCM model (cf. Fig. 4.3), which can be considered as the "noise-free" case of the Hookean dumbbell model, the STRidge provides the correct number of terms only within a narrow range of α values. Nevertheless, if we choose the appropriate α value, the (nearly) correct constitutive equations can be found by the STRidge, as shown in the upper part of Fig. 4.6(b). We note that the terms containing τ_{yy} appear in the time evolution equation for τ_{xy} obtained by the STRidge. Although these terms do not affect the predictions because $\dot{\tau}_{yy} = 0$, these terms do not appear in the correct equation. We speculate that the appearance of these terms is due to the correlation effects of the noise in x and y on the stress (cf. Eq. (4.24)). When comparing the STRidge and a-Lasso, it is evident that the a-Lasso provides stable and sparse solutions across a broader range of α values, regardless of the N_p value. Furthermore, we confirm that the correct equations can be obtained using the a-Lasso from the lower part of Fig. 4.6(b). This partially suggests the effectiveness of the a-Lasso in discovering essential terms from noisy data.

4.4.4 Re-Identifying the Solution of FENE-P Dumbbell Model

We examine whether *Rheo*-SINDy can find more complex differential equations (i.e., the FENE-P dumbbell model) than the UCM model and the Giesekus model. For the *Rheo*-SINDy regressions of the differential equation for the conformation tensor of the FENE-P dumbbell model explained in Sec. 4.3.2,

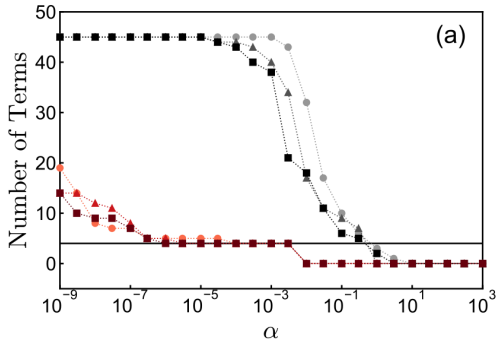

(b)

method	α	N_p	equations
STRidge	3×10^{-1}	10^3	$\dot{\tau}_{xx} = -0.994\tau_{xx} + 1.999\tau_{xy}\kappa_{xy}$ $\dot{\tau}_{yy} = 0.000$ $\dot{\tau}_{xy} = -0.992\tau_{xy} + 0.995\kappa_{xy} + 0.559\tau_{yy}\tau_{xy} + 1.007\tau_{yy}\kappa_{xy}$
STRidge	3×10^{-1}	10^5	$\dot{\tau}_{xx} = -1.001\tau_{xx} + 2.002\tau_{xy}\kappa_{xy}$ $\dot{\tau}_{yy} = 0.000$ $\dot{\tau}_{xy} = -1.001\tau_{xy} + 1.000\kappa_{xy} + 0.387\tau_{yy}\kappa_{xy}$
a-Lasso	3×10^{-4}	10^3	$\dot{\tau}_{xx} = -0.993\tau_{xx} + 1.998\tau_{xy}\kappa_{xy}$ $\dot{\tau}_{yy} = 0.000$ $\dot{\tau}_{xy} = -0.991\tau_{xy} + 0.987\kappa_{xy}$
a-Lasso	1×10^{-6}	10^5	$\dot{\tau}_{xx} = -1.001\tau_{xx} + 2.002\tau_{xy}\kappa_{xy}$ $\dot{\tau}_{yy} = 0.000$ $\dot{\tau}_{xy} = -1.001\tau_{xy} + 1.000\kappa_{xy}$

Fig. 4.6 (a) The number of total terms obtained by the STRidge (black) and a-Lasso (red) for the training data generated by the Hookean dumbbell model, and (b) the obtained constitutive equations. Here, the *Rheo*-SINDy regressions were conducted for the multiple data trajectories. In (a), circle, triangle, and square symbols indicate the total numbers of terms obtained by the data for $N_\mathrm{p} = 10^3$, 10^4, and 10^5, respectively.

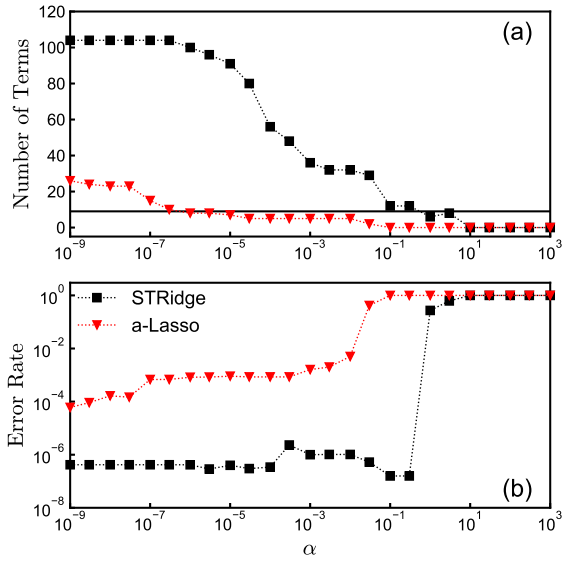

Fig. 4.7 (a) The total number of terms and (b) the error rate for the conformation tensor $\boldsymbol{C}$ of the FENE-P dumbbell model obtained by *Rheo*-SINDy with the STRidge (black squares) and a-Lasso (red reverse triangles). The horizontal line in (a) indicates the correct number of terms. The training data were generated by Eqs. (4.30)–(4.32) with $n_\mathrm{K} = 10$.

we prepare the following library:

$$\boldsymbol{\Theta} = \begin{bmatrix} \mathbf{1} & \boldsymbol{C}_\mathrm{s}(t_1) & \kappa_{xy}(t_1) & f_\mathrm{FENE}(t_1)\boldsymbol{C}_\mathrm{s}(t_1) & f_\mathrm{FENE}(t_1)\kappa_{xy}(t_1) \\ \mathbf{1} & \boldsymbol{C}_\mathrm{s}(t_2) & \kappa_{xy}(t_2) & f_\mathrm{FENE}(t_2)\boldsymbol{C}_\mathrm{s}(t_2) & f_\mathrm{FENE}(t_2)\kappa_{xy}(t_2) \\ \vdots & \vdots & \vdots & \vdots & \vdots \\ \mathbf{1} & \boldsymbol{C}_\mathrm{s}(t_n) & \kappa_{xy}(t_n) & f_\mathrm{FENE}(t_n)\boldsymbol{C}_\mathrm{s}(t_n) & f_\mathrm{FENE}(t_n)\kappa_{xy}(t_n) \end{bmatrix}, \tag{4.38}$$

method	α	equations
STRidge	1×10^{-3}	$\dot{C}_{xx} = +0.410 + 0.078C_{xx} + 0.495(C_{yy} + C_{zz}) - 0.011C_{xx}(C_{yy} + C_{zz}) - 0.092C_{yy}(C_{yy} + C_{zz} + C_{xy}) + 2.000C_{xy}\kappa_{xy} - 1.038f_{\mathrm{FENE}}C_{xx} + 0.418f_{\mathrm{FENE}}(C_{yy} + C_{zz})$ $\dot{C}_{yy} = +0.970 + 0.573(C_{yy} + C_{zz}) - 0.003C_{xx}C_{yy} - 0.002C_{xx}C_{zz} - 0.080C_{yy}(C_{yy} + C_{zz} + C_{xy}) - 0.312f_{\mathrm{FENE}}(C_{yy} + C_{zz})$ $\dot{C}_{zz} = \dot{C}_{yy}$ $\dot{C}_{xy} = +0.500(C_{yy} + C_{zz})\kappa_{xy} - 1.000f_{\mathrm{FENE}}C_{xy}$
STRidge	1×10^{-1}	$\dot{C}_{xx} = +3.333 + 2.000C_{xy}\kappa_{xy} - 1.000f_{\mathrm{FENE}}C_{xx}$ $\dot{C}_{yy} = +3.326 - 0.499f_{\mathrm{FENE}}(C_{yy} + C_{zz})$ $\dot{C}_{zz} = \dot{C}_{yy}$ $\dot{C}_{xy} = +0.500(C_{yy} + C_{zz})\kappa_{xy} - 1.000f_{\mathrm{FENE}}C_{xy}$
a-Lasso	1×10^{-7}	$\dot{C}_{xx} = -0.208C_{xx} + 0.436C_{yy} - 0.042C_{xx}C_{yy} + 1.946C_{xy}\kappa_{xy} + 0.072\kappa_{xy}^2 - 0.683f_{\mathrm{FENE}}C_{xx} + 0.683f_{\mathrm{FENE}}C_{yy}$ $\dot{C}_{yy} = 0.000$ $\dot{C}_{zz} = \dot{C}_{yy}$ $\dot{C}_{xy} = +1.101\kappa_{xy} - 0.017C_{xx}C_{xy} - 0.086C_{yy}C_{xy} + 0.314C_{yy}\kappa_{xy} - 0.107C_{zz}C_{xy} + 0.210C_{zz}\kappa_{xy} - 0.289f_{\mathrm{FENE}}C_{xy} + 0.424f_{\mathrm{FENE}}\kappa_{xy}$
a-Lasso	1×10^{-4}	$\dot{C}_{xx} = +1.977C_{xy}\kappa_{xy} - 0.998f_{\mathrm{FENE}}C_{xx} + 1.007f_{\mathrm{FENE}}C_{yy}$ $\dot{C}_{yy} = 0.000$ $\dot{C}_{zz} = \dot{C}_{yy}$ $\dot{C}_{xy} = +3.219\kappa_{xy} - 1.005f_{\mathrm{FENE}}C_{xy}$

Fig. 4.8 The differential equations for the conformation tensor $\boldsymbol{C}$ of the FENE-P dumbbell model found by *Rheo*-SINDy.

where $\boldsymbol{C}_{\mathrm{s}}$ includes non-zero components of the conformation tensor under shear flow, namely, C_{xx}, C_{yy}, C_{zz}, and C_{xy}. The total number of library functions is thus $N_{\boldsymbol{\Theta}} = 26$.

Figure 4.7 indicates (a) the total number of predicted terms and (b) the error rate as a function of the hyperparameter α for the STRidge and the a-Lasso. Similar to the results in Figs. 4.3 and 4.4, the a-Lasso provides sparser solutions than the STRidge, and the STRidge gives lower error rates than the a-Lasso. Figure 4.8 presents the differential equations obtained by the STRidge and a-Lasso for particular α values that yield a small error and/or a small number of terms. From the lower part of Fig. 4.8, while the a-Lasso can provide sparser solutions, it does not guarantee that these are correct (cf. Eqs. (4.30)–(4.32)). Specifically, in all cases for τ_{xx}, τ_{yy}, and τ_{zz}, the a-Lasso has failed to identify the constant term in Eqs. (4.30) and (4.31), which is a possible source of larger errors compared to the STRidge. On the other hand, in the case of the STRidge, we confirmed that by choosing the appropriate α ($\alpha = 1 \times 10^{-1}$), nearly correct differential equations can be obtained, as shown in the upper part of Fig. 4.8. Since the yy-component and zz-component of the stress are equivalent, the exact equations can be recovered by setting $C_{yy} = C_{zz}$. Thus, we found that the correct differential equations for the FENE-P dumbbell model can be obtained if we can prepare the proper library functions and choose the appropriate value of the hyperparameter. Figure 4.9 shows the test simulation results using the identified differential equations for $\boldsymbol{C}$ in Fig. 4.8 and the dimensionless form of Eq. (4.29). Here, the oscillatory shear flow with $\gamma_0 = 4$ and $\omega = 1$ was considered. From Fig. 4.9, the equations obtained by the STRidge can reproduce the exact solutions even when the equations are not exactly correct ($\alpha = 1 \times 10^{-3}$). On the other hand, the test simulations with the differential equations obtained by the a-Lasso show the deviations from the test data, especially for τ_{xx}. These results emphasize the need to choose an appropriate optimization method to obtain reasonable solutions.

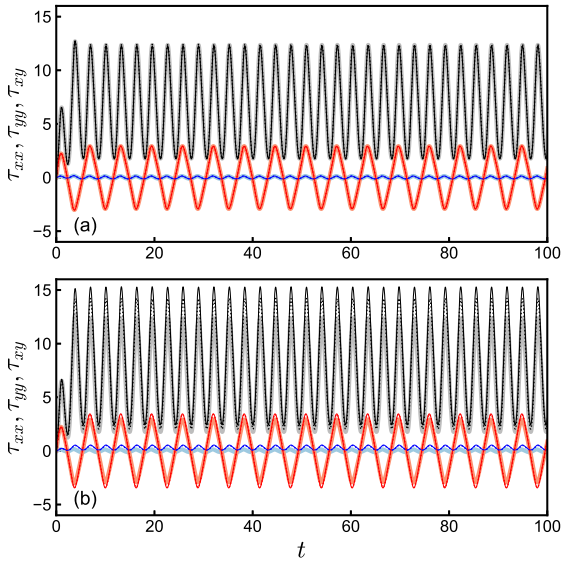

Fig. 4.9 The test simulation results using the equations obtained by (a) the STRidge and (b) a-Lasso. Here, the test simulations were conducted with $\gamma_0 = 4$ and $\omega = 1$. The black, blue, and red lines show τ_{xx}, τ_{yy}, and τ_{xy}. The bold, thin dotted, and thin solid lines indicate the exact solutions, predictions with smaller α values ($\alpha = 1 \times 10^{-3}$ for the STRidge and $\alpha = 1 \times 10^{-7}$ for the a-Lasso), and predictions with larger α values ($\alpha = 1 \times 10^{-1}$ for the STRidge and $\alpha = 1 \times 10^{-4}$ for the a-Lasso).

We then examine whether the stress expression of the constitutive equation for the FENE-P dumbbell model (cf. Eqs. (4.35)–(4.37)) can be found by *Rheo*-SINDy. For such a purpose, we prepared the following custom library:

$$\boldsymbol{\Theta} = \begin{bmatrix} 1 & \{\mathrm{tr}\{\boldsymbol{\tau}\}(t_1)\}^p \boldsymbol{T}_\mathrm{s}(t_1) & \{\mathrm{tr}\{\boldsymbol{\tau}\}(t_1)\}^2 & \{\boldsymbol{T}_\mathrm{s}(t_1)\}^p \kappa_{xy}(t_1) \\ 1 & \{\mathrm{tr}\{\boldsymbol{\tau}\}(t_2)\}^p \boldsymbol{T}_\mathrm{s}(t_2) & \{\mathrm{tr}\{\boldsymbol{\tau}\}(t_2)\}^2 & \{\boldsymbol{T}_\mathrm{s}(t_2)\}^p \kappa_{xy}(t_2) \\ \vdots & \vdots & \vdots & \vdots \\ 1 & \{\mathrm{tr}\{\boldsymbol{\tau}\}(t_n)\}^p \boldsymbol{T}_\mathrm{s}(t_n) & \{\mathrm{tr}\{\boldsymbol{\tau}\}(t_n)\}^2 & \{\boldsymbol{T}_\mathrm{s}(t_n)\}^p \kappa_{xy}(t_n) \end{bmatrix}, \tag{4.39}$$

where $\boldsymbol{T}_\mathrm{s}$ includes $\{\tau_{xx}, \tau_{yy}, \tau_{zz}, \tau_{xy}\}$ and p $(= 0, 1, 2)$ is the polynomial order. Thus, the total number of library functions is $N_{\boldsymbol{\Theta}} = 29$. We prepared the library that includes at least the terms present in Eqs. (4.35)–(4.37). Furthermore, we excluded terms that could potentially become large, such as higher-order terms involving κ_{xy}. When such terms are included in the solutions, the differential equations may be unstable, and in worse cases, they may also diverge.

Figure 4.10 shows (a) the total number of terms and (b) the error rate obtained by *Rheo*-SINDy with the STRidge and a-Lasso. Similar to what we noted previously, the a-Lasso can yield sparser solutions than the STRidge. Based on the number of terms shown in Fig. 4.10(a) and the error rates shown in Fig. 4.10(b), we chose several α values with a small number of terms and a low error rate. Figure 4.11 presents the equations obtained using the selected α. From Fig. 4.11, the equations predicted by the STRidge with $\alpha = 1$ and the a-Lasso with $\alpha = 1 \times 10^{-4}$ are almost the same; conversely, the solutions for small α values significantly differ between the two methods. For the STRidge with $\alpha = 1 \times 10^{-2}$, the identified equations are close to the correct equations (cf. Eqs. (4.35)–(4.37)). Furthermore, the coefficient values

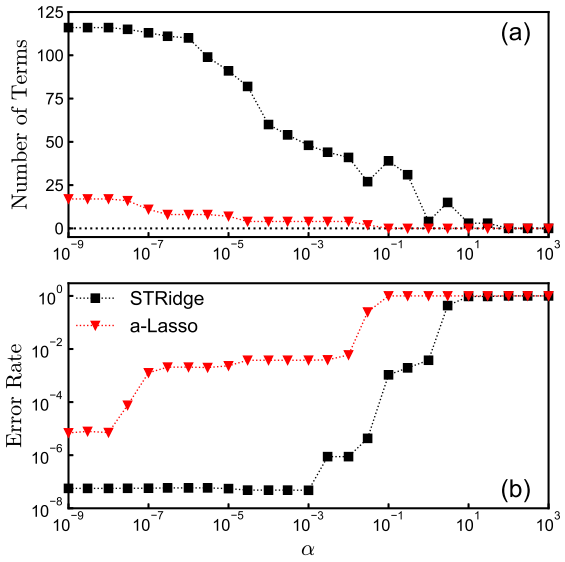

Fig. 4.10 (a) The total number of terms and (b) the error rate for the FENE-P dumbbell model obtained by the STRidge (black squares) and the a-Lasso (red reverse triangles). The horizontal short-dashed line in (a) indicates that the number of terms is zero.

Table 4.1 The mean squared error (MSE) between predicted and exact solutions for the FENE-P dumbbell model.

method	α	MSE(τ_{xx})	MSE(τ_{yy})	MSE(τ_{xy})
STRidge	1×10^{-2}	1.1×10^{-1}	5.0×10^{-5}	5.1×10^{-3}
STRidge	1	2.3	8.2×10^{-3}	8.9×10^{-2}
a-Lasso	3×10^{-8}	3.4×10^{-1}	3.0×10^{-3}	3.8×10^{-2}
a-Lasso	1×10^{-4}	2.3	8.2×10^{-3}	9.0×10^{-2}

for the correctly obtained terms are close to the correct values. For the a-Lasso with $\alpha = 3 \times 10^{-8}$, several coefficients for the correctly obtained terms, such as τ_{xx}, τ_{xy}, and $\tau_{xx}\tau_{xy}\kappa_{xy}$ in the equation for $\dot{\tau}_{xx}$, are close to the exact values, but for other several terms, such as $\mathrm{tr}\,\boldsymbol{\tau}\tau_{xx}$ in the equation for $\dot{\tau}_{xx}$, the correct coefficient values are not obtained. Nevertheless, from Fig. 4.12, which shows the test simulation results, the equations obtained by the STRidge with $\alpha = 1 \times 10^{-2}$ and the a-Lasso with $\alpha = 3 \times 10^{-8}$ can well reproduce the exact solutions including the small oscillation of τ_{yy}. Although the results for the STRidge and a-Lasso appear to be little difference, the difference in predictions is quantified by their MSEs shown in Table 4.1. When α is small, the error in τ_{xx} is of the same order for both methods, but for predictions of τ_{yy} and τ_{xy}, the STRidge outperforms the a-Lasso. The STRidge, however, provides a sparse solution within a narrow range of α values, requiring careful selection of α.

4.4.5 Finding an Approximate Equation of FENE Dumbbell Model

Finally, we address the FENE dumbbell model. As explained in Sec. 4.3.2, the FENE dumbbell model does not have an analytical expression of the constitutive equation. Thus, we here develop an "approximate" constitutive equation using *Rheo*-SINDy.

method	α	equations
STRidge	1×10^{-2}	$\dot{\tau}_{xx} = -1.033\tau_{xx} - 0.032(\tau_{yy} + \tau_{zz}) - 0.076\mathrm{tr}\boldsymbol{\tau}\tau_{xx} + 0.039\mathrm{tr}\boldsymbol{\tau}(\tau_{yy} + \tau_{zz}) + 2.071\tau_{xy}\kappa_{xy}$ $- 0.031(\mathrm{tr}\boldsymbol{\tau})^2(\tau_{yy} + \tau_{zz}) + 0.076\tau_{xx}\tau_{xy}\kappa_{xy}$ $\dot{\tau}_{yy} = -0.037\tau_{xx} - 0.533(\tau_{yy} + \tau_{zz}) + 0.019\mathrm{tr}\boldsymbol{\tau}\tau_{xx} - 0.020\mathrm{tr}\boldsymbol{\tau}(\tau_{yy} + \tau_{zz}) + 0.074\tau_{xy}\kappa_{xy}$ $- 0.020(\mathrm{tr}\boldsymbol{\tau})^2 + 0.037(\tau_{yy} + \tau_{zz})\tau_{xy}\kappa_{xy}$ $\dot{\tau}_{zz} = \dot{\tau}_{yy}$ $\dot{\tau}_{xy} = -0.997\tau_{xy} + 0.999\kappa_{xy} - 0.075\mathrm{tr}\boldsymbol{\tau}\tau_{xy} + 0.506(\tau_{yy} + \tau_{zz})\kappa_{xy}$ $- 0.019\tau_{xx}(\tau_{yy} + \tau_{zz})\kappa_{xy} + 0.048(\tau_{yy}^2 + +\tau_{yy}\tau_{zz} + \tau_{zz}^2)\kappa_{xy} + 0.076\tau_{xy}^2\kappa_{xy}$
STRidge	1	$\dot{\tau}_{xx} = -1.173\tau_{xx} + 2.185\tau_{xy}\kappa_{xy}$ $\dot{\tau}_{yy} = 0.000$ $\dot{\tau}_{zz} = \dot{\tau}_{yy}$ $\dot{\tau}_{xy} = -1.071\tau_{xy} + 1.033\kappa_{xy}$
a-Lasso	3×10^{-8}	$\dot{\tau}_{xx} = -1.024\tau_{xx} + 0.424\mathrm{tr}\boldsymbol{\tau}\tau_{xx} + 1.133\mathrm{tr}\boldsymbol{\tau}\tau_{yy} + 2.067\tau_{xy}\kappa_{xy} - 0.504(\mathrm{tr}\boldsymbol{\tau})^2 + 0.075\tau_{xx}\tau_{xy}\kappa_{xy}$ $\dot{\tau}_{yy} = -0.038\tau_{xx} - 1.155\tau_{yy} + 0.073\tau_{xy}\kappa_{xy}$ $\dot{\tau}_{zz} = \dot{\tau}_{yy}$ $\dot{\tau}_{xy} = -1.043\tau_{xy} + 1.047\kappa_{xy} - 0.046\mathrm{tr}\boldsymbol{\tau}\tau_{xy} + 2.489\tau_{yy}\kappa_{xy}$
a-Lasso	1×10^{-4}	$\dot{\tau}_{xx} = -1.173\tau_{xx} + 2.185\tau_{xy}\kappa_{xy}$ $\dot{\tau}_{yy} = 0.000$ $\dot{\tau}_{zz} = \dot{\tau}_{yy}$ $\dot{\tau}_{xy} = -1.070\tau_{xy} + 1.032\kappa_{xy}$

Fig. 4.11 The constitutive equations for the FENE-P dumbbell model obtained by the STRidge and a-Lasso.

To obtain dynamical equations by *Rheo*-SINDy, one first needs to design an appropriate library $\boldsymbol{\Theta}$. To prepare $\boldsymbol{\Theta}$ for the FENE dumbbell model, we utilize the physical insights obtained from the analytical expression of the FENE-P dumbbell model. We here assume the constitutive equation of the FENE-P dumbbell model is *similar* to that of the FENE dumbbell model. Since the FENE-P dumbbell model is a simplified version of the FENE dumbbell model, we believe that this is a reasonable assumption. Here, we note that the stress expression shown in Eq. (4.29) is no longer applicable to the FENE dumbbell model. Thus, it is invalid to obtain stress through the conformation tensor $\boldsymbol{C}$, as in the FENE-P dumbbell model. Based on the above considerations, we decided to use the custom library presented in Eq. (4.39), which was also used in the FENE-P dumbbell model.

Figure 4.13(a) compares the total number of terms predicted by the STRidge and a-Lasso. Similar to the previous discussions, we can obtain sparse solutions over a wide range of α values with the a-Lasso, whereas the STRidge gives sparse solutions only within a limited range of α. The left table in Fig. 4.14 shows the equations obtained by the a-Lasso with two α chosen from the viewpoints of the sparsity and error rate. We note that the predictions obtained by the STRidge are inferior to those obtained by the a-Lasso shown in Fig. 4.14, which is discussed in 4.D. From the left table in Fig. 4.14, if α is appropriately chosen, the a-Lasso can give sparse equations with coefficients of reasonable (not excessively large) magnitudes. Comparing the equations for the FENE-P model obtained by the a-Lasso with $\alpha = 3 \times 10^{-8}$ (Fig. 4.11) and those for the FENE model obtained by the a-Lasso with $\alpha = 1 \times 10^{-6}$ (Fig. 4.14), the appearing terms are almost identical, which demonstrates the similarity between these models. The difference in the coefficients thus represents the difference between these models. The right panels in Fig. 4.14 show the test simulation results obtained by the equations shown in the left table. We found that the equations obtained with $\alpha = 1 \times 10^{-6}$ can reproduce the BD simulation results outside the range of the training data well within the investigated parameters, including the oscillatory behavior

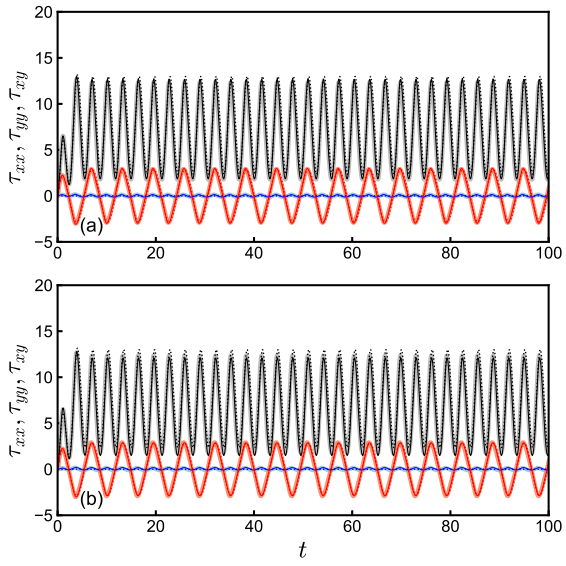

Fig. 4.12 Test simulation results for the constitutive equations of the FENE-P dumbbell model obtained by (a) the STRidge and (b) a-Lasso. The black, blue, and red lines represent the xx-, yy-, and xy-components of the stress tensor, respectively. The bold lines show the exact solutions. The thin solid and short-dashed lines indicate the results with smaller α values ($\alpha = 1 \times 10^{-2}$ for the STRidge and $\alpha = 3 \times 10^{-8}$ for the a-Lasso) and with larger α values ($\alpha = 1$ for the STRidge and $\alpha = 1 \times 10^{-4}$ for the a-Lasso).

of τ_{yy}. (With the large α ($\alpha = 3 \times 10^{-4}$), the identified equation for τ_{yy} becomes $\dot{\tau}_{yy} = 0$, which fails to reproduce the oscillatory behavior of τ_{yy}.) This success suggests that *Rheo*-SINDy with the a-Lasso is effective for discovering *unknown* constitutive equations. Nevertheless, we note that the equations presented in Fig. 4.14 may fail to predict test data significantly outside the range of the training data. Reproducing such highly nonlinear data would require the nonlinear terms dropped in Fig. 4.14. In this sense, the constitutive equations for the FENE dumbbell model obtained here are appropriately referred to as the "approximate" constitutive equations.

Thanks to the equations obtained using *Rheo*-SINDy, it is possible to provide a physical interpretation with the assistance of rheological knowledge. For example, from the comparison of the equations obtained for the FENE-P dumbbell model (cf. Fig. 4.11) and those for the FENE dumbbell model (cf. Fig. 4.14), the equations for larger α value ($\alpha = 1 \times 10^{-4}$ for the FENE-P dumbbell model and $\alpha = 3 \times 10^{-4}$ for the FENE dumbbell model) are similar except for the coefficient values. Furthermore, the terms in these equations are the same as those for the UCM model (and thus the Hookean dumbbell model). This indicates that all of these models share the same origin based on the dumbbell model. The linear term of stress in the constitutive equation represents the relaxation of stress (see Eq. (4.11)). Since the relaxation time at equilibrium ($\lambda = \zeta/4k_{\mathrm{eq}}$) is taken as the unit time in this study, the coefficient of this term should be -1 at equilibrium (and thus for the UCM model, see Eqs. (4.12)–(4.14)). From Figs. 4.11 and 4.14, the coefficient of the linear term of stress is smaller than -1, which indicates $\lambda_{\mathrm{sf}} < \lambda_{\mathrm{eq}}$ with the subscript "sf" and "eq" standing for "shear flow" and "equiliblium", respectively. This indicates that under shear flow, the values of spring strength for the FENE-P and FENE dumbbell models become larger than h_{eq}, which implies the appearance of the FENE effects under flow. From this discussion, it

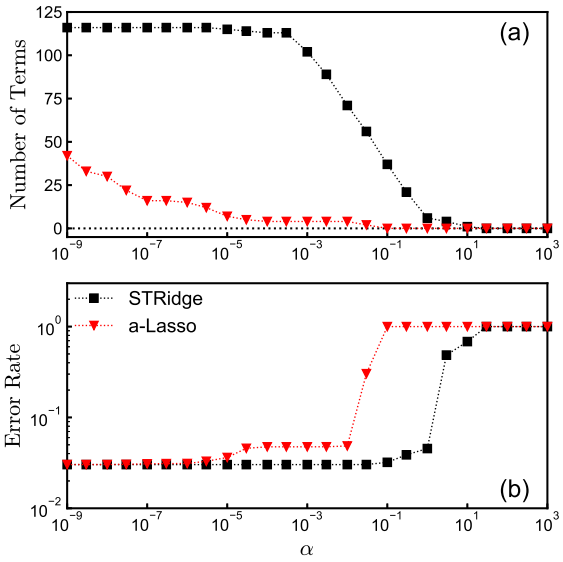

Fig. 4.13 (a) The total number of terms and (b) the error rate for the FENE dumbbell model predicted by the STRidge (black squares) and the a-Lasso (red reverse triangles). The horizontal short-dashed line in (a) indicates that the number of terms is zero.

α	equations
1×10^{-6}	$\dot{\tau}_{xx} = -1.265\tau_{xx} - 1.235\tau_{yy} + 0.583\mathrm{tr}\boldsymbol{\tau}\tau_{xx} + 1.208\mathrm{tr}\boldsymbol{\tau}\tau_{yy} + 2.279\tau_{xy}\kappa_{xy} - 0.714(\mathrm{tr}\boldsymbol{\tau})^2 + 0.822\tau_{yy}\tau_{xy}\kappa_{xy}$ $\dot{\tau}_{yy} = -0.110\tau_{xx} - 1.411\tau_{yy} - 0.990\tau_{zz} + 0.165\tau_{xy}\kappa_{xy}$ $\dot{\tau}_{zz} = 0.000$ $\dot{\tau}_{xy} = -1.208\tau_{xy} + 1.140\kappa_{xy} - 0.102\mathrm{tr}\boldsymbol{\tau}\tau_{xy} + 2.290\tau_{yy}\kappa_{xy}$
3×10^{-4}	$\dot{\tau}_{xx} = -1.477\tau_{xx} + 2.232\tau_{xy}\kappa_{xy}$ $\dot{\tau}_{yy} = 0.000$ $\dot{\tau}_{zz} = \dot{\tau}_{yy}$ $\dot{\tau}_{xy} = -1.320\tau_{xy} + 1.158\kappa_{xy}$

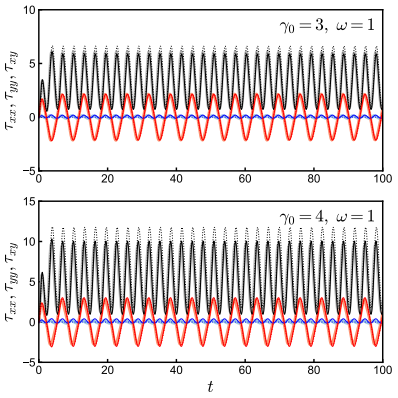

Fig. 4.14 The predicted constitutive equations for the FENE dumbbell model (left) and the test simulation results (right). Here, the a-Lasso was utilized to obtain the approximate constitutive equations. For test simulations, we solved the constitutive equations under the oscillatory shear flows with $\gamma_0 = 3$ and $\omega = 1$ (right upper panel) and $\gamma_0 = 4$ and $\omega = 1$ (right lower panel). The bold lines show the exact solutions, and the thin solid and short-dashed lines show the results with the smaller α value ($\alpha = 1 \times 10^{-6}$) and the larger α value ($\alpha = 3 \times 10^{-4}$).

is evident that *Rheo*-SINDy can provide physically interpretable constitutive equations.

4.5 Concluding Remarks

We tested that the sparse identification for nonlinear dynamics (SINDy) modified for nonlinear rheological data, which we call *Rheo*-SINDy, is effective in finding constitutive equations of complex fluids. We found

that *Rheo*-SINDy can successfully identify correct equations from training data generated from *known* constitutive equations, as well as provide approximate constitutive equations (or reduced order models) from training data generated by mesoscopic models when constitutive equations are analytically *unknown*.

Rheo-SINDy for two phenomenological constitutive equations (i.e., the upper convected Maxwell model and Giesekus model) revealed the following two things. First, compared to constant shear tests, oscillatory shear tests are appropriate for generating training data. Second, the sequentially thresholded Ridge regression (STRidge) and adaptive Lasso (a-Lasso) are effective in finding appropriate constitutive equations. We then examined the commonly used mesoscopic model, namely the dumbbell model with three different representations of spring strength: the Hookean, FENE-P, and FENE dumbbell models. Although the Hookean and FENE-P dumbbell models have analytical constitutive equations, for the FENE dumbbell model, there is no analytical expression of the constitutive equation. We confirmed through the Hookean dumbbell model that even in the presence of noise, the a-Lasso provides the correct solution over a wide range of the hyperparameter α. *Rheo*-SINDy was also effective in discovering the complex constitutive equations of the FENE-P dumbbell model. This case study revealed that the identification of complex equations requires the preparation of an appropriate custom library based on prior physical knowledge. Utilizing physical insights obtained from the Hookean and FENE-P dumbbell models, we attempted to find *approximate* constitutive equations for the FENE dumbbell model. We found that the a-Lasso can successfully give the approximate constitutive equations, which can be used in predictions beyond the range of the training data.

From our investigation, *Rheo*-SINDy with the STRidge or a-Lasso is effective for discovering constitutive equations from nonlinear rheological data. We found that the STRidge is generally superior in terms of retaining correct terms, while the a-Lasso is more robust to the selection of α than the STRidge. To obtain correct constitutive equations, in addition to selecting the appropriate optimization method, we are required to design an appropriate library by using physical insights, namely "domain knowledge." Designing such a proper library necessitates not only including necessary terms but also excluding unnecessary terms.

This research is expected to have an impact on fields such as rheology and fluid dynamics. From a rheological perspective, for several systems such as entangled polymers [85, 86] and wormlike micellar solutions [115, 116], sophisticated mesoscopic models suitable for numerical simulations under flow have been proposed. These mesoscopic models can generate reasonable training data not only under shear flow but also under extensional flow. Finding new approximate models from the data obtained by these mesoscopic simulations would be an interesting research subject. Furthermore, it would be desirable to conduct *Rheo*-SINDy for experimental data obtained by Large Amplitude Oscillatory Shear (LAOS) experiments [117]. Since the LAOS measurements do not provide all the major stress components under shear flow, exploring methods for discovering the constitutive equations from experimental data would be a future challenge. When approximate constitutive models are identified, those models can be employed for predictions of complex flows, which would deepen our understanding of complex fluids. We will continue our research in these directions.

4.A Sparse Regression Methods

To solve the optimization problem in Eq. (4.9), we used five sparse regression methods: (i) the sequentially thresholded least squares (STLSQ), (ii) sequentially thresholded Ridge regression (STRidge), (iii) least absolute shrinkage and selection operator (Lasso), (iv) Elastic-Net (E-Net), and (v) adaptive Lasso (a-

Table 4.2 The regularization term $R(\boldsymbol{\xi}_{\mu\nu})$ for the sparse regression methods.

Method	Regularization term $R(\boldsymbol{\xi}_{\mu\nu})$
STLSQ	$\lambda_0 \|\|\boldsymbol{\xi}_{\mu\nu}\|\|_0$
STRidge	$\lambda_0 \|\|\boldsymbol{\xi}_{\mu\nu}\|\|_0 + \lambda_2 \|\|\boldsymbol{\xi}_{\mu\nu}\|\|_2^2$
Lasso	$\lambda_1 \|\|\boldsymbol{\xi}_{\mu\nu}\|\|_1$
E-Net	$\lambda_1 \|\|\boldsymbol{\xi}_{\mu\nu}\|\|_1 + \lambda_2 \|\|\boldsymbol{\xi}_{\mu\nu}\|\|_2^2$
a-Lasso	$\lambda_1 \|\|\boldsymbol{\xi}'_{\mu\nu}\|\|_1$

Lasso).

The differences among these methods lie in the regularization term $R(\boldsymbol{\xi}_{\mu\nu})$ as shown in Table 4.2. The hyperparameters of ℓ_i norm ($i = 0, 1, 2$) are denoted as λ_i (> 0). The ℓ_0 and ℓ_1 norms are defined as

$$||\boldsymbol{\xi}_{\mu\nu}||_0 = \sum_j \delta(\xi_{\mu\nu,j}) \tag{4.40}$$

and

$$||\boldsymbol{\xi}_{\mu\nu}||_1 = \sum_j |\xi_{\mu\nu,j}|, \tag{4.41}$$

where $\delta(\xi_{\mu\nu,j})$ is the Kronecker delta function, which is equal to 1 if $\xi_{\mu\nu,j} \neq 0$ and 0 otherwise. The vector $\boldsymbol{\xi}'_{\mu\nu}$ in the a-Lasso is defined as $\boldsymbol{\xi}'_{\mu\nu} = \boldsymbol{\xi}_{\mu\nu} \otimes \boldsymbol{w}_{\mu\nu}$, where $\otimes$ is the element-wise product and $\boldsymbol{w}_{\mu\nu}$ is the adaptive weight vector and its j-th element is defined as $w_{\mu\nu,j} = |\xi_{\mu\nu,j}|^{-\delta}$ with δ being the positive constant.

The STLSQ and STRidge were implemented by iteratively conducting the least square regression and the Ridge regression, respectively, while setting the coefficients with smaller absolute values than a certain threshold α (> 0) to zero based on the original papers [43, 118]. In the STRidge, the hyperparameter λ_2 was set to 0.05. The Lasso, E-Net, and a-Lasso were implemented using the scikit-learn library [119]. In this library, the loss functions for the Lasso and E-Net are respectively defined as

$$\hat{\boldsymbol{\xi}}_{\mu\nu} = \underset{\boldsymbol{\xi}_{\mu\nu}}{\operatorname{argmin}} \frac{1}{2n} ||\dot{\boldsymbol{t}}_{\mu\nu} - \boldsymbol{\Theta}\boldsymbol{\xi}_{\mu\nu}||_2^2 + \alpha ||\boldsymbol{\xi}_{\mu\nu}||_1, \tag{4.42}$$

and

$$\hat{\boldsymbol{\xi}}_{\mu\nu} = \underset{\boldsymbol{\xi}_{\mu\nu}}{\operatorname{argmin}} \frac{1}{2n} ||\dot{\boldsymbol{t}}_{\mu\nu} - \boldsymbol{\Theta}\boldsymbol{\xi}_{\mu\nu}||_2^2 + \alpha\beta ||\boldsymbol{\xi}_{\mu\nu}||_1 + \frac{\alpha(1-\beta)}{2} ||\boldsymbol{\xi}_{\mu\nu}||_2^2, \tag{4.43}$$

where n is the number of data points, β is the ℓ_1 ratio, and α and β are the hyperparameters. The loss function for the Lasso is obtained by setting $\beta = 1$ in Eq. (4.43). In this study, β was set to 0.5 for the E-Net. According to the original paper of a-Lasso [120], the a-Lasso can be implemented as the Lasso problem as the following steps:

1. Define $\boldsymbol{\xi}'_{\mu\nu,j} = \boldsymbol{\xi}_{\mu\nu,j} / w_{\mu\nu,j}$, $j = 1, \ldots, J$.
2. Solve the Lasso problem for $\boldsymbol{\xi}'_{\mu\nu}$ using Eq. (4.42).
3. Output $\hat{\xi}_{\mu\nu,j} = \hat{\xi}'_{\mu\nu,j} / w_{\mu\nu,j}$, $j = 1, \ldots, J$.

The adaptive weight $w_{\mu\nu,j}$ depends on the coefficients, and thereby, the output coefficients can be varied in each iteration. To obtain the converged solution, we initialized the weights as unit vectors $\boldsymbol{w} = \boldsymbol{1}$ and repeated the above steps until the coefficients $\hat{\xi}_{\mu\nu,j}$ no longer change [110]. The hyperparameter δ was set to 3 (see 4.B for the effect of δ).

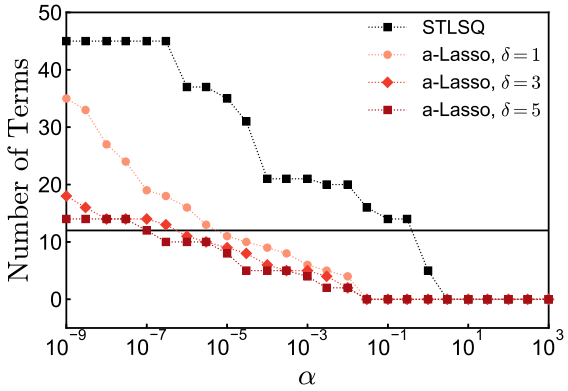

Fig. 4.15 The total number of terms obtained by the STLSQ (black symbols) and a-Lasso (red symbols) for the Giesekus model. Here, the circles, diamonds, and squares in the red series indicate the results with $\delta = 1$, 3, and 5 for the adaptive weight w_i, respectively.

4.B Hyperparameter of the Adaptive Lasso

Here, we shortly note the effect of changing the hyperparameter δ of the a-Lasso, which determines the adaptive weight. Figure 4.15 compares the total number of terms for the Giesekus model obtained by the a-Lasso with three different δ values. The training data include multiple trajectories, which are the same as those in Fig. 4.5. Here, the results for the STLSQ are also shown for comparison. As shown in Fig. 4.15, the solutions obtained by the a-Lasso with $\delta = 1$, 3, and 5 are sparser than those obtained by the STRidge. Nevertheless, due to the increased effects of weights, the solutions for $\delta = 3$ and 5 are sparser compared to the solutions for $\delta = 1$. Moreover, the results with $\delta = 3$ are almost the same as in the case of $\delta = 5$, although the a-Lasso with $\delta = 5$ provides slightly sparser solutions. Thus, the hyperparameter $\delta = 3$ can be considered sufficiently large to obtain sparse solutions. We note, in general, that a sparser solution is superior from the perspective of overfitting and helps prevent unexpected divergence during test simulations. From these discussions, in this study, we used $\delta = 3$ as the adaptive weight in the a-Lasso.

4.C Stress Expressions for the FENE-P Dumbbell Model

As noted in Sec. 4.3.2, the constitutive equation for the FENE-P dumbbell model can be expressed in terms of the stress (cf. Eqs. (4.35)–(4.37)). We here show the derivation of the constitutive equation for the FENE-P model [114].

To improve clarity, let us rewrite the stress $\boldsymbol{\tau}$ in Eq. (4.24) as follows:

$$\boldsymbol{\tau}(t) = \rho k_{\mathrm{eq}} Z_{\mathrm{eq}}^{-1} Z \langle \boldsymbol{R}(t)\boldsymbol{R}(t)\rangle - G\boldsymbol{I}, \tag{4.44}$$

where Z has already been defined in Eq. (4.34) and Z_{eq} indicates Z at equilibrium. In what follows, we express all variables in dimensionless forms by using the unit time λ and the unit stress $\rho k_{\mathrm{B}}T$. Additionally, for simplicity, we omit the tilde representing dimensionless quantities. Taking the trace of both sides of Eq. (4.44) and using the relation $\langle \boldsymbol{R}^2(t)\rangle = R_{\mathrm{max}}^2(1 - Z^{-1})$, we can rewrite Z as a function

of $\boldsymbol{\tau}$:

$$Z = 1 + \frac{1}{3n_{\mathrm{K}}Z_{\mathrm{eq}}^{-1}}(\mathrm{tr}\boldsymbol{\tau} + 3). \tag{4.45}$$

Taking the convected derivative of $\boldsymbol{\tau}/Z$, the time evolution of stress can be expressed as

$$\frac{\mathrm{d}\boldsymbol{\tau}}{\mathrm{d}t} - \boldsymbol{\tau}\cdot{}^{t}\boldsymbol{\kappa} - \boldsymbol{\kappa}\cdot\boldsymbol{\tau} = -Z_{\mathrm{eq}}^{-1}Z\boldsymbol{\tau} + 2\boldsymbol{D} + \frac{\mathrm{D}\ln Z}{\mathrm{D}t}(\boldsymbol{\tau} + \boldsymbol{I}), \tag{4.46}$$

which is the same as in Eq. (4.33). Since we do not address the spatial gradient in rheological calculations, $\mathrm{D}(\cdots)/\mathrm{D}t$ simply reduces $\mathrm{d}(\cdots)/\mathrm{d}t$. To obtain Eq. (4.46), we used the following relation that can be obtained by Eq. (4.28):

$$\frac{\mathrm{d}\boldsymbol{C}}{\mathrm{d}t} - \boldsymbol{C}\cdot{}^{t}\boldsymbol{\kappa} - \boldsymbol{\kappa}\cdot\boldsymbol{C} = -\frac{n_{\mathrm{K}}}{3}\boldsymbol{\tau}. \tag{4.47}$$

From Eq. (4.45), the time evolution of $\ln Z$ can be expressed in terms of $\mathrm{tr}\,\boldsymbol{\tau}$ as

$$\frac{\mathrm{d}}{\mathrm{d}t}\mathrm{tr}\boldsymbol{\tau} = \left\{3n_{\mathrm{K}}Z_{\mathrm{eq}}^{-1} + (\mathrm{tr}\boldsymbol{\tau} + 3)\right\}\frac{\mathrm{d}\ln Z}{\mathrm{d}t}. \tag{4.48}$$

Furthermore, taking trace of Eq. (4.46) and using Eq. (4.48), we can have

$$\frac{\mathrm{d}\ln Z}{\mathrm{d}t} = \frac{1}{3n_{\mathrm{K}}Z_{\mathrm{eq}}^{-1}}\left\{-Z_{\mathrm{eq}}^{-1}Z\mathrm{tr}\boldsymbol{\tau} + 2\mathrm{tr}\boldsymbol{D} + \mathrm{tr}\left(\boldsymbol{\tau}\cdot{}^{t}\boldsymbol{\kappa} + \boldsymbol{\kappa}\cdot\boldsymbol{\tau}\right)\right\}. \tag{4.49}$$

Combining Eqs. (4.46) and (4.49), we can express the time evolution of $\boldsymbol{\tau}$ (i.e., $\dot{\boldsymbol{\tau}}$) as a function of $\boldsymbol{\tau}$ and $\boldsymbol{\kappa}$. Specifically, Eqs. (4.46) and (4.49) reduce to Eqs. (4.35)–(4.37) under shear flow.

4.D STRidge Regressions for the FENE Dumbbell Model

Figures 4.16 and 4.17 show the test simulation results for the FENE dumbbell model using the approximate constitutive equations obtained by *Rheo*-SINDy with the STRidge. Here, in Fig. 4.16, we employed the custom library shown in Eq. (4.39) ($N_{\boldsymbol{\Theta}} = 29$), while in Fig. 4.17, we utilized a polynomial library including polynomial terms up to the third order of $\{\tau_{xx}, \tau_{yy}, \tau_{zz}, \tau_{xy}, \kappa_{xy}\}$ ($N_{\boldsymbol{\Theta}} = 56$). From the thin solid lines in Fig. 4.16, which show the results with the smaller $\alpha = 1 \times 10^{-1}$, while the magnitudes of the predicted stress components almost match the results of the BD simulation, spike-like predictions are occasionally observed. When using the third order polynomial library, the solutions for the small α, indicated by thin solid lines in Fig. 4.17, closely resemble the results of the BD simulations. This is likely attributed to the fact that the larger number of terms included in the library improves the predictive ability of the model. Nevertheless, we note that increasing the number of terms in the library without careful consideration does not necessarily lead to an improvement in the model performance. By increasing the number of terms in the library, overfitting issues may arise. For example, when *Rheo*-SINDy chooses terms that are likely to be significantly large under shear flow, such as $\tau_{xx}\kappa_{xy}^2$, there is an increased possibility that the differential equations may fail to be solved when conducting test simulations.

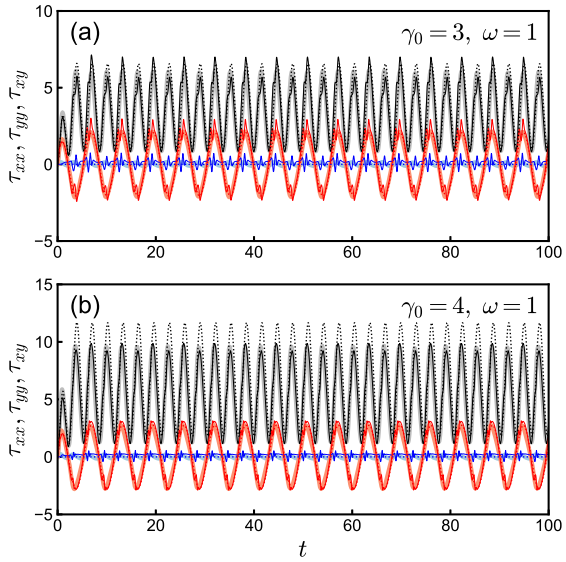

Fig. 4.16 Test simulation results obtained by *Rheo*-SINDy with the STRidge for the library shown in Eq. (4.39). The test simulations are conducted under the oscillatory shear flows with (a) $\gamma_0 = 3$ and $\omega = 1$ and (b) $\gamma_0 = 4$ and $\omega = 1$. The bold lines show the exact solutions, and the thin solid and short-dashed lines show the results with the smaller α value ($\alpha = 1 \times 10^{-1}$) and the larger α value ($\alpha = 1$).

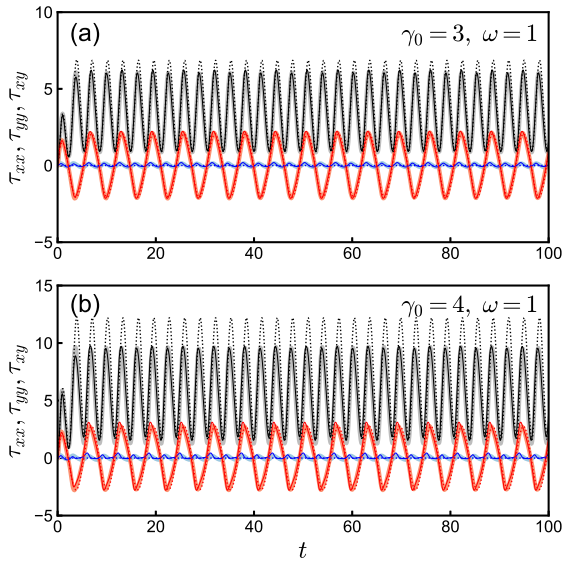

Fig. 4.17 Test simulation results obtained by the STRidge for the library including polynomial terms up to the third order of $\{\tau_{xx}, \tau_{yy}, \tau_{zz}, \tau_{xy}, \kappa_{xy}\}$. The flow parameters for the test simulations are the same as those in Fig. 4.16. The bold lines show the exact solutions, and the thin solid and short-dashed lines show the results with the smaller α value ($\alpha = 3 \times 10^{-2}$) and the larger α value ($\alpha = 1$).

Chapter 5

Nonlinear Rheology of Bidispersed Polymer Systems in Entangled States

5.1 Introduction

In this chapter, we extend a correction model based on mono-dispersed molecular weight systems for bi-dispersed and improve rheological predictions of microscopic models used in a future MLMSS. It has already been investigated that the sliplink model also used in Chapters 2 and 3 provide excellent predictions of rheological properties for entangled polymer melts under shear deformation and uniaxial extensional deformation On the other hand, recent experimental studies have revealed that under extremely high strain rate flow, strain softening occurs contrary to model predictions, and this is considered because of friction reduction by significant stretches and orientation of the polymer chains.

The rheological properties of a polymer melt in an entangled state attract much attention due to their importance in polymer processing. In typical industrial conditions, a polymer melt with molecular weight distribution is used to tune rheological properties [121]. Thus, it is essential to investigate the relation between the rheology and the compositions of the well-entangled polymeric system. For this purpose, bidisperse polymer blends have been extensively studied as a first step in understanding the rheology of polymer melts with arbitrary molecular weight distributions, as explained in detail below.

Experimental studies on the rheology of bidisperse polymer melts have been made for several decades [122–126]. Linear rheology involves not only the superposition of the rheology of monodispersed systems but also contributions from coupled dynamics [127]. The elongational viscosity has been measured by the Meissner-type rheometer by [123] and by the filament stretching rheometer by several groups [124, 126]. Among these studies, one of the interesting findings is that polymer blends containing a small amount of ultrahigh-molecular-weight polymers show significant strain hardenings under elongational flows [123]. [124] examined polystyrene blends and found that the maximum steady-state elongational viscosity became indistinguishable from three times the zero-shear viscosity calculated from linear viscoelasticity as the concentration of higher-molecular-weight chains increased in their examined samples. [126] classified the time regimes for the relaxations after cessation of elongational flow for the bidisperse system. The relaxations after cessation of the steady elongations exhibit the three regimes originating from the dynamics of short, long, or both short and long polymer chains. To predict the mechanical properties based on the coupled dynamics over the components, it is desirable to develop a coarse-grained model.

The theoretical and numerical models of polymers have rationalized the molecular-based mechanism

and reproduced the rheological properties by considering the coupled dynamics among the polymer chains. The models for entangled polymer melts are based on the bead-spring model and the tube model [6]. For entangled polymers, the pioneering model is the famous tube model. The important dynamics of the tube are reptation, the change in the tube length, and the release of entanglements. Based on the original tube model, sliplink models [20, 22, 23] and slip-spring model [107] were developed to numerically predict the rheological properties [128]. These models can quantitatively reproduce the rheological properties in the linear and near-linear response regimes. However, it is difficult to predict some phenomena under high deformation rate flows because of the lack of the mechanisms required to predict nonlinear rheology. For example, typical sliplink models cannot predict the decrease in the steady viscosities of entangled polymer melts with strain rates under uniaxial elongational flows [23].

For the unexplained rheological behavior under high deformation rate flows, friction reduction between a segment and the surrounding polymers induced by the stretched and oriented polymers (SORF mechanism) has been proposed [129]. For the rheology of entangled and unentangled polymer melts, some studies support that the SORF is important for accurate predictions of nonlinear rheology [130, 131]. For entangled systems, Masubuchi and coworkers extenisvely examined nonlinear rheological properties by the primitive chain network (PCN) model. After developing the PCN model with SORF for linear polystyrene [132], they examined the universality of SORF [133], and the associated predictions under biaxial elongational flows [134] and planar elongational flows [135]. Moreover, they investigated the applicability for pom-pom polymers [136] and for star polymers [137]. Subsequently, [85] studied the SORF by extending the sliplink model developed by [23]. Tests for unentangled polymer melts have also been reported with the dumbbell model [138] and the Rouse model [139]. While the SORF mechanism has been tested for monodispersed polymers, few studies have examined the effect of such a mechanism in bidisperse melts.

With the PCN model, the SORF expression has been tested for three bidisperse samples containing small amounts of the high-molecular-weight polymers [140]. [140] examined the SORF expression proposed by [132] with the PCN model. They found that the PCN model reproduces the rheology of the bidisperse well-entangled polystyrene melts reported by [124] and that the SORF mechanism explains the data under high-strain-rate elongational flows. In their results, at elongational strain rates below the inverse of the Rouse relaxation time of the long-chain component, suppressing the stretches of the long chains improves the rheological predictions. On the other hand, at elongational strain rates above that, the relaxations of the short chains suppress the SORF effects. Note that two models, namely, the slip-spring model [141] and the Rolie-double-Poly (RDP) model [142], can predict the linear and nonlinear rheological properties well, but these works still do not adopt the SORF mechanism. This RDP model can predict the transient viscosities within the regime of a short time; on the other hand, the steady elongational viscosities have difficulty in predictions under high-deformation-rate flows. We have to clarify whether the SORF mechanism is generally effective by making assessments based on more evidence, e.g., systems consisting of a larger amount of high-molecular-weight polymers.

From the viewpoint that the friction of a chain with others is a many-body problem, the coupling of the state of the entangled chain itself with the environment has not been investigated in depth. Specifically, unlike a monodispersed system where the state of a chain is statistically the same as the states of the surrounding chains, in a bidisperse system, the state of a longer or shorter entangled chain itself and the state of environments that can be evaluated by averaging the surrounding polymer chains might be different. Thus, the following question arises regarding how the friction coefficient (tensor) is determined by the state of a considering chain and/or the state of the environment around it, which factor is more

dominant, the state of the considering chain or the state of the environment. Judging from the fact that the nonlinear rheology of bidisperse polymer melts has not been well tested, we should also consider the comparison of the two contributions from the considered chain and the environment in the extension to the bidisperse systems.

In this study, we assess the SORF mechanism for the bidisperse entangled polymer melts because the empirical relation used in the previous study [140] has arbitrariness in using bidispersed polystyrene melts. In more detail, the SORF expressions thus far proposed are obtained from the monodisperse system; thus, the contribution originating from the difference in the states of the components has been ignored. This study takes into account the contribution to the friction reduction from the states of the long- and short-chain components. For such a purpose, we employ the pseudo-single-chain sliplink model, for which the effect of the SORF mechanism on the rheological properties has been tested in the case of monodisperse entangled polymer melts [85].

The contents of the present chapter are as follows. In Section 5.2, we explain the sliplink model and the SORF extension, and in Section 5.3, we show the simulation results for six experimental samples. In Section 5.4, we summarize and discuss the results.

5.2 Model

5.2.1 Doi Takimoto Original Sliplink Model

We employ a dual sliplink model developed by [23], namely, DT model. Here, "dual" refers to the assumption that an entanglement is made of two points on different chains. An entangled polymer chain is modeled by a primitive path, the two tails, and the sliplinks on the path. The sliplinks are pinned in space. A polymer molecule has two tails, and one-end of a tail is fixed by a sliplink and the other end is free. Each tail is considered to be an ideal chain. From the viewpoint of rheological properties, the entangled polymer chain is characterized by the number of entanglements at equilibrium Z_{eq} and the maximum stretch ratio $\lambda_{\max}$. The units for the model are the length of a strand between two adjacent sliplinks at equilibrium a, the Rouse relaxation time of a strand τ_{e}, and a stress value σ_{e} connected to the plateau modulus.

The state of the i-th polymer chain can be described by the positions of the sliplinks $\{\boldsymbol{R}\}$, the length of the two tails $\{s_{\mathrm{head}}, s_{\mathrm{tail}}\}$, the numbers of entanglements of a chain Z, and the pair list of the sliplinks. The primitive path length of the i-th polymer chain L^i is calculated as

$$L^i = s^i_{\mathrm{head}} + s^i_{\mathrm{tail}} + \sum_{k=1}^{Z^i-1} |\boldsymbol{r}^i_k|, \tag{5.1}$$

where $\boldsymbol{r}^i_k (= \boldsymbol{R}^i_{k+1} - \boldsymbol{R}^i_k)$ is the bond vector of the adjacent two $(k, k+1)$ sliplinks. The stretch ratio λ^i is defined as L^i/L^i_{eq} , where $L^i_{\mathrm{eq}} (= aZ^i_{\mathrm{eq}})$ is the equilibrium length of L^i.

This model contains the three relaxation mechanisms considered in the recent tube model [3]: reptation, contour length fluctuation (CLF), and constraint release (CR). It is assumed that the tension on a chain is always balanced within time τ_{e}. Note that the major difference between the DT model and the PCN model is the nonexistence of the dynamics originating from the tensile balance. Therefore, the momentum equation of the sliplink contains only affine deformation as

$$\frac{\mathrm{d}\boldsymbol{R}^i_k}{\mathrm{d}t} = \boldsymbol{\kappa} \cdot \boldsymbol{R}^i_k, \tag{5.2}$$

where $\boldsymbol{\kappa} = (\boldsymbol{\nabla v})^{\mathrm{T}}$, i.e., $\kappa_{\alpha\beta} = \nabla_\beta v_\alpha$ is the velocity gradient. The primitive path length $L^i(t)$ follows the overdamped Langevin equation with the Rouse relaxation time of a chain $\tau_{\mathrm{R}}^i = \tau_{\mathrm{e}}(Z_{\mathrm{eq}}^i)^2$,

$$\frac{\mathrm{d}L^i}{\mathrm{d}t} = -\frac{f^i}{\tau_{\mathrm{R}}^i}(L^i - L_{\mathrm{eq}}^i) + \left(\frac{\mathrm{d}L^i}{\mathrm{d}t}\right)_{\mathrm{affine}} + \sqrt{\frac{2a^2}{3\tau_{\mathrm{e}} Z_{\mathrm{eq}}^i}}\, w_{\mathrm{clf}}(t), \tag{5.3}$$

where $f^i(\equiv \{1-(1/\lambda_{\mathrm{max}}^i)^2\}/\{1-(\lambda^i/\lambda_{\mathrm{max}}^i)^2\})$ is the FENE parameter of the i-th chain, λ_{max}^i is the maximum stretch ratio of the i-th chain. $w_{\mathrm{clf}}(t)$ is a Gaussian white noise satisfying these relations:

$$\langle w_{\mathrm{clf(t)}} \rangle = 0,\ \langle w_{\mathrm{clf}}(t) w_{\mathrm{clf}}(t') \rangle = \delta(t-t'). \tag{5.4}$$

The three terms of the RHS in Eq. (5.3) refer to the contributions of the chain length restoration, the affine deformation, and the contour length fluctuation by thermal noise. By assuming a tension balance along strands, the two tails take over the change of L half by half on behalf of the pinned sliplinks. Thus, the lengths of the two ends s_{head}^i and s_{tail}^i change according to the following equations:

$$\begin{aligned}
\frac{\mathrm{d}s_{\mathrm{head}}^i}{\mathrm{d}t} &= \frac{1}{2}\left(\frac{\mathrm{d}L^i}{\mathrm{d}t} - \left(\frac{\mathrm{d}L^i}{\mathrm{d}t}\right)_{\mathrm{affine}}\right) + \sqrt{2D_{\mathrm{c}}^i}\, w_{\mathrm{rep}}(t), \\
\frac{\mathrm{d}s_{\mathrm{tail}}^i}{\mathrm{d}t} &= \frac{1}{2}\left(\frac{\mathrm{d}L^i}{\mathrm{d}t} - \left(\frac{\mathrm{d}L^i}{\mathrm{d}t}\right)_{\mathrm{affine}}\right) - \sqrt{2D_{\mathrm{c}}^i}\, w_{\mathrm{rep}}(t),
\end{aligned} \tag{5.5}$$

where $D_{\mathrm{c}}^i(= (L_{\mathrm{eq}}^i)^2/\pi^2\tau_{\mathrm{rep}}^i)$ is the diffusion constant of pure reptation motion and $\tau_{\mathrm{rep}}^i = 3(Z_{\mathrm{eq}}^i)^3\tau_{\mathrm{e}}$ is the reptation time calculated from the Doi-Edwards model [6]. The first term in the RHS in Eq. (5.5) is related to the contributions in Eq. (5.3) except for the affine deformation, and the second term is related to the thermal fluctuations. Here, $w_{\mathrm{rep}}(t)$ is a Gaussian white noise that satisfies the same equation as Eq. (5.4) of w_{clf}. The lengths of the two ends are checked every τ_{e}. If the length of an end is more than a or less than zero, the creation or annihilation of entanglement occurs, respectively, which mimics constraint renewal.

The stress $\boldsymbol{\sigma}$ of the system consisting of N_{chain}-chains in the volume V is calculated with the Kramers formula:

$$\boldsymbol{\sigma} = \sigma_{\mathrm{e}} \left\langle f \frac{\boldsymbol{r}\boldsymbol{r}}{a|\boldsymbol{r}|} \right\rangle. \tag{5.6}$$

The unit stress σ_{e} is related to the plateau modulus G_{N} as

$$\sigma_{\mathrm{e}} = \frac{3k_{\mathrm{B}}T}{V} \sum_{i=1}^{N_{\mathrm{chain}}} Z_{\mathrm{eq}}^i = \frac{3\rho RT}{M_{\mathrm{e}}} = \frac{15}{4} G_{\mathrm{N}}, \tag{5.7}$$

where ρ is the mass density, R is the gas constant, k_{B} is the Boltzmann constant, T is the temperature, and M_{e} is the entanglement molecular weight. The plateau modulus G_{N} is generally expressed as

$$G_{\mathrm{N}} = A\frac{\rho RT}{M_{\mathrm{e}}}, \tag{5.8}$$

where the constant A equals 4/5 when considering the thermal fluctuations of the length along the primitive path [6]. Note that [143] reported a more detailed analysis of this factor A.

Table 5.1 Conditions with experiments and simulations

No.	sample code	Z^{S}	Z^{L}	$\lambda_{\max}$	T [°C]	τ_{e} [s]	σ_{e} [MPa]
I	PS-_95S-545L-50w	8.6	50	4.4	130	0.16	0.68
II	PS-_52S-390L-_4w	4.5	36	4.4	130	0.16	0.68
III	PS-_52S-390L-14w	4.5	36	4.4	130	0.16	0.68
IV	PS-100S-390L-14w	9.1	36	4.4	130	0.16	0.68
V	PI-_23S-226L-20w	5.3	53	5.9	25	1.1×10^{-5}	1.2
VI	PI-_23S-226L-40w	5.3	53	5.9	25	1.1×10^{-5}	1.2

5.2.2 Proposed Extension of a SORF Expression

At present, the contributions of SORF are determined by empirical order parameters correlated to the stretch and orientation [132, 144]. In this study, we utilize the relation proposed by [132]. The expression is accurate enough to reproduce the rheological properties.

We briefly explain the SORF mechanism considered in the original study for a monodisperse polymer melt. To express the segments' orientation and stretch to the elongational direction, [132] proposed the stretch/orientation order parameter $F_{\mathrm{s/o}}$ defined as

$$F_{\mathrm{s/o}} \equiv \tilde{\lambda}^2 \bar{S}, \tag{5.9}$$

where $\tilde{\lambda} = \lambda/\lambda_{\max}$ and $\bar{S}$ is the averaged orientation anisotropy, defined as

$$\bar{S}(\boldsymbol{S}) \equiv |s_1 - s_2|, \tag{5.10}$$

where $\boldsymbol{S} = \langle \boldsymbol{u}\boldsymbol{u} \rangle$ is the orientation tensor, $\boldsymbol{u}(= \boldsymbol{r}/|\boldsymbol{r}|)$ is the normalized bond vector between the adjacent sliplinks, and s_1 and s_2 are respectively the maximum and minimum eigenvalues of the orientation tensor.

[132] derived the empirical relation between the friction coefficient ζ and the order parameter $F_{\mathrm{s/o}}$,

$$\begin{aligned} \frac{\tau_{\mathrm{e}}(F_{\mathrm{s/o}})}{\tau_{\mathrm{e}}(0)} &= \frac{\zeta(F_{\mathrm{s/o}})}{\zeta(0)} \frac{1}{f_{\mathrm{FENE}}} \\ &= \frac{1}{(1+\beta)^{\gamma}} \left[\beta + \frac{1 - \tanh\left\{ \alpha(F'_{\mathrm{s/o}} - F'^{*}_{\mathrm{s/o}}) \right\}}{2} \right]^{\gamma}, \end{aligned} \tag{5.11}$$

where $f_{\mathrm{FENE}}(\equiv 1/(1-\tilde{\lambda}^2))$ is the FENE parameter. For $F'_{\mathrm{s/o}} \equiv f_{\mathrm{FENE}} F_{\mathrm{s/o}}$, the parameters $\alpha = 20$, $\beta = 5.0 \times 10^{-9}$, $\gamma = 0.15$, and $F'^{*}_{\mathrm{s/o}} = 0.14$ are obtained from the experiments in monodispersed PS melts. $F'_{\mathrm{s/o}}$ used here is the same as that used in [132]. The reason why they introduced $F'_{\mathrm{s/o}}$ is that it is impossible to experimentally separate f_{FENE} from $F_{\mathrm{s/o}}$. In this study, we just follow the way used by [132]. Eq. (5.11) expresses the friction change to a lower value by exceeding the threshold parameter of $F'_{\mathrm{s/o}}$, and was used for the multichain sliplink model [22] and the DT model [23]. [133] used Eq. (5.11) with the above parameter values to examine polyisoprene and poly(n-butyl acrylate) melts and found that the predictions were improved. Nevertheless, the parameter could not be applied universally for chemical structures; thus, [85] reported that a smaller value of $F'^{*}_{\mathrm{s/o}} \simeq 0.007$ gives better predictions for PI melts.

Note that there are other expressions for SORF. For example, [144] used a power-law-type function to describe friction reduction. While these can also reasonably improve the predictions for the entangled

and unentangled polymer melts, the functional form and the order parameter have not yet been fully established.

We also note that the strength of the thermal fluctuation is determined using the friction coefficient under flows through the fluctuation-dissipation theorem. Recently, Watanabe and coworkers discussed the change in the Brownian force intensity under strong flow for unentangled chains[138, 139, 145]. Using the modified Rouse (or dumbbell) model to allow the spring strength, friction coefficient, and the strength of the Brownian force to be changed, they formulated rheological quantities under shear and elongational flow. Using these rheological quantities, they found that the fluctuation-dissipation theorem might not be valid under strong flow. Since the origin of the friction is local dynamics, this argument can also be applied to entangled melts. Nevertheless, considering the strength of the thermal fluctuation is outside this study's scope and deferred to future research.

The application of Eq. (5.11) to the polydisperse melts has arbitrariness in terms of averaging the stretch and the orientational anisotropy. The SORF expressions are thus far obtained from monodispersed polymer melt systems. Unlike a monodisperse system where the state of a chain is statistically the same as the states of the surrounding chains, in a polydisperse system, the state of a component often differs from those of other components. For example, in a bidisperse system, the state of a longer or shorter entangled chain and the state of the environment defined by an average over the surrounding polymer chains might be different under a flow because the two types of chains have different relaxation times. The friction of a chain moving relative to the surrounding chains can be considered to be a consequence of many-body interaction among them, and the coupling of the state of the entangled chain itself with the environment has not yet been clarified. Therefore, the following question arises regarding how the friction coefficient (in general, friction coefficient tensor) of a polymer chain along its contour is determined by (i) the state of the considering chain and/or (ii) the state of the environment around it, and furthermore, which factor of the two is more dominant, (i) or (ii).

In this study, we investigate bidisperse blend systems composed of long and short chains (hereafter $\mathtt{C}$ stands for a component, i.e., $\mathtt{C}$="short" or "long"), where we consider different types of SORF expressions by replacing the statistical quantities in $F'_{\mathrm{s/o}}$ in (5.11). Eight types of SORF expressions for a chain belonging to a component $\mathtt{C}$ are possible by changing the averages for the statistical quantities: the chain stretch ratio λ and orientation tensor $\boldsymbol{S}$ used in the parameter $F'_{\mathrm{s/o}}$, i.e.,

$$F'^{(\mathtt{X\_Y\_Z})}_{\mathrm{s/o}} = f_{\mathrm{FENE}}(\langle\tilde{\lambda}\rangle_{\mathtt{X}})F_{\mathrm{s/o}}(\langle\tilde{\lambda}\rangle_{\mathtt{Y}}, \boldsymbol{S}_{\mathtt{Z}}), \tag{5.12}$$

for the bidisperse blend systems instead of $F'_{\mathrm{s/o}}$ in Eq. (5.11). The superscript $\mathtt{X\_Y\_Z}$ refers to averaging the arguments, where $\mathtt{X}$ stands for the normalized stretch ratio in the FENE factor, $\mathtt{Y}$ for the normalized stretch ratio in the order parameter $F_{\mathrm{s/o}}$, and $\mathtt{Z}$ for the orientation. $F'_{\mathrm{s/o}}$ consists of the two contributions f_{FENE} and $F_{\mathrm{s/o}}$, and one can consider that two contributions may have different physical origins. For instance, in a monodisperse polymer system, the average quantities used in the two contributions are considered to be identical; in a bidispersed polymer system, they might be different because the state of a considering type of chain, e.g., a long chain can be different from the average over the whole long and short chains. Therefore we retain possible combinations of variables in $F'_{\mathrm{s/o}}$, and discuss later which combination is the better one.

The component average of a quantity Q, $\langle Q\rangle_{\mathtt{C}}$ means the average of Q over the chains with the same equilibrium length as a considering chain; on the other hand, the system average of Q, $\langle Q\rangle_{\mathtt{S}}$ expresses overall average of the chains (in other words, environment around the considering chain). The subscripts $\mathtt{S}$ and $\mathtt{C}$ indicate the averages of stretch and orientation over the system and the component, respectively.

For example, the superscript C_S_S on $F'_{\mathrm{s/o}}$ means the component average is used for the FENE parameter, the system average for the stretch ratio λ and the orientation tensor $\boldsymbol{S}$ in $F_{\mathrm{s/o}}$. Note that [140] used the system averages for all quantities in $F'_{\mathrm{s/o}}$; specifically, they used $F'_{\mathrm{s/o}}$, expressed as S_S_S in our notation.

In the next section, we focus on the three combinations, i.e., C_S_S, C_C_S, and S_S_S. Here, we can consider the eight combinations at maximum. However, the four combinations S_S_Z and X_C_C clearly give no meaningful results in agreement. In the remaining half, the two expressions, C_S_S and S_C_S, gave similar results to each other for the examined samples in this study. Considering the roles of the factors in $F'_{\mathrm{s/o}}$, the factor f_{FENE} comes from the finite extensibility of chains, so we consider it natural that f_{FENE} is reflected from the state of the considered chain. In the next section, we discuss the results using C for X in X_Y_Z on supposing the factor f_{FENE} reflects the finite extensibility of the chains under consideration. The remaining two combinations, C_C_S and C_S_C, provide mutually similar results to each other for the examined samples. C_C_S clearly focuses on the stretch ratios of the considered chains and the orientation anisotropy of the entire system. On the other hand, the interpretation of C_S_C on the physical meanings has considerable complexity. Therefore, we provide the results in C_C_S, and the discussion on the difference between C_C_S and C_S_C is excluded from the target of this research. To summarize, in the next section, we discuss the results for three cases: S_S_S, C_S_S, and C_C_S; i.e., S_S_S is chosen as a reference case for the previous research where just system averages were used, and C_S_S and C_C_S are chosen as the representative cases where the component average for the stretch of the considered chains is taken into account.

5.3 Results and Discussion

The systems considered here are bidisperse polymer blends. In Table 5.1, we show the characteristics of each system and their simulation conditions. The sample code is given as PS-AAAS-BBBL-CCw, where PS (or PI) stands for polystyrene (or polyisoprene), AAA is the molecular weight of the main-polymer component in the unit of kDa, BBB also denotes the molecular weight of the secondary polymer component in the unit of kDa, and CC expresses the weight percent of the secondary component in the system. Z^{S} is the number of entanglements at equilibrium Z_{eq} for the short chain (the main component), and Z^{L} denotes that for the long chain (the secondary component).

5.3.1 Fitting to the Experimental Linear Viscoelasticity

We first compare the storage modulus $G'(\omega)$ and the loss modulus $G''(\omega)$ calculated from the simulations with experimental results to determine the unit values τ_{e} and σ_{e}, and thus obtain the Rouse relaxation time $\tau_{\mathrm{R}}(= Z_{\mathrm{eq}}^2\tau_{\mathrm{e}})$ and the longest relaxation time τ_{d}. The fitted parameters are $\tau_{\mathrm{e}} = 0.16$ s and $\sigma_{\mathrm{e}} = 0.68$ MPa for 130 °C PS melts. These values are of similar order to the previous reports by [146] and [85]. For 25 °C PI melts, the values are $\tau_{\mathrm{e}} = 1.1 \times 10^{-5}$ s and $\sigma_{\mathrm{e}} = 1.2$ MPa. In appendix 5.3.1, we show the fitted complex moduli for the bidisperse PS and PI melts and the monodisperse PS melts containing polymers of the same molecular weight polymers as before blending, as shown in Figs. 5.1, 5.2, 5.3, and 5.4. The predictions of the linear viscoelasticities (LVEs) are in agreement with the experimental results obtained from the blends.

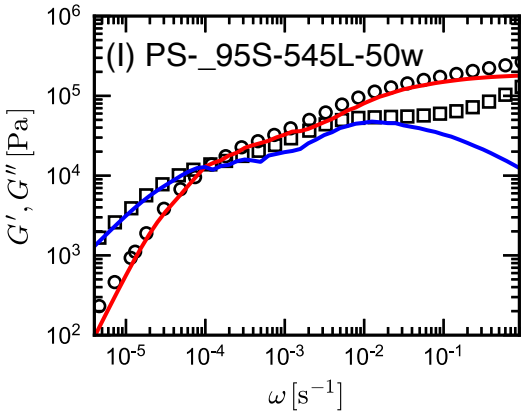

Fig. 5.1 Storage (circles and red line) and loss (squares and blue line) moduli of (I) PS-_95S-545L-50w. The solid lines represent those obtained by the DT model. Symbols express those obtained by [126].

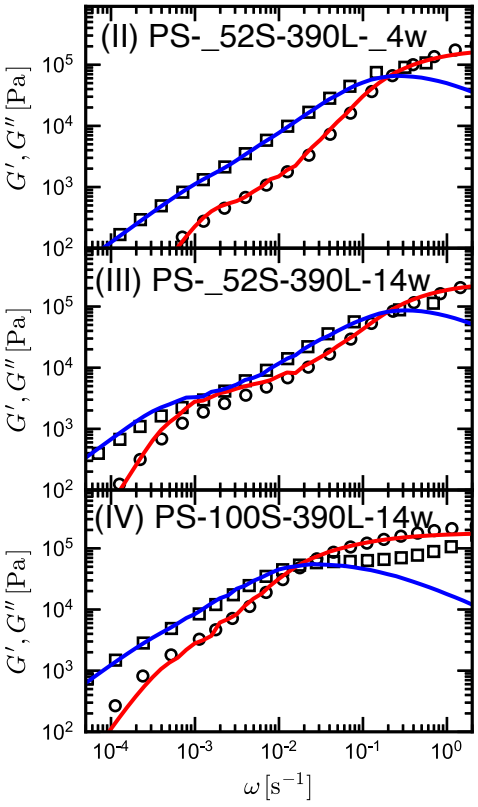

Fig. 5.2 Storage (circles and red line) and loss (squares and blue line) moduli of (II) PS-_52S-390L-_4w, (III) PS-_52S-390L-14w, and (IV) PS-100S-390L-14w. The solid lines represent those obtained by the DT model. Symbols express those obtained by [124].

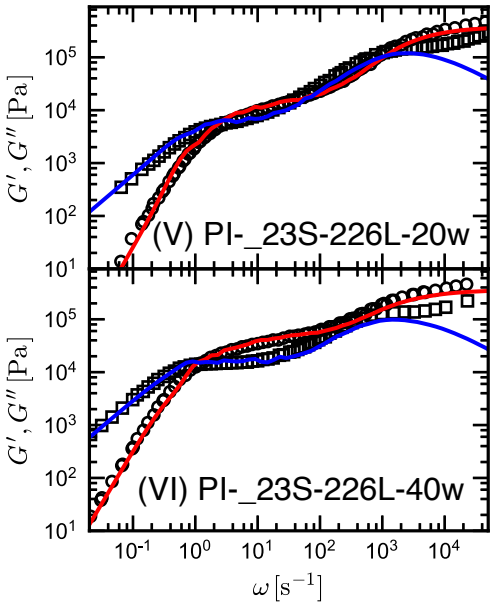

Fig. 5.3 Storage (circles and red line) and loss (squares and blue line) moduli of (V) `PI-_23S-226L-20w`, and (VI) `PI-_23S-226L-40w`. The solid lines represent those obtained by the DT model. Symbols express those obtained by [147].

The linear relaxation modulus $G(t)$ is calculated from the autocorrelations as

$$\begin{aligned} G(t) =& \frac{V}{5k_{\mathrm{B}}T}(\langle\sigma_{xy}(t)\sigma_{xy}(0)\rangle + \langle\sigma_{yz}(t)\sigma_{yz}(0)\rangle \\ &+ \langle\sigma_{zx}(t)\sigma_{zx}(0)\rangle) + \frac{V}{30k_{\mathrm{B}}T}(\langle N_{xy}(t)N_{xy}(0)\rangle \\ &+ \langle N_{yz}(t)N_{yz}(0)\rangle + \langle N_{zx}(t)N_{zx}(0)\rangle), \end{aligned} \tag{5.13}$$

where $\sigma_{\alpha\beta}$ is the $\alpha\beta$ component of the stress tensor and $N_{\alpha\beta}(=\sigma_{\alpha\alpha}-\sigma_{\beta\beta})$ is the normal stress difference. The multiple-tau method [148] enables us to evaluate the autocorrelations efficiently. The complex modulus $G^*(\omega)$ composed of storage and loss moduli is evaluated from $G(t)$:

$$G^*(\omega) = G'(\omega) + iG''(\omega) = i\omega\int_0^\infty G(t)e^{-i\omega t}\mathrm{d}t. \tag{5.14}$$

The integral of $G(t)$ is evaluated by the data of N points:

$$\begin{aligned} \int_0^\infty G(t)e^{-i\omega t}\mathrm{d}t &= \sum_{k=1}^{N-1}\int_{t_k}^{t_{k+1}} G(t)e^{-i\omega t} \\ &= \sum_{k=1}^{N-1} G(t_k)e^{-i\omega t_k}C + G(t_{k+1})e^{-i\omega t_{k+1}}\bar{C}, \\ &\text{where } C = \frac{1-i\omega(t_{k+1}-t_k)-e^{-i\omega(t_{k+1}-t_k)}}{\omega^2(t_{k+1}-t_k)}. \end{aligned} \tag{5.15}$$

C is the complex constant, and $\bar{C}$ is the conjugate number of C.

The reference data and the predictions from the extended Doi-Takimoto model are shown by the symbols and black lines, respectively, in Fig. 5.1 [126], Fig. 5.3 [147], and Fig. 5.2 [124]. These figures

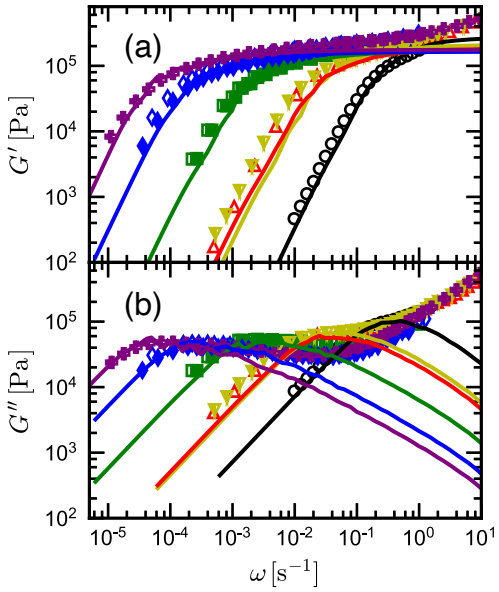

Fig. 5.4 (a) Storage modulus and (b) loss modulus. The graphs show the compared results with 130°C PS52K [124], PS95K [126], PS100K [124], PS200K [124, 149], PS390K [124, 149] and PS545K [126]. Circles, upper triangles, lower triangles, squares, diamonds, and crosses show the experimental results of PS52K, PS95K, PS100K, PS200K, PS390K and PS545K, respectively. The unfilled, filled and left-filled markers show the results of experiments reported by [124], [149] and [126], respectively. Lines show the results of the DT model simulations.

display only the regions of the terminal relaxation and the plateau, which can be calculated by the DT model. The simulation results predict the two contributions of the short chains and the long chains. Figs. 5.1-5.3 show that the DT model can successfully reproduce the linear rheological properties of bidispersed polymers except for the high frequency region. The deviation from the experimental data in the high frequency range is due to the lack of the Rouse-like dynamics in the DT model.

The values of τ_e and σ_e are determined from the LVE results of bidisperse entangled polymer melts. Here, we show the comparison between the simulations and the data of monodisperse melts. Fig. 5.4 shows the linear viscoelasticity of the monodispersed polystyrene samples before blended. The numbers of entanglements at equilibrium Z_{eq} equal 4.5, 8.6, 9.1, 18, 36, and 50 for the molecular weights 52 K, 95 K, 100 K, 200 K, 390 K, and 545 K of the mono-dispersed PS melts (130°C), respectively. The results from the DT model, the storage and the loss moduli, match almost all the data, but the simulation results for PS95K and PS100K slightly deviate from the data obtained from [126] and [124].

5.3.2 Tests with Polystyrene Melts for Comparing Four SORF Expressions

In this section, we compare selected SORF expressions defined in Eq. (5.12) to the experimental results for the uniaxial elongations. Figures 5.5 and 5.6 show the predictions with the extended DT model for the transient viscosities under elongational flows. Figure 5.5 displays the stress growth and relaxation for the bidisperse system-I reported by [126], which consists of the high weight fraction of the long chains (50 wt%). In contrast, Fig. 5.6 expresses the transient viscosities of the three samples with low weight fractions (4 wt%-14 wt%). The two out of the three samples, II and IV, are reported by [124] and III is

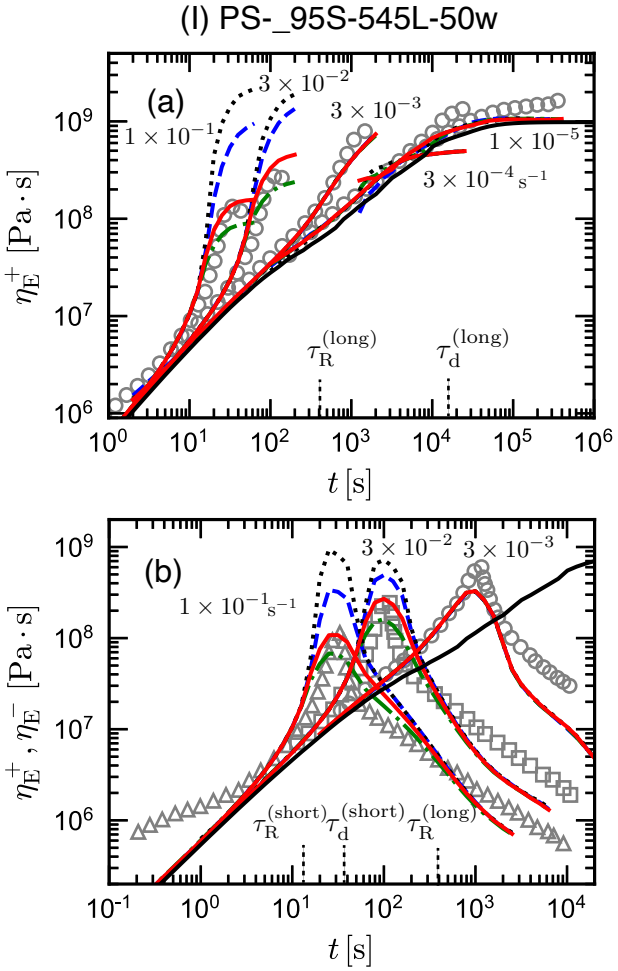

Fig. 5.5 (a) Elongational transient viscosities and (b) transient viscosities in stress-growth-and-relaxation measurements of (l) `PS-_95S-545L-50w` reported by [126], showing initial uniaxial elongation deformation with a constant elongational strain rate up to the fixed Hencky strain $\varepsilon_0 = 3.5$ and then a strain rate set to zero. The colored lines and black dotted lines are the results obtained by the extended DT model with and without SORF, respectively. The blue dashed, red solid, and green dash-dotted lines correspond to the SORFs calculated from the different combinations for `X_Y_Z`: `S_S_S`, `C_S_S`, and `C_C_S`, respectively. The black solid line indicates the LVE result. (a) The circles are the experimental results under elongational flows having the five strain rates: 1×10^{-5}, 3×10^{-4}, 3×10^{-3}, 3×10^{-2}, and $1 \times 10^{-1}\mathrm{s}^{-1}$ from right to left. (b) The circles, squares, and triangles represent the experiments with the three respective elongational strain rates 3×10^{-3}, 3×10^{-2}, and $1 \times 10^{-1}\mathrm{s}^{-1}$ from right to left.

reported by [125].

Figure 5.5 shows (a) elongational transient viscosities and (b) transient viscosities ($\eta_{\rm E}^{+}$ for the start-up and $\eta_{\rm E}^{-}$ after the cessation) in stress-growth-and-relaxation measurements of (I) PS-_95S-545L-50w under elongational flows. In Fig. 5.5a, the five series data points of the transient viscosities expressed as the symbols are for the experiments with constant elongational strain rates: 1×10^{-5}, 3×10^{-4}, 3×10^{-3}, 3×10^{-2}, and 1×10^{-1} s^{-1} from right to left. Fig. 5.5b shows the three data points of the stress growth and relaxation after the cessation, displaying initial uniaxial elongation deformation with a constant strain rate up to the fixed Hencky strain $\varepsilon_0 = 3.5$ and then a strain rate set to zero. The three strain rates are 3×10^{-3}, 3×10^{-2}, and 1×10^{-1} s^{-1}. As a reference, the Rouse relaxation time and the longest relaxation time are evaluated to be $\tau_{\rm R}^{\rm (long)} (= (Z^{\rm L})^2 \tau_{\rm e}) = 4.0 \times 10^2$ s and $\tau_{\rm d}^{\rm (long)} = 1.6 \times 10^4$ s for the long chain, respectively. The relaxation times of the short chains are smaller than those of the long chains, which are $\tau_{\rm R}^{\rm (short)} (= (Z^{\rm S})^2 \tau_{\rm e}) = 12$ s and $\tau_{\rm d}^{\rm (short)} = 36$ s. These quantities for this sample I and those for other samples (II-IV) and appear later as obtained by the analyses of the linear viscoelasticity data (see Appendix 5.3.1).

In Figs. 5.5a and 5.5b, the predictions by extended DT models with C_S_S (colored solid lines), C_C_S (colored dash-dotted lines), S_S_S (colored dashed lines), and by the DT model without SORF (black dotted lines) are shown. From these figures, both C_S_S and C_C_S are in agreement with the experimental results. On the other hand, those for S_S_S (colored dashed lines) and without SORF overestimate the experimental values in the two high-deformation-rate flows: 3×10^{-2}, and 1×10^{-1} s^{-1}, which are in the region $\dot{\varepsilon} > 1/\tau_{\rm R}^{\rm (long)}$. When comparing the predictions with C_S_S and C_C_S, C_S_S gives the best prediction for the steady values of the transient viscosities and the maximum values for the stress growth. Under flows, the averaged stretch has the relation: $\langle\lambda\rangle_{\rm C=\text{“}long\text{”}} > \langle\lambda\rangle_{\rm S} > \langle\lambda\rangle_{\rm C=\text{“}short\text{”}}$. Thus, the contribution of SORF is larger when using C_S_S and C_C_S, that is, the notable failure of S_S_S for $\dot{\varepsilon} > 1/\tau_{\rm R}^{\rm (long)}$ comes from the less effect of SORF on the stress. Regarding the average of λ used in $f_{\rm FENE}$, the results obtained by the component average is better than those by the system average. Thus, $f_{\rm FENE}$ in $F'_{\rm s/o}$ should be determined by the average over the chains of the same type as the considering chain as expected in Sec.2.2.

In Fig. 5.5a, the nonlinear behavior of the DT model changes from strain softening to strain hardening with increasing the elongational strain rate. However, the experimental results of (I) PS-_95S-545L-50w do not show such strain softening of the simulation results for the middle elongational strain rate region $1/\tau_{\rm R}^{\rm (long)} < \dot{\varepsilon} < 1/\tau_{\rm d}^{\rm (long)}$. We suppose that the relaxation of the long chain is overestimated compared to that expected from the experiments for bidisperse blend systems. The underestimation of the transient viscosities appears in previous studies for polydisperse polymer melts with the original Doi-Takimoto model [23] and for bidisperse polymer melts with the multichain sliplink model [140].

In Fig. 5.5b, especially in the case of $\dot{\varepsilon} = 1.0 \times 10^{-1}$ s^{-1}, the best prediction by C_S_S (green solid line) cannot fully reproduce the two-step relaxation after flow cessation. Considering the time, the first of the two-step relaxation behavior seems to correspond to the Rouse relaxation time of the short chains. It is assumed that the fast dynamics of the tensile balance not considered here cause the deviation. In the long-term regime, the predictions show underestimates of the elongational viscosity from the experimental results after cessation, notably for the lower deformation rates. [85] demonstrate the predictions for PS145k show the deviation similar to this at the long time region. We consider that the dynamics of the long chains dominate the relaxation on the long time scale, but the relaxation of the long chains in our model seems faster than that expected by the experimental results.

Through these results for (I) PS-_95S-545L-50w in Fig. 5.5, we find that the statistical averages

over each component are important in the system with the high weight fraction (50wt%) of the long chains, where C_S_S is the best one. The success of C_S_S, as well as C_C_S, implies that f_{FENE} should be evaluated from the considering chains. In system (I), dominated by the long chains of 50 wt%, the system averages used to evaluate $F_{\mathrm{s/o}}$ reasonably match the component averages over the long chains. Hence, the difference in $F'_{\mathrm{s/o}}$ between C_S_S and C_C_S should be small. In the next paragraph, by using the three types of expressions of $F'_{\mathrm{s/o}}$, we discuss the prediction of rheology for the systems with the lower-weight fractions of the long chains.

Figure 5.6 displays the transient elongational viscosities η_{E}^{+} for (II) PS-_52S-390L-_4w, (III) PS-_52S-390L-14w, and (IV) PS-100S-390L-14w. The data in graphs II and IV are obtained from [124], and the data in graph III are obtained from [125]. The characteristic times of the long chain have the values $\tau_{\mathrm{R}}^{(\mathrm{long})} = 2.1 \times 10^2$ s and $\tau_{\mathrm{d}}^{(\mathrm{long})} = 5.0 \times 10^3$ s for PS390k. The values of the short chain for II and III are $\tau_{\mathrm{R}}^{(\mathrm{short})} = 3.2$ s and $\tau_{\mathrm{d}}^{(\mathrm{short})} = 3.8$ s for PS52K, and those for IV are $\tau_{\mathrm{R}}^{(\mathrm{short})} = 13$ s and $\tau_{\mathrm{d}}^{(\mathrm{short})} = 44$ s for PS100K. The circles are the experimental results under elongational flows having the five elongational strain rates 3×10^{-3}, 1×10^{-2}, 3×10^{-2}, 1×10^{-1}, 3×10^{-1} s^{-1} for II and under the elongational flows also having the five elongational strain rates: 1×10^{-3}, 3×10^{-3}, 1×10^{-2}, 3×10^{-2}, and 1×10^{-1} s^{-1} for III from right to left. For IV, the elongational flows have the six elongational strain rates 1×10^{-4}, 3×10^{-3}, 1×10^{-2}, 3×10^{-2}, 1×10^{-1}, and 3×10^{-1} s^{-1}. In the three figures for II (top), III (middle), and IV (bottom), the SORF effects with the component averages (C_S_S and C_C_S) fundamentally improve the predictions for the higher elongational strain rates than $1/\tau_{\mathrm{R}}^{(\mathrm{long})}$, which correspond to the two or three $\dot{\varepsilon}$ cases from the left. On the other hand, the predictions with the SORF effects just with the system averages (S_S_S expressed by colored dashed lines) are almost the same as those without SORF, especially in the results of II and III. The predictions of C_S_S (colored solid lines) are the best for sample II, those of C_C_S (colored dash-dotted lines) are the best for sample III, and those of C_S_S and C_C_S are in agreement for sample IV.

By focusing on the data from the higher deformation-rate flows ($\dot{\varepsilon} > 1/\tau_{\mathrm{R}}^{(\mathrm{long})}$), we find that the C_S_S and C_C_S predictions are the best for the steady viscosities in the two results, II and III, respectively. The SORF expression with C_C_S shows the best results for the two samples, (III) PS-_52S-390L-14w and (IV) PS-100S-390L-14w, while the predictions underestimate the viscosities for the two samples (I) PS-_95S-545L-50w and (II) PS-_52S-390L-_4w. On the other hand, the predictions obtained from C_S_S are the best for the two samples, I and II. The two samples, I and II, have the long chain's high and low weight fractions (50wt% and 4wt%) and are dominated by the contributions of the long and short chains, respectively. Thus, on the assumption that the order parameter $F_{\mathrm{s/o}}$ should describe the environment around the considered chain in the experiments, we find that the $F_{\mathrm{s/o}}$ obtained from the system averages rather than the component averages can describe the elongational rheological properties of the two systems, I and II. On the other hand, this $F_{\mathrm{s/o}}$ obtained from the system averages does not fully describe the two systems, III and IV, with the long chain's middle weight fractions.

In this section, we found that the importance in using the component averages from the comparison in the different SORFs. The SORF expression with the component average improves the predictions for all the examined samples having the molecular weights (4-50 wt%) of the minor component under the high-deformation-rate flows with a large elongational strain rate ($\dot{\epsilon} > 1/\tau_{\mathrm{R}}^{(\mathrm{long})}$). For the dynamics of the polymer chain, taking into account the state of the considered chain is necessary for the evaluation of the reduction of friction. We should confirm how much the condition of a shorter or longer component is extremely different from that of the other under flows. In the next subsection, we investigate how much difference in the states appears between long and short chains.

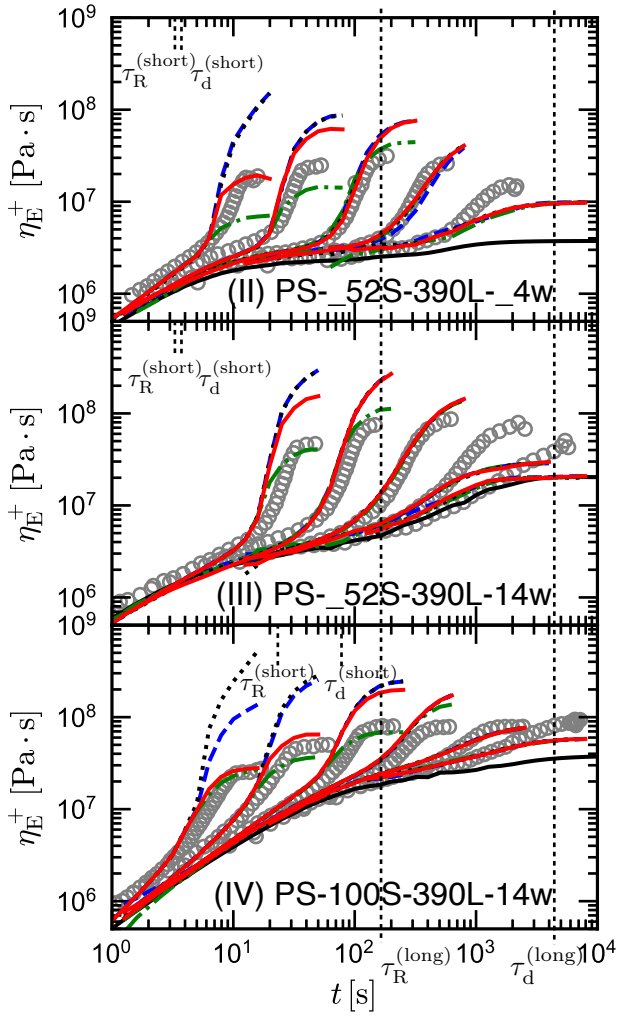

Fig. 5.6 Transient elongational viscosities of (II) PS-_52S-390L-_4w, (III) PS-_52S-390L-14w, and (IV) PS-100S-390L-14w. (circles) The data in graphs II and IV are obtained from [124], and the data in graph III are obtained from [125]. The blue dashed, red solid, and green dash-dotted lines correspond to the SORFs calculated from the different arguments: S_S_S, C_S_S, and C_C_S, respectively. The black dotted and solid lines are the simulation results without the SORF and the LVE result, respectively. The vertical lines across the graphs correspond to the Rouse and longest relaxation times of the long chain. The circles are the experimental results under elongational flows having six strain rates: 1×10^{-3}, 3×10^{-3}, 1×10^{-2}, 3×10^{-2}, 1×10^{-1}, and 3×10^{-1} s^{-1} from right to left. Here, the graphs for II, III, and IV show the experimental results with only the five smaller strain rates, only the five larger strain rates, and all the strain rates, respectively.

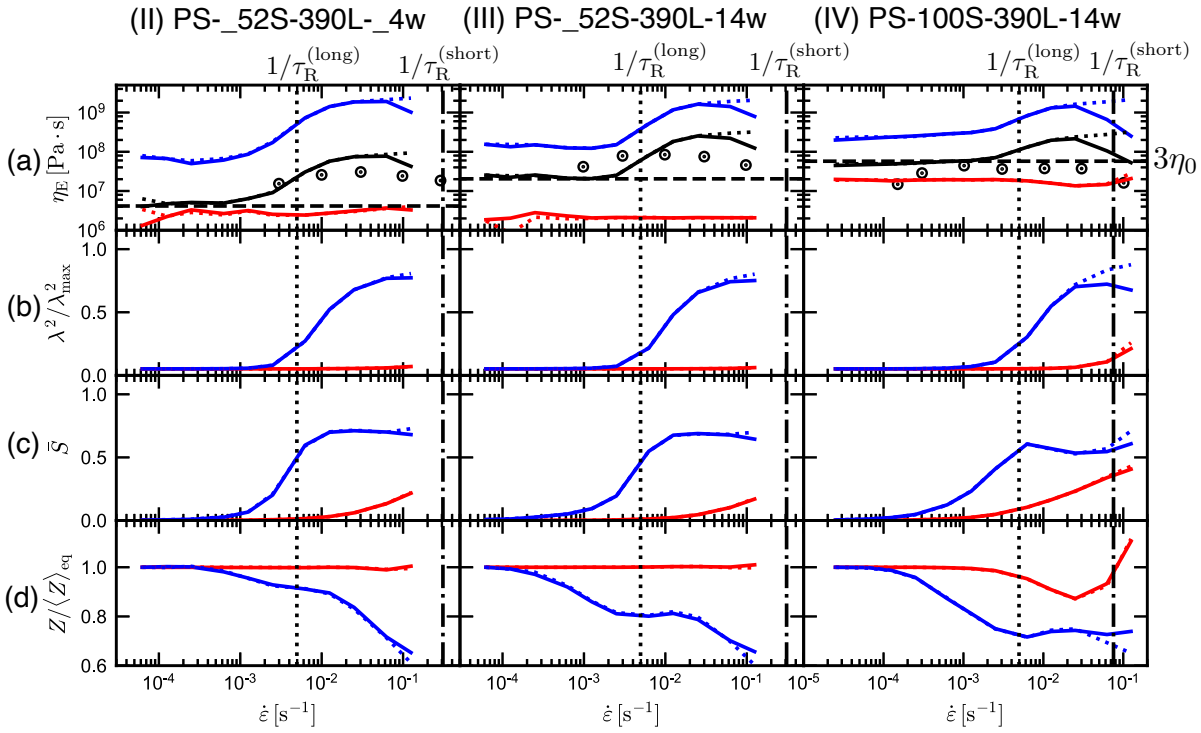

Fig. 5.7 (a) Elongational viscosities, (b) normalized stretch rates, (c) orientational anisotropy, and (d) normalized numbers of entanglements for (II) `PS-_52S-390L-_4w`, (III) `PS-_52S-390L-14w`, and (IV) `PS-100S-390L-14w`. The black, red, and blue lines with symbols express the statistical value averaged over the system, the major component (short chains), and the minor component (long chains), respectively. The solid and dotted lines correspond to the results with and without the SORF mechanism, respectively. In graph (a), the dashed horizontal line displays the three times of the zero viscosity $3\eta_0$ calculated from the LVE results by the DT model, and the dotted and dash-dotted vertical lines show the inverse of the Rouse relaxation times τ_R of the long and short chains.

5.3.3 Investigation of Steady Elongational Viscosity

Next, we investigate the rheological properties of bidisperse blend systems and the state for each component of polymer chains by using the DT model with a SORF expression using the component averages (`C_S_S` as an example). As shown in the previous section, we could not find the clear superiority or inferiority between `C_S_S` and `C_C_S`; of course, these two are superior to the other combination, say, `S_S_S`. The expressions `S_Y_Z` and `C_C_C` do not take this aspect into consideration because they do not give better results or it is difficult to give clear physical meanings to them. For example, it has been confirmed that the results with `C_C_C` show a clear underestimate for the experimental results although we do not show data in the present chapter due to excessively large deviations.

Thus, the reason to use `C_S_S` and not `C_C_S` is the simplicity and relatively clear physical meaning of the formula, in that the FENE parameter f_{FENE} in Eq. (5.11) expresses the contribution of the considered chains and the order parameter $F_{s/o}$ in Eq. (5.11) expresses that from the environment. Figure 5.7

displays the steady-state properties for the three PS samples reported by [124] for investigating the difference in the states of the long and short chains under elongational flows. In addition, to test the chemical dependence of the friction reduction mechanism in other bidisperse polymer melts, we also study the transient viscosities under steady shears in Figure 5.8 with two PI systems reported by [147].

Figure 5.7 shows the (a) steady state elongation viscosity, (b) stretch ratio, (c) orientation anisotropy, and (d) numbers of entanglements on a chain for (II) `PS-_52S-390L-_4w`, (III) `PS-_52S-390L-14w`, and (IV) `PS-100S-390L-14w`, from top to bottom. The solid and dotted lines are the results with and without SORF, respectively. Here, we adopt the `C_S_S` expression to evaluate the parameter $F'_{\mathrm{s/o}}$. The red and blue lines are the averages over short chains and long chains, respectively. The black solid lines and the black dashed lines are the steady viscosities and the LVE results, respectively. The symbols are the experimental values having unimodal shapes obtained from the report by [124]. As seen from the three columns of II (left), III (center), and IV (right), the states of the short and long chains are notably different from each other. The long chains are fully oriented and stretched under the region where the anisotropy and the stretch of the short chain do not largely change. The difference in the state between the components should be critical when considering friction reduction.

The decrease in the steady elongation viscosities appears under high-deformation-rate flows, while the orientational anisotropy of the short chains increases. This tendency of the decrease is in agreement with the experimental results. From the right column for IV, the behavior in the steady viscosities clearly appears to suppress the stretch ratios of the long chains. In the left column II, the steady viscosities evaluated by the DT model with and without the SORF are slightly different for the small strain rate region, and the difference is considered to originate from the thermal fluctuations. Note also that the steady viscosities obtained by the PCN model [140] slightly increase even with the small elongational strain rate, but our simulations do not show such increases. The major difference between their PCN model and the DT model is whether the dynamics of the force balances exist. The strands of the long chains pull the short chains, and both dynamics with and without force balance may cause the difference.

In the left and center columns for II and III, the (a) viscosities, (b) stretch ratios, and (c) orientational anisotropy are similar to each other, but (d) the numbers of entanglements of (III) `PS-_52S-390L-14w` remarkably decrease around the vertical dotted line ($1/\tau_{\mathrm{R}}^{(\mathrm{long})}$) with the elongational strain rate compared to those of (II) `PS-_52S-390L-_4w`. The difference between II and III systems is simply the weight percent of the minor component (the long chains), that is, the ease in the releasing "long-long" chains entanglements changes more than that in the "long-short" chains entanglements under convection. We suppose that the long chains easily release the entanglements under the small elongational deformation rate flows.

In the right column of Fig. 5.7(d), the normalized number of entanglements shows an upturn in the high deformation rate region. We consider that the upturn of $\langle Z \rangle / Z_{\mathrm{eq}}$ is unphysical, and should be improved. Nevertheless, the previous study [85] demonstrates that the increase of Z in the region $\dot{\epsilon} > 1/\tau_{\mathrm{R}}$ does not bring the unreasonable rheological properties and the unphysical conformation since the increased entanglements near the ends only slightly contributes to the stress. Since the upturn is not observed in the PCN model from the comparison with the DT model reported by [85], this might come from the difference between the DT model and the PCN model, e.g., the Rouse dynamics faster than $1/\tau_{\mathrm{R}}$.

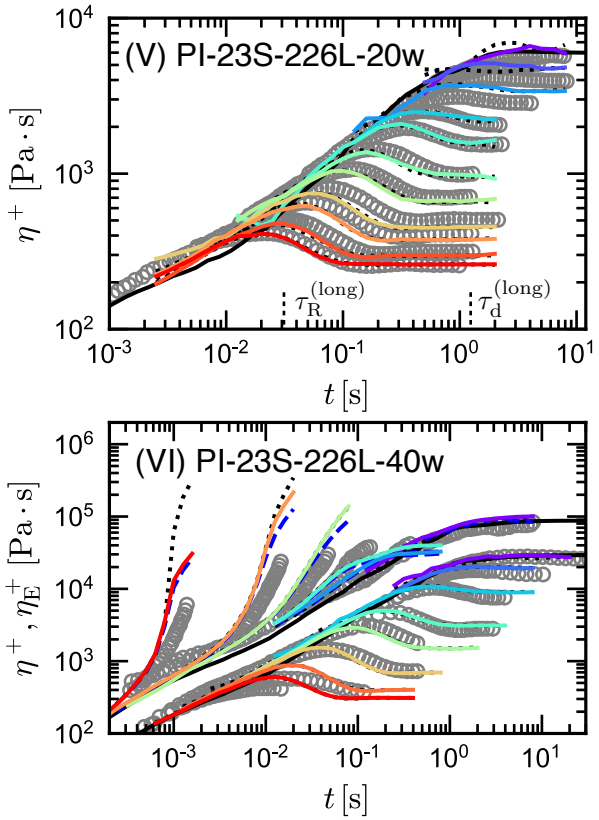

Fig. 5.8 The transient viscosities of (V) PI-_23S-226L-20w under shear (VI) PI-_23S-226L-40w under shear or uniaxial elongation were reported by [147]. Colored solid lines and black dotted lines are the results of the extended DT model with or without the SORF, respectively. Blue dashed lines are the results under uniaxial elongations with the tuned parameter $F'^{*}_{s/o} = 0.007$ by [85]. The black solid line is the LVE result. Symbols show the experimental results.

5.3.4 Application to Polyisoprene Melts

Figure 5.8 shows the transient viscosities (η^+ for shear and η_E^+ for elongation) of (V) PI-_23S-226L-20w under steady shears and (VI) PI-_23S-226L-40w under steady shears and uniaxial elongations. The values of the two units, τ_e and σ_e, are already written in the second paragraph of Section 5.3. The characteristic times of the long chain have the values $\tau_R^{(long)} = 3.1 \times 10^{-2}$ s and $\tau_d^{(long)} = 1.3$ s for PI226k. Those of the short chain have the values $\tau_R^{(twoshort)} = 3.1 \times 10^{-4}$ s and $\tau_d^{(twoshort)} = 4.6 \times 10^{-4}$ s for PI23k.

In Figure 5.8, the transient viscosities under small elongational strain rate flows are in agreement with the LVE result for a long time. On the other hand, under sufficiently high elongational strain rate flows, the responses show nonlinearity, i.e., strain hardening within short times. For both samples under shear flows, the viscosities under higher shear rate flows display stress overshoots and a decrease in the steady values with the shear rate. Regarding the transient shear viscosities, simulations both with and without SORF reasonably reproduce the data of (V) PI-_23S-226L-20w and (VI) PI-_23S-226L-40w, even if the shear rates are larger than the inverse of the Rouse relaxation time of the long chains ($\dot{\gamma}\tau_R^{(long)} \sim 20$),

which is the same tendency observed in the Rolie-double-Poly model [142].

In the upper part in the graph for VI, the elongational viscosity growth functions are also displayed. The elongational viscosities in the DT model, even with the SORF mechanism, are overestimated compared with the experimental viscosities. Here, remembering that the parameters in Eq. (5.11) are for polystyrene, [85] proposed a different value of the parameter $F'^{*}_{\mathrm{s/o}} = 0.007$ for polyisoprene. With $F'^{*}_{\mathrm{s/o}} = 0.007$, they have shown that the predictions of the steady viscosities approach the experimental results in the monodispersed polyisoprene. Thus, we test the proposed parameter for the bidispersed polyisoprene melts, expecting the overestimations to be suppressed. The lower graph for (VI) `PI-_23S-226L-40w` shows the elongational viscosities with $F'^{*}_{\mathrm{s/o}} = 0.14$ (black solid lines) and $F'^{*}_{\mathrm{s/o}} = 0.007$ (blue dashed lines). The results with the smaller $F'^{*}_{\mathrm{s/o}} = 0.007$ approach the experimental results under flows with high elongational strain rates, but still, the $F'^{*}_{\mathrm{s/o}} = 0.007$ does not bring sufficiently good agreement to the data of the nonlinear behavior between the simulations and the experiments. Judging from these deviations, the chemical dependence of the friction reduction mechanism and the appropriate functional form and parameters are not resolved in this study and should be sought in a future study.

In this section, we have confirmed the three following findings: (i) The states of the long chain and the short chain clearly differ from each other under steady elongations; (ii) the DT model with SORF using the component average (`C_S_S`) brings the improvement in the prediction not only for the transient viscosities but also for the steady state elongational viscosities, and (iii) for shear flows, the results with and without SORF predictions are not important for shear flows even with a high shear rate ($\dot{\gamma}\tau_{\mathrm{R}}^{(\mathrm{long})} \sim 20$).

5.4 Conclusions

We studied the rheological predictions by dual sliplink model (extended version of the Doi-Takimoto model) for six samples of the bidisperse entangled polymer melts that have already been measured experimentally. In the extended model, the improvement of stretch- and orientation-induced friction reduction effect is addressed. The rheological predictions basically support the applicability of the SORF expression even for the bidisperse melts under shear and uniaxial elongational flows. The results satisfy the aim of this study: additional confirmation of the SORF mechanism for bidisperse entangled polymer melts.

Through this study, there are three findings. First, the SORF expression proposed by [132] improves the rheological prediction for bidisperse entangled polymer melts under the uniaxial elongational flows with strain rates comparable to or larger than the inverse of the Rouse relaxation time of the longer chain. Second, the predictions with the SORF using the component average for the stretches quantitatively reproduce the steady viscosities because the states of the components with different molecular weights differ from each other under elongational flows. Third, the SORF effect does not affect the prediction of the nonlinear rheology of the bidisperse system under shear even for a high deformation rate for the specific polyisoprene systems. In particular, the second point means that in the frictional dynamics of an entangled polymer chain in a polydisperse system, the state of the considered chain is also important as well as the state of the environment. We show guidelines for the extension of the reduction friction effect obtained from monodisperse melts.

Further studies are clearly required for a deeper understanding of the friction reduction in bidisperse systems. While this study considers two averages (i.e., component and system averages) to reproduce the

experimental rheological data, this treatment has not been fully validated. For such a purpose, Molecular dynamics simulations are highly desirable.

This study is intended to guide the future application of the SORF expression for the prediction of entangled polymer melts under flows not only with a bidisperse distribution, but also with an arbitrary molecular weight distribution for the analysis of polymer processing. Recently, some multiscale simulation (MSS) studies have focused on this model [35–37, 139] due to the computational convenience. The confirmation of the applicability of the DT model into which the SORF mechanism is incorporated is essential for future analysis by using MSS for polymer processing consisting of polydisperse entangled polymer melts. Our research helps us understand effective polymer processing by controlling the molecular weight.

Chapter 6

Concluding Remarks

6.1 Summary

In this thesis, we developed a scheme of MLMSS efficiently simulating the polymer melt flows. We have proposed a protocol for MLMSS, and the studies in the previous chapters have improved the technical elements. The results and discussions are summarized as follows.

In Chapter 2, we established an MLMSS protocol by researching flow analysis to predict flows of polymer melts for simple problems. The time derivative of stress is assumed as a function of stress and velocity gradient. We employ the sliplink model to express the dynamics of well-entangled polymers as a fluid exhibiting a nonlinear stress response. Using microscopic simulators, we successfully predicted flows between two parallel plates with only shear deformations under typical elastic conditions specified by the elastic number, the rate of Weissenberg number to the Reynolds number. Overall, our machine-learning method demonstrates good predictive capabilities for both transient responses and the nonlinear behavior at steady-state, i.e., shear-thinning. We accurately track the evolution of stress for both weak and strong elastic cases, although velocity predictions for the latter show decreased accuracy in the transient regime. Furthermore, our simulation scheme is more computationally efficient than conventional MSS, which uses microscopic simulators containing a system of coarse-grained polymers to evaluate macroscopic stress.

In Chapter 3, following the research in Chapter 2, we extended the MLMSS method to two-dimensional systems with time-dependent deformation mode flows. We summarize the research considering rotational symmetry for stress rate in the constitutive relation of machine learning models, as required by the objectivity principle. The applications have been validated with the analysis of contraction-expansion channel flows driven by pressure gap. We succeeded in learning the constitutive relation using training data generated from shears and planar elongations. The constitutive relation can express stress responses to strain rate histories under a complex geometric system.

In Chapter 4, we assessed another data-driven methodology for the surrogate model of consecutive relations of rheology. We proposed a novel method named Rheo-SINDy, which employs sparse identification of nonlinear dynamics (SINDy) to discover constitutive models from rheological data. This method plays a pivotal role for MLMSS in predicting material behavior by discovering governing equations that relate deformation and stress, namely constitutive equations. Despite the critical importance of constitutive equations in predicting dynamics of complex fluids, a systematic methodology for deriving these equations from available data has remained a significant challenge in the rheology field. Rheo-SINDy was applied to five distinct scenarios, including four cases with well-established constitutive equations and one without predefined equations. Our results demonstrate that Rheo-SINDy successfully identifies accurate constitutive models for the cases with known equations and derives physically plausible

approximate models for the scenario with the unknown one. These findings validate the robustness of Rheo-SINDy in handling MLMSS data complexities and underscore its efficacy as a powerful tool for advancing the development of data-driven approaches.

In Chapter 5, we extended the microscopic entangled polymer model to predict the mechanical response under high strain rate elongations. The SORF mechanism is significant in predicting the viscoelasticity under uniaxial elongational flows, experimentally and theoretically validated for monodispersed polymer systems. To extend the capability of predicting highly nonlinear rheology to a bidisperse molecular weight system, we incorporated an expression of friction reduction into the Doi-Takimoto sliplink model. For six experimental bidisperse systems, i.e., four polystyrene blends and two polyisoprene blends, the extended DT model, where the order parameter is evaluated through component averages, succeeds in reproducing the data under uniaxial elongation and shear. This success is due to the suppression of stretch of longer chains using statistical averages over each component. Through this study, the SORF expression improves rheological predictions for bidisperse entangled polymer melts under uniaxial elongational flows with strain rates comparable to or larger than the inverse of the Rouse relaxation time of the longer chains. This finding indicates that for chain dynamics, the friction coefficient is determined by the state of surrounding polymer chains and the state of the chain. For future use in MLMSS, this accurate rheological prediction ensures the reliability of flow analysis.

6.2 Future Outlooks

Finally, we provide outlooks for extending our proposed MLMSS for potential future developments. When using a machine learning-based model for constitutive relations, we encounter four significant challenges: (i) developing a machine learning-based regression model that fully satisfies the physical requirements of constitutive relations, (ii) designing an effective protocol for creating datasets for the external fields applied to microscopic systems, (iii) introducing an active learning protocol to ensure prediction accuracy when the model encounters inexperienced data regions during simulations.

Possible solutions for these challenges are proposed here: For (i), a regression model must meet two requirements: first, it must adhere to the objectivity principle, demanding rotational symmetry for tensor variables; second, it must demonstrate stability around the equilibrated state of reference systems even under highly deformed states. For (ii), deformation gradient tensors can be algebraically decomposed and classified into key components, possibly reducing the degrees of freedom to smaller dimensions (see [17]). For (iii), the low-fidelity region in predictions of a learned constitutive relation can be detected using Bayesian approaches, utilizing the uncertainty of predicted points. However, this method requires improvement alongside (ii) to generate additional training points by incorporating deformation rate history in inexperienced regions during training processes. Solving these problems is challenging as the three subjects are interrelated, but we should attempt to address them based on the initial steps provided by this thesis.

Improving the description of microscopic polymer models is crucial for fluid flow predictions, not only for the development of the MLMSS protocol itself. The reliability of flow prediction results is evidently limited by the quality of data based on the reference system of a microscopic model when not combined with other data sources. In this thesis, our focus primarily lies on polymer melts of mono-dispersed systems with well-established rheological models, but the methodology of MLMSS can be applied to analyze the flow of other complex fluids. As the first step toward broader application, we have developed an accurate model based on the sliplink model. When aiming to describe more complex

systems comprehensively, such as polydisperse polymer systems, we should consider adding additional descriptors to the regression model to represent almost all aspects of the reference system's state under deformations. Polymer systems with polydisperse molecular weight distributions exhibit multi-mode relaxations of stress corresponding to the length distributions of polymer chains.

Once we verify the accuracy and efficiency of the MLMSS method, we can begin investigating complex and heterogeneous fluids used in industrial processes. Conventional methods typically analyze simple and homogeneous systems, which are far removed from natural materials. Colloidal dispersions in polymeric fluids serve as a prime example of such problematic systems. Despite their functional properties in chemical engineering, understanding their behavior remains significantly challenging. We hope that extending MLMSS from this study will shed light on the origins of rheology observed in industrial processes and soft substances encountered in daily life.

Bibliography

[1] P. G. de Gennes, "Soft matter", Science **256**, 495 (1992).

[2] M. Doi, *Soft matter physics* (Oxford University Press, USA, 2013).

[3] R. G. Larson, *The structure and rheology of complex fluids* (Oxford university press New York, 1999).

[4] R. Bird, W. Stewart, and E. Lightfoot, *Transport phenomena*, revised 2, Transport Phenomena (Wiley, 2006).

[5] M. Rubinsten and C. H. Ralph, *Polymer physics* (Oxford University Press, 2003).

[6] M. Doi and S. F. Edwards, *The theory of polymer dynamics* (Oxford University Press, 1986).

[7] P.-G. De Gennes, *Scaling concepts in polymer physics* (Cornell university press, 1979).

[8] T. Sato, "A review on transport phenomena of entangled polymeric liquids", Nihon Reoroji Gakkaishi (Journal of the Society of Rheology, Japan) **48**, 1 (2020).

[9] S. L. Brunton and J. N. Kutz, *Data-driven science and engineering: machine learning, dynamical systems, and control*, 2nd ed. (Cambridge University Press, 2022).

[10] S. Jamali, "Data-driven rheology: could be a new paradigm?", Rheology Bulletin **92**, 20 (2023).

[11] K. H. Ahn and S. Jamali, "Data-driven methods in rheology", Rheoligica Acta **62**, 473 (2023).

[12] S. Miyamoto, "Short review on machine learning-based multi-scale simulation in rheology", Nihon Reoroji Gakkaishi (Journal of the Society of Rheology, Japan) **52**, 1 (2024).

[13] K. Kremer and G. S. Grest, "Dynamics of entangled linear polymer melts: A molecular-dynamics simulation", Journal of Chemical Physics **92**, 5057 (1990).

[14] P. E. Rouse, "A Theory of the Linear Viscoelastic Properties of Dilute Solutions of Coiling Polymers", Journal of Chemical Physics **21**, 1272 (1953).

[15] A. W. Lees and S. F. Edwards, "The computer study of transport processes under extreme conditions", Journal of Physics C: Solid State Physics **5**, 1921 (1972).

[16] T. A. Hunt, S. Bernardi, and B. D. Todd, "A new algorithm for extended nonequilibrium molecular dynamics simulations of mixed flow", Journal of Chemical Physics **133**, 154116 (2010).

[17] M. Dobson, "Periodic boundary conditions for long-time nonequilibrium molecular dynamics simulations of incompressible flows", Journal of Chemical Physics **141**, 184103 (2014).

[18] D. A. Nicholson and G. C. Rutledge, "Molecular simulation of flow-enhanced nucleation in n-eicosane melts under steady shear and uniaxial extension", Journal of Chemical Physics **145**, 244903 (2016).

[19] M. Laso and H. Öttinger, "Calculation of viscoelastic flow using molecular models: the connffessit approach", Journal of Non-Newtonian Fluid Mechanics **47**, 1 (1993).

[20] C. C. Hua and J. D. Schieber, "Segment connectivity, chain-length breathing, segmental stretch, and constraint release in reptation models. i. theory and single-step strain predictions", Journal of Chemical Physics **109**, 10018 (1998).

[21] C. C. Hua, J. D. Schieber, and D. C. Venerus, "Segment connectivity, chain-length breathing, segmental stretch, and constraint release in reptation models. II. Double-step strain predictions", Journal of Chemical Physics **109**, 10028 (1998).

[22] Y. Masubuchi, J.-I. Takimoto, K. Koyama, G. Ianniruberto, G. Marrucci, and F. Greco, "Brownian simulations of a network of reptating primitive chains", Journal of Chemical Physics **115**, 4387 (2001).

[23] M. Doi and J. Takimoto, "Molecular modelling of entanglement", Philosophical Transactions of the Royal Society A **361**, 641 (2003).

[24] J. D. Schieber, J. Neergaard, and S. Gupta, "A full-chain, temporary network model with sliplinks, chain-length fluctuations, chain connectivity and chain stretching", Journal of Rheology **47**, 213 (2003).

[25] J. D. Schieber, "Fluctuations in entanglements of polymer liquids", Journal of Chemical Physics **118**, 5162 (2003).

[26] J. D. Schieber, "Generic compliance of a temporary network model with sliplinks, chain-length fluctuations, segment-connectivity and constraint release", Journal of Non-Equilibrium Thermodynamics **28**, 179 (2003).

[27] J. G. Oldroyd, "On the formulation of rheological equations of state", Proceedings of the Royal Society of London. Series A. **200**, 523 (1950).

[28] J. L. White and A. B. Metzner, "Development of constitutive equations for polymeric melts and solutions", Journal of Applied Polymer Science **7**, 1867 (1963).

[29] H. Giesekus, "A simple constitutive equation for polymer fluids based on the concept of deformation-dependent tensorial mobility", Journal of Non-Newtonian Fluid Mechanics **11**, 69 (1982).

[30] N. P. Thien and R. I. Tanner, "A new constitutive equation derived from network theory", Journal of Non-Newtonian Fluid Mechanics **2**, 353 (1977).

[31] J. J. Monaghan, "Smoothed particle hydrodynamics", Annual Review of Astronomy and Astrophysics **30**, 543 (1992).

[32] M. Ellero, P. Español, and E. G. Flekkøy, "Thermodynamically consistent fluid particle model for viscoelastic flows", Physical Review E **68**, 041504 (2003).

[33] T. Murashima and T. Taniguchi, "Multiscale lagrangian fluid dynamics simulation for polymeric fluid", Journal of Polymer Science Part B: Polymer Physics **48**, 886 (2010).

[34] H. Feng, M. Andreev, E. Pilyugina, and J. D. Schieber, "Smoothed particle hydrodynamics simulation of viscoelastic flows with the slip-link model", Molecular Systems Design & Engineering **1**, 99 (2016).

[35] T. Sato and T. Taniguchi, "Multiscale simulations for entangled polymer melt spinning process", Journal of Non-Newtonian Fluid Mechanics **241**, 34 (2017).

[36] T. Sato, K. Harada, and T. Taniguchi, "Multiscale simulations of flows of a well-entangled polymer melt in a contraction-expansion channel", Macromolecules **52**, 547 (2019).

[37] Y. Hamada, T. Sato, and T. Taniguchi, "Multiscale simulation of a polymer melt flow between two coaxial cylinders under nonisothermal conditions", Mathematics in Engineering **3**, 1 (2021).

[38] Y. Morii and T. Kawakatsu, "Lagrangian multiscale simulation of complex flows", Physics of Fluids **33**, 093106 (2021).

[39] N. Moreno and M. Ellero, "Generalized lagrangian heterogeneous multiscale modelling of complex fluids", Journal of Fluid Mechanics **969**, A2 (2023).

[40] S. Yasuda and R. Yamamoto, "A model for hybrid simulations of molecular dynamics and computational fluid dynamics", Physics of Fluids **20**, 113101 (2008).

[41] T. Sato, K. Takase, and T. Taniguchi, "Multiscale simulation of polymer melt spinning by using the dumbbell model", Nihon Reoroji Gakkaishi (Journal of the Society of Rheology, Japan) **44**, 265 (2017).

[42] Y. Xu, Y. Hamada, and T. Taniguchi, "Multiscale simulations for polymer melt spinning process using kremer–grest cg model and continuous fluid mechanics model", Journal of Non-Newtonian Fluid Mechanics **325**, 105195 (2024).

[43] S. L. Brunton, J. L. Proctor, and J. N. Kutz, "Discovering governing equations from data by sparse identification of nonlinear dynamical systems", Proceedings of the National Academy of Sciences of the United States of America **113**, 3932 (2016).

[44] M. Raissi, P. Perdikaris, and G. Karniadakis, "Physics-informed neural networks: a deep learning framework for solving forward and inverse problems involving nonlinear partial differential equations", Journal of Computational Physics **378**, 686 (2019).

[45] A. Ghadami and B. I. Epureanu, "Data-driven prediction in dynamical systems: recent developments", Philosophical Transactions of the Royal Society A **380**, 20210213 (2022).

[46] W. Li, C. Burkhart, P. Polińska, V. Harmandaris, and M. Doxastakis, "Backmapping coarse-grained macromolecules: An efficient and versatile machine learning approach", Journal of Chemical Physics **153**, 041101 (2020).

[47] S. Dhamankar and M. A. Webb, "Chemically specific coarse-graining of polymers: methods and prospects", Journal of Polymer Science **59**, 2613 (2021).

[48] B. Ravikumar, I. K. Karathanassis, T. Smith, and M. Gavaises, "Multi-scale modelling of dilute viscoelastic liquids: atomistic to mesoscale mapping of polymer solutions", Polymer **285**, 126360 (2023).

[49] R. S. Mukkamala and M. J. A. Hore, "Simulation and analysis of molecular bottlebrush dynamics in dilute solutions", Macromolecules **57**, 445 (2024).

[50] Z. Shireen, H. Weeratunge, A. Menzel, A. W. Phillips, R. G. Larson, K. Smith-Miles, and E. Hajizadeh, "A machine learning enabled hybrid optimization framework for efficient coarse-graining of a model polymer", npj Computational Materials **8**, 224 (2022).

[51] K. Endo, K. Tomobe, and K. Yasuoka, "Multi-step time series generator for molecular dynamics", Proceedings of the International AAAI Conference on Web and Social Media **32** (2018).

[52] R. Kawada, K. Endo, D. Yuhara, and K. Yasuoka, "Md-gan with multi-particle input: the machine learning of long-time molecular behavior from short-time md data", Soft Matter **18**, 8446 (2022).

[53] J. L. Proctor, S. L. Brunton, and J. N. Kutz, "Dynamic mode decomposition with control", SIAM Journal on Applied Dynamical Systems **15**, 142 (2016).

[54] L. Zhao, Z. Li, B. Caswell, J. Ouyang, and G. E. Karniadakis, "Active learning of constitutive relation from mesoscopic dynamics for macroscopic modeling of non-newtonian flows", Journal of Computational Physics **363**, 116 (2018).

[55] N. Seryo, T. Sato, J. J. Molina, and T. Taniguchi, "Learning the constitutive relation of polymeric flows with memory", Physical Review Research **2**, 033107 (2020).

[56] L. Zhao, Z. Li, Z. Wang, B. Caswell, J. Ouyang, and G. E. Karniadakis, "Active- and transfer-learning applied to microscale-macroscale coupling to simulate viscoelastic flows", Journal of Computational Physics **427**, 110069 (2021).

[57] M. Mahmoudabadbozchelou and S. Jamali, "Rheology-informed neural networks (rhinns) for forward and inverse metamodelling of complex fluids", Scientific Reports **11**, 12015 (2021).

[58] K. R. Lennon, G. H. McKinley, and J. W. Swan, "Scientific machine learning for modeling and simulating complex fluids", Proceedings of the National Academy of Sciences of the United States of America **120**, e2304669120 (2023).

[59] H. Jin, S. Yoon, F. C. Park, and K. H. Ahn, "Data-driven constitutive model of complex fluids using recurrent neural networks", Rheoligica Acta **62**, 569 (2023).

[60] L. Fang, P. Ge, L. Zhang, W. E, and H. Lei, "DeePN^2: a deep learning-based non-newtonian hydrodynamic model", Journal of Machine Learning **1**, 114 (2022).

[61] S. Miyamoto, J. J. Molina, and T. Taniguchi, "Machine-learned constitutive relations for multi-scale simulations of well-entangled polymer melts", Physics of Fluids **35**, 063113 (2023).

[62] Y.-J. Chang, H.-Y. Huang, R.-L. Chern, and Y.-J. Chou, "A multiscale computational framework using active learning to model complex suspension flows", Journal of Computational Physics **493**, 112481 (2023).

[63] Y. Xu, S. Miyamoto, and T. Taniguchi, "Machine-learning based multi-scale simulation for polymer melt spinning process", Nihon Reoroji Gakkaishi (Journal of the Society of Rheology, Japan) **51**, 51 (2023).

[64] Z. Zhang, Y. Shin, and G. Em Karniadakis, "Gfinns: generic formalism informed neural networks for deterministic and stochastic dynamical systems", Philosophical Transactions of the Royal Society A **380**, 20210207 (2022).

[65] S. Greydanus, M. Dzamba, and J. Yosinski, "Hamiltonian neural networks", Advances in neural information processing systems **32** (2019).

[66] M. Cranmer, S. Greydanus, S. Hoyer, P. Battaglia, D. Spergel, and S. Ho, "Lagrangian neural networks", arXiv preprint arXiv:2003.04630 (2020).

[67] M. Mahmoudabadbozchelou, G. E. Karniadakis, and S. Jamali, "nn-PINNs: non-newtonian physics-informed neural networks for complex fluid modeling", Soft Matter **18**, 172 (2022).

[68] N. Seryo, J. J. Molina, and T. Taniguchi, "Select applications of bayesian data analysis and machine learning to flow problems", Nihon Reoroji Gakkaishi (Journal of the Society of Rheology, Japan) **49**, 97 (2021).

[69] J. J. Molina, K. Ogawa, and T. Taniguchi, "Stokesian processes : inferring stokes flows using physics-informed gaussian processes", Machine Learning: Science and Technology **4**, 045013 (2023).

[70] M. Saadat, D. Mangal, and S. Jamali, "A rheologist's guideline to data-driven recovery of complex fluids' parameters from constitutive models", Digital Discovery **2**, 915 (2023).

[71] S. Farrington, S. Jariwala, M. Armstrong, E. Nigro, N. J. Wagner, and A. N. Beris, "Physiology-based parameterization of human blood steady shear rheology via machine learning: a hemostatistics contribution", Rheoligica Acta **62**, 491 (2023).

[72] Y. Hayashi, J. Shiomi, J. Morikawa, and R. Yoshida, "Radonpy: automated physical property calculation using all-atom classical molecular dynamics simulations for polymer informatics", npj Computational Materials **8**, 222 (2022).

[73] Y. Wang, J. Ouyang, and X. Wang, "Machine learning of lubrication correction based on gpr for the coupled dpd–dem simulation of colloidal suspensions", Soft Matter **17**, 5682 (2021).

[74] R. B. Bird, R. C. Armstrong, and O. Hassager, *Dynamics of polymeric liquids*, 2nd ed., Vol. 2 (Oxford University Press, 1987).

[75] C. Saengow, A. J. Giacomin, N. Grizzuti, and R. Pasquino, "Startup steady shear flow from the oldroyd 8-constant framework", Physics of Fluids **31**, 063101 (2019).

[76] M. Pavelka, V. Klika, and M. Grmela, *Multiscale thermo-dynamics: introduction to generic* (Walter de Gruyter GmbH & Co KG, 2018).

[77] T. Watanabe and T. Gotoh, "Hybrid eulerian–lagrangian simulations for polymer–turbulence interactions", Journal of Fluid Mechanics **717**, 535 (2013).

[78] H.-J. Yan, Z.-H. Wan, F.-H. Qin, and D.-J. Sun, "Multiscale Simulations of Polymer Flow Between Two Parallel Plates", Journal of Fluids Engineering **143**, 041208 (2021).

[79] T. Murashima and T. Taniguchi, "Multiscale simulation of history-dependent flow in entangled polymer melts", Europhysics Letters **96**, 18002 (2011).

[80] T. Murashima and T. Taniguchi, "Flow-history-dependent behavior of entangled polymer melt flow analyzed by multiscale simulation", Journal of the Physical Society of Japan **81**, SA013 (2012).

[81] T. Murashima, S. Yasuda, T. Taniguchi, and R. Yamamoto, "Multiscale modeling for polymeric flow: particle-fluid bridging scale methods", Journal of the Physical Society of Japan **82**, 012001 (2013).

[82] T. Sato and T. Taniguchi, "Multiscale simulation of the flows of a bidisperse entangled polymer melt", Nihon Reoroji Gakkaishi (Journal of the Society of Rheology, Japan) **49**, 87 (2021).

[83] M. Mahmoudabadbozchelou and S. Jamali, "Rheology-informed neural networks (RhINNs) for forward and inverse metamodelling of complex fluids", Scientific Reports **11**, 12015 (2021).

[84] M. Saadat, M. Mahmoudabadbozchelou, and S. Jamali, "Data-driven selection of constitutive models via rheology-informed neural networks (RhINNs)", Rheoligica Acta **61**, 721 (2022).

[85] T. Sato and T. Taniguchi, "Rheology and entanglement structure of well-entangled polymer melts: a slip-link simulation study", Macromolecules **52**, 3951 (2019).

[86] S. Miyamoto, T. Sato, and T. Taniguchi, "Stretch-orientation-induced reduction of friction in well-entangled bidisperse blends: a dual slip-link simulation study", Rheoligica Acta **62**, 57 (2023).

[87] T. Sato, Y. Kwon, Y. Matsumiya, and H. Watanabe, "A constitutive equation for Rouse model modified for variations of spring stiffness, bead friction, and Brownian force intensity under flow", Physics of Fluids **33**, 063106 (2021).

[88] C. E. Rasmussen, C. K. Williams, et al., *Gaussian processes for machine learning*, Vol. 1 (Springer, 2006).

[89] J. R. Gardner, G. Pleiss, D. Bindel, K. Q. Weinberger, and A. G. Wilson, "Gpytorch: blackbox matrix-matrix gaussian process inference with gpu acceleration", in Advances in neural information processing systems (2018).

[90] A. Paszke, S. Gross, F. Massa, A. Lerer, J. Bradbury, G. Chanan, T. Killeen, Z. Lin, N. Gimelshein, L. Antiga, A. Desmaison, A. Kopf, E. Yang, Z. DeVito, M. Raison, A. Tejani, S. Chilamkurthy, B. Steiner, L. Fang, J. Bai, and S. Chintala, in *Advances in neural information processing systems* (Curran Associates, Inc., 2019), pp. 8024–8035.

[91] M. Iwasawa, A. Tanikawa, N. Hosono, K. Nitadori, T. Muranushi, and J. Makino, Publications of the Astronomical Society of Japan **68**, 54 (2016).

[92] T. Murashima, "Inter node parallelization of multiscale fluid particle simulation towards large-scale polymeric fluid simulation", Microsystem Technologies **24**, 765 (2018).

[93] J. P. Morris, P. J. Fox, and Y. Zhu, "Modeling low reynolds number incompressible flows using sph", Journal of Computational Physics **136**, 214 (1997).

[94] T. Murashima, "Multiscale simulation performed on issp super computer: analysis of entangled polymer melt flow, activity report 2015", Activity Report 2015/Supercomputer Center, Institute for Solid State Physics, The University of Tokyo, 35 (2016).

[95] G. M. Zhang and R. C. Batra, "Symmetric smoothed particle hydrodynamics (ssph) method and its application to elastic problems", Computational Mechanics **43**, 321 (2009).

[96] C. Huang, J. M. Lei, M. B. Liu, and X. Y. Peng, "A kernel gradient free (kgf) sph method", International Journal for Numerical Methods in Fluids **78**, 691 (2015).

[97] B. M. de Silva, D. M. Higdon, S. L. Brunton, and J. N. Kutz, "Discovery of physics from data: universal laws and discrepancies", Frontiers in artificial intelligence **3**, 25 (2020).

[98] K. Kaheman, S. L. Brunton, and J. Nathan Kutz, "Automatic differentiation to simultaneously identify nonlinear dynamics and extract noise probability distributions from data", Machine Learning: Science and Technology **3**, 015031 (2022).

[99] U. Fasel, J. N. Kutz, B. W. Brunton, and S. L. Brunton, "Ensemble-SINDy: robust sparse model discovery in the low-data, high-noise limit, with active learning and control", Proceedings: Mathematical, Physical and Engineering Sciences **478**, 20210904 (2022).

[100] M. Schmidt and H. Lipson, "Distilling Free-Form natural laws from experimental data", Science **324**, 81 (2009).

[101] J. Bongard and H. Lipson, "Automated reverse engineering of nonlinear dynamical systems", Proceedings of the National Academy of Sciences of the United States of America **104**, 9943 (2007).

[102] P. A. K. Reinbold, L. M. Kageorge, M. F. Schatz, and R. O. Grigoriev, "Robust learning from noisy, incomplete, high-dimensional experimental data via physically constrained symbolic regression", Nature communications **12**, 3219 (2021).

[103] S.-M. Udrescu and M. Tegmark, "AI feynman: a physics-inspired method for symbolic regression", Science Advances **6**, eaay2631 (2020).

[104] G. E. Karniadakis, I. G. Kevrekidis, L. Lu, P. Perdikaris, S. Wang, and L. Yang, "Physics-informed machine learning", Nature Reviews Physics **3**, 422 (2021).

[105] X. Jia, J. Willard, A. Karpatne, J. S. Read, J. A. Zwart, M. Steinbach, and V. Kumar, "Physics-Guided machine learning for scientific discovery: an application in simulating lake temperature profiles", ACM IMS Transactions on Data Science **2**, 1 (2021).

[106] S. G. Rosofsky, H. Al Majed, and E. A. Huerta, "Applications of physics informed neural operators", Machine Learning: Science and Technology **4**, 025022 (2023).

[107] A. E. Likhtman, "Single-chain slip-link model of entangled polymers: simultaneous description of neutron spin-echo, rheology, and diffusion", Macromolecules **38**, 6128 (2005).

[108] M. Mahmoudabadbozchelou, K. M. Kamani, S. A. Rogers, and S. Jamali, "Digital rheometer twins: learning the hidden rheology of complex fluids through rheology-informed graph neural networks", Proceedings of the National Academy of Sciences of the United States of America **119**, e2202234119 (2022).

[109] M. Mahmoudabadbozchelou, M. Caggioni, S. Shahsavari, W. H. Hartt, G. Em Karniadakis, and S. Jamali, "Data-driven physics-informed constitutive metamodeling of complex fluids: A multifidelity neural network (MFNN) framework", Journal of Rheology **65**, 179 (2021).

[110] K. Fukami, T. Murata, K. Zhang, and K. Fukagata, "Sparse identification of nonlinear dynamics with low-dimensionalized flow representations", Journal of Fluid Mechanics **926**, A10 (2021).

[111] M. Mahmoudabadbozchelou, K. M. Kamani, S. A. Rogers, and S. Jamali, "Unbiased construction of constitutive relations for soft materials from experiments via rheology-informed neural networks", Proceedings of the National Academy of Sciences of the United States of America **121**, e2313658121 (2024).

[112] R. . Larson, *Constitutive equations for polymer melts and solutions* (Butterworths Series in Chemical Engineering, 1988).

[113] M. D. Graham, "Drag reduction and the dynamics of turbulence in simple and complex fluids", Physics of Fluids **26**, 101301 (2014).

[114] Y. Mochimaru, "Unsteady-state development of plane couette flow for viscoelastic fluids", Journal of Non-Newtonian Fluid Mechanics **12**, 135 (1983).

[115] T. Sato, S. Moghadam, G. Tan, and R. G. Larson, "A slip-spring simulation model for predicting linear and nonlinear rheology of entangled wormlike micellar solutions", Journal of Rheology **64**, 1045 (2020).

[116] T. Sato and R. G. Larson, "Nonlinear rheology of entangled wormlike micellar solutions predicted by a micelle-slip-spring model", Journal of Rheology **66**, 639 (2022).

[117] K. Hyun, M. Wilhelm, C. O. Klein, K. S. Cho, J. G. Nam, K. H. Ahn, S. J. Lee, R. H. Ewoldt, and G. H. McKinley, "A review of nonlinear oscillatory shear tests: analysis and application of large amplitude oscillatory shear (LAOS)", Progress in Polymer Science **36**, 1697 (2011).

[118] S. H. Rudy, S. L. Brunton, J. L. Proctor, and J. N. Kutz, "Data-driven discovery of partial differential equations", Science Advances **3**, e1602614 (2017).

[119] F. Pedregosa, G. Varoquaux, A. Gramfort, V. Michel, B. Thirion, O. Grisel, M. Blondel, P. Prettenhofer, R. Weiss, V. Dubourg, J. Vanderplas, A. Passos, D. Cournapeau, M. Brucher, M. Perrot, and E. Duchesnay, "Scikit-learn: machine learning in Python", Journal of Machine Learning Research **12**, 2825 (2011).

[120] H. Zou, "The adaptive lasso and its oracle properties", Journal of American Statistical Association **101**, 1418 (2006).

[121] J. D. Ferry, *Viscoelastic properties of polymers* (John Wiley & Sons, 1980).

[122] F. P. L. Mantia, A. Valenza, and D. Acierno, "Influence of the structure of linear density polyethylene on the rheological and mechanical properties of blends with low density polyethylene", European Polymer Journal **22**, 647 (1986).

[123] A. Minegishi, A. Nishioka, T. Takahashi, Y. Masubuchi, J.-i. Takimoto, and K. Koyama, "Uniaxial elongational viscosity of ps/a small amount of uhmw-ps blends", Rheologica Acta **40**, 329 (2001).

[124] J. K. Nielsen, H. K. Rasmussen, O. Hassager, and G. H. McKinley, "Elongational viscosity of monodisperse and bidisperse polystyrene melts", Journal of Rheology **50**, 453 (2006).

[125] E. van Ruymbeke, J. Nielsen, and O. Hassager, "Linear and nonlinear viscoelastic properties of bidisperse linear polymers: mixing law and tube pressure effect", Journal of Rheology **54**, 1155 (2010).

[126] L. Hengeller, Q. Huang, A. Dorokhin, N. J. Alvarez, K. Almdal, and O. Hassager, "Stress relaxation of bi-disperse polystyrene melts: exploring the interactions between long and short chains in non-linear rheology", Rheologica Acta **55**, 303 (2016).

[127] J. L. Viovy, M. Rubinstein, and R. H. Colby, "Constraint release in polymer melts: tube reorganization versus tube dilation", Macromolecules **24**, 3587 (1991).

[128] Y. Masubuchi, "Simulating the flow of entangled polymers", Annual Review of Chemical and Biomolecular Engineering **5**, 11 (2014).

[129] G. Ianniruberto, A. Brasiello, and G. Marrucci, "Simulations of fast shear flows of ps oligomers confirm monomeric friction reduction in fast elongational flows of monodisperse ps melts as indicated by rheooptical data", Macromolecules **45**, 8058 (2012).

[130] G. Ianniruberto, G. Marrucci, and Y. Masubuchi, "Melts of linear polymers in fast flows", Macromolecules **53** (2020).

[131] Y. Matsumiya and H. Watanabe, *Non-universal features in uniaxially extensional rheology of linear polymer melts and concentrated solutions: a review*, 2021.

[132] T. Yaoita, T. Isaki, Y. Masubuchi, H. Watanabe, G. Ianniruberto, and G. Marrucci, "Primitive chain network simulation of elongational flows of entangled linear chains: stretch/orientation-induced reduction of monomeric friction", Macromolecules **45**, 2773 (2012).

[133] Y. Masubuchi, Y. Matsumiya, and H. Watanabe, "Test of orientation/stretch-induced reduction of friction via primitive chain network simulations for polystyrene, polyisoprene, and poly(n-butyl acrylate)", Macromolecules **47**, 6768 (2014).

[134] K. Takeda, Y. Masubuchi, S. S. Kumar, M. Sugimoto, K. Koyama, and Y. Masubuchi, "Re-examination of the effect of the stretch/orientation-induced reduction of friction under equi-biaxial elongational flow via primitive chain network simulation using two definitions of orientation anisotropy", Nihon Reoroji Gakkaishi (Journal of the Society of Rheology, Japan) **46**, 145 (2018).

[135] K. Takeda, Y. Masubuchi, M. Sugimoto, K. Koyama, and S. K. Sukumaran, "Simulations of startup planar elongation of an entangled polymer melt", Nihon Reoroji Gakkaishi (Journal of the Society of Rheology, Japan) **48**, 43 (2020).

[136] Y. Masubuchi, Y. Matsumiya, H. Watanabe, G. Marrucci, and G. Ianniruberto, "Primitive chain network simulations for pom-pom polymers in uniaxial elongational flows", Macromolecules **47**, 3511 (2014).

[137] Y. Masubuchi, G. Ianniruberto, and G. Marrucci, "Primitive chain network simulations of entangled melts of symmetric and asymmetric star polymers in uniaxial elongational flows", Nihon Reoroji Gakkaishi (Journal of the Society of Rheology, Japan) **49**, 171 (2021).

[138] H. Watanabe, Y. Matsumiya, and T. Sato, "Nonlinear rheology of fene dumbbell with friction-reduction: analysis of brownian force intensity through comparison of extensional and shear viscosities", Nihon Reoroji Gakkaishi (Journal of the Society of Rheology, Japan) **48**, 259 (2020).

[139] T. Sato, Y. Kwon, Y. Matsumiya, and H. Watanabe, "A constitutive equation for rouse model modified for variations of spring stiffness, bead friction, and brownian force intensity under flow", Physics of Fluids **33** (2021).

[140] K. Takeda, S. K. Sukumaran, M. Sugimoto, K. Koyama, and Y. Masubuchi, "Primitive chain network simulations for elongational viscosity of bidisperse polystyrene melts", Advanced Modeling and Simulation in Engineering Sciences **2** (2015).

[141] D. J. Read, M. E. Shivokhin, and A. E. Likhtman, "Contour length fluctuations and constraint release in entangled polymers: slip-spring simulations and their implications for binary blend rheology", Journal of Rheology **62**, 1017 (2018).

[142] V. A. H. Boudara, J. D. Peterson, L. G. Leal, and D. J. Read, "Nonlinear rheology of polydisperse blends of entangled linear polymers: rolie-double-poly models", Journal of Rheology **63**, 71 (2019).

[143] T. Uneyama and Y. Masubuchi, "Plateau moduli of several single-chain slip-link and slip-spring models", Macromolecules **54**, 1338 (2021).

[144] S. Costanzo, Q. Huang, G. Ianniruberto, G. Marrucci, O. Hassager, and D. Vlassopoulos, "Shear and extensional rheology of polystyrene melts and solutions with the same number of entanglements", Macromolecules **49**, 3925 (2016).

[145] H. Watanabe, Y. Matsumiya, and T. Sato, "Revisiting nonlinear flow behavior of rouse chain: roles of fene, friction-reduction, and brownian force intensity variation", Macromolecules **54**, 3700 (2021).

[146] Y. Masubuchi and Y. Amamoto, "Orientational cross-correlation in entangled binary blends in primitive chain network simulations", Macromolecules **49**, 9258 (2016).

[147] D. J. Read, K. Jagannathan, S. K. Sukumaran, and D. Auhl, "A full-chain constitutive model for bidisperse blends of linear polymers", Journal of Rheology **56**, 823 (2012).

[148] J. Ramírez, S. K. Sukumaran, B. Vorselaars, and A. E. Likhtman, "Efficient on the fly calculation of time correlation functions in computer simulations", Journal of Chemical Physics **133**, 154103 (2010).

[149] A. Bach, K. Almdal, H. K. Rasmussen, and O. Hassager, "Elongational viscosity of narrow molar mass distribution polystyrene", Macromolecules **36**, 5174 (2003).

Acknowledgements

本学位論文は，2019年から2024年にかけて工学研究科化学工学専攻ソフトマター工学研究室（旧称：移動現象論研究室）で行った研究をまとめたものです．はじめに，直接ご指導いただいた主査の谷口貴志准教授に深く感謝申し上げます．主としてマルチスケールシミュレーションの方法についてご教示いただきました．また，機械学習に関してはJohn J. Molina助教にご教導いただきました．さらに，研究室を主催する山本量一教授にも研究方針に関して助言いただきました．長年の研究指導を通して研究内容に対する厳格さは勿論のこと，その活動を楽しむ姿勢をご教示いただきました．先生方のお力添えなくして本論文は完成できませんでした．心より御礼申し上げます．

副査として審査にご協力いただいた浦山健治教授と外輪健一郎教授に感謝申し上げます．論文内容や表現に対してコメントをいただき，改善のきっかけとなりました．

本論文の作成にあたり，主に分子レオロジーに関して佐藤健助教に多大な協力をいただきました．また，加藤祥太助教には，情報学寄りの立場から助言をいただきました．また，Xu Yan博士には本論文に関連する研究プロジェクトを主導いただきました． 3氏には研究だけでなく，各種の雑多な相談もお引き受けいただきました．心より感謝申し上げます．

同研究室研究員のMayank Dixit博士と今村舜博士には研究に関する議論や，アドバイスをいただきました．同課程の小林巧弥君には日頃の雑多な相談に付き合っていただきました．大学院の生活では，3氏から大きな刺激を受けました．ここに深く感謝申し上げます．

勉強会を共にした学生の皆様に御礼申し上げます．機械学習の勉強会を赤木美佳さん，小川健太君，上野由樹君，Gomez Soria Luis Angel君と，分子動力学の勉強会を藤井翔麻君，植田晃亮君，太田志哉君，岩見弦君，山本浩司君と，統計の勉強会を北川佳史君と行いました．また，平松崇文さんにはよく研究に関する議論をしていただきました．

研究活動に関する様々な手続きに関して，秘書の星原花絵様にご協力いただきました．また，経済的な支援を，京都大学科学技術イノベーション創出フェローシップと，日本学術振興会特別研究員制度からいただきました．ご支援無くして研究活動は継続できませんでした，他，研究活動の中で関わっていただいた多くの皆さんと，これまで見守ってくださった私の両親に，あらためて感謝の意を表します．

宮本 奏汰

2024

Publications

Discussed in this thesis

- Souta Miyamoto "Short Review on Machine Learning-based Multi-Scale Simulation in Rheology", *Nihon Reoroji Gakkaishi* (*Journal of the Society of Rheology, Japan*), **52**(1), 15-19 (2024).
  [Parts of **Chapter 1** are reproduced from this paper with permission.]

- Souta Miyamoto, John J Molina and Takashi Taniguchi "Machine-learned constitutive relations for multi-scale simulation of well-entangled polymer melts", *Physics of Fluids*, **35**(6), 063113 (2023).
  [**Chapter 2** is reproduced from this paper with the permission of AIP Publishing.]

- Souta Miyamoto, John J Molina and Takashi Taniguchi "Machine-learned constitutive relations resolving time-dependent deformation modes: a multi-scale simulation study of well-entangled polymer melts", **in preparation**.
  [This paper is based on parts of **Chapter 3**.]

- Takeshi Sato, Souta Miyamoto(co-first) and Shota Kato, "Rheo-SINDy: Finding a Constitutive Model from Rheological Data Using Sparse Identification for Nonlinear Dynamics", **submitted**, arXiv:2403.14980.
  [Parts of **Chapter 4** are reproduced from this paper with the permission of the authors.]

- Souta Miyamoto, Takeshi Sato and Takashi Taniguchi "Stretch-orientation-induced reduction of friction in well-entangled bidisperse blends: a dual slip-link simulation study", *Rheologica Acta*, **62**(1), 57-70 (2023).
  [**Chapter 5** is reproduced from this paper with the permission of Springer Nature.]

Others not discussed in this thesis

- Yan Xu, Souta Miyamoto and Takashi Taniguchi, "Machine-learning based multi-scale simulation for polymer melt spinning process", *Nihon Reoroji Gakkaishi* (*Journal of the Society of Rheology, Japan*), **51**(5), 281-294 (2023).